A DOUBLE STRAND DNA BREAK MODEL OF PHOTON AND ELECTRON RELATIVE BIOLOGICAL EFFECTIVENESS

A Dissertation
Presented to
The Academic Faculty

by

Michael Bruce Bellamy

In Partial Fulfillment
of the Requirements for the Degree
Doctor of Philosophy in the
George W. Woodruff School of Mechanical Engineering

Georgia Institute of Technology
Spring 2013

A DETERMINISTIC MODEL OF THE RELATIVE BIOLOGICAL EFFECTIVENESS OF PHOTONS AND ELECTRONS

Approved by:

Dr. Nolan Hertel, Advisor
School of Mechanical Engineering
Georgia Institute of Technology

Dr. Chris Wang
School of Mechanical Engineering
Georgia Institute of Technology

Dr. Armin Ansari
School of Mechanical Engineering
Georgia Institute of Technology

Dr. Robert Foley
School of Industrial and Systems Engineering
Georgia Institute of Technology

Dr. Keith Eckerman
School of Nuclear Engineering
University of Tennessee

Date Approved:

ACKNOWLEDGEMENTS

It is a pleasure to express my gratitude to the many individuals who have supported, encouraged and advised me throughout this journey. This thesis would not have been possible without those mentioned here.

I owe my deepest gratitude to my distinguished and respected mentor Dr. Keith Eckerman who has taught, encouraged, paid, corrected, guided and tremendously assisted me from the beginning through the end of this project. I am extremely grateful to Dr. Ryan Manger for kindly providing nuggets of wisdom which enrich this work. It is an honor for me to acknowledge, Dr. Nolan Hertel for his steadfast influence, encouragement and mentorship throughout my Ph.D. matriculation. I would like to show my gratitude to Dr. Chris Wang for providing valuable insight into this topic and challenging me to constantly improve. I would like to thank my committee members, Dr. Armin Ansari and Dr. Robert Foley for their experience and support. I would also like to thank Dr. Richard Leggett for his advice and ideas.

I am especially grateful to my wife and daughter, Kristien and Kira Bellamy for their love, support, direction and for purposing my existence. I wish to thank my mother,

Salisha Bellamy for her love, encouragement and all of the sacrifices she made for me. In addition, I want to thank my entire extended family for their guidance and support.

Finally, I would like to acknowledge the esteemed and beloved Dr. James Turner for laying the scientific foundations upon which my approach is built.

TABLE OF CONTENTS

LIST OF FIGURES

SUMMARY

The ICRP recommends a radiation weighting factor of one for all low-LET radiation. However, many experimental studies find inconsistencies between low-LET RBE and the ICRP's current radiation weighting factor. Generally, there is evidence that dependence exists between radiation energy and radiation RBE where lower energy radiations tend to have a greater biological effect than higher energy radiation. Specifically, the radiations of tritium and carbon K-shell x-rays have been studied in numerous experiments and the biological effects of both of these radiations are consistently greater than that of Co-60.

In this work, the relationship between radiation energy and radiation effect has been investigated with the use of a newly developed double strand break (DSB) yield estimation algorithm. This algorithm makes use of a detailed solenoidal 30 nm DNA chromatin model to describe the radiation-sensitive biological target. In addition to the DNA model, NOREC, an event by event Monte Carlo code, was used in this algorithm to characterize the electron track. As an alternative to the conventional approach of computationally simulating DNA damage by spatial overlay of an electron track on DNA, this algorithm instead focuses on quantifying the distance between ionizations in

an electron track and next determining the likelihood that any given ionization pair forms a DSB. The first step of the algorithm involves electron characterization while the second step relies on DNA molecule characterization. By assuming a DSB biological endpoint and determining the DSB yield as a function of electron energy, energy dependent RBE values were estimated for monoenergetic electrons from 10 eV to 1 MeV.

Photon RBE values, x-ray RBE values and radionuclide RBE values were also calculated and reported in this work in addition to electron RBE values. Photon RBE values were estimated based upon the electron RBE calculation. Photon RBE values were reported from 1 eV to 10 MeV. In turn, x-ray RBE values were calculated based upon photon values for several tube voltage and filter combinations. Finally, RBE values for over 1000 radionuclides were estimated and reported.

CHAPTER 1

OBJECTIVE

The objective of this study is to investigate the RBE of low-LET radiation with the goal of predicting the RBE of any arbitrary low-LET source.

CHAPTER 2

BACKGROUND

Absorbed dose, D, is the most fundamental dosimetric quantity. This is the energy absorbed per unit mass and it is expressed in the units of gray. In standard units, the unit of absorbed dose, the gray, is equivalent to 1 joule per kilogram. Although absorbed dose can be defined at a point, it is typically expressed as the average over some volume such as a cell, organ, or organism. Absorbed dose can be used to predict the occurrence of radiation induced biological effects such as cell death, cancer and organism death. In some cases, the radiation induced effect is probabilistic or stochastic, while in other cases the effect is deterministic.

The probability of radiation induced effects depends on several other factors in addition to absorbed dose. Two specific factors which affect the probability of stochastic biological effects is the radiation type and radiation energy. Radiation type refers to the particle which deposits energy. There are hundreds of potential types of radiation but common radiation types are electrons, photons, alpha particles, neutrons and photons. Radiation energy, another factor which influences biological effect, refers to the energy associated with the radiation and is usually expressed in electron volts.

In 1931, the term relative biological effectiveness (RBE) was first described by two radiologists, Failla and Henshaw. In this article, the authors noted varying degrees of biological effect resulting from the same absorbed dose of two different types of radiation (Failla and Henshaw, 1931). They coined the term RBE to quantify the difference in biological effect between two radiations. The relative biological effectiveness for a specific radiation (T) is defined as:

$$RBE(T) = \frac{\begin{array}{c}Dose\ of\ reference\ radiation \\ required\ to\ produce \\ a\ specific\ level\ of\ response\end{array}}{\begin{array}{c}Dose\ of\ radiation\ A \\ required\ to\ produce \\ an\ equal\ response\end{array}} \qquad \textbf{Equation 1}$$

where all experimental variables except the reference radiation type are held constant. In this particular study, the experimenters investigated differences between x-rays and gamma rays.

Later, in 1952, a relationship between the spatial distribution of energy deposition and RBE was reported (Zirkle *et al).* Zirkle coined the term 'linear energy transfer' (LET) which describes the density of ionizations as energy loss per unit path of a charged particle. While investigating the effect of radiation on the survival of mold spores, high LET radiation was found to generally have a higher RBE than lower LET radiation (Zirkle et al, 1952).

Shortly after World War II, the International Commission on Radiological Protection (ICRP) published weighting factor based upon RBE measurements at the time to allow for comparison and addition of irradiation scenarios. They used the term 'relative biological efficiency' for this weighting factor in their 1951 report (ICRP, 1951). The relative biological efficiency factors recommended in this report were from 'considerations of the equivalent energy absorbed in tissue coupled with the relative biological efficiency'. The values in Table 1 were recommended in this report.

The reference radiation for the values in Table 1 was defined to be gamma radiation from radium filtered by 0.5 mm of platinum. The RBE values were assumed to be constant for biological effects including superficial injuries, production of 'anameia and leukemia', malignant tumors, cataracts, obesity, infertility, reduction of lifespan and genetic effects.

Table 1 - RBE recommendations from ICRP 1951

Radiation	RBE
Gamma rays from radium	1
Electrons	1
x-rays from 0.1-3 MeV	1
Fast neutrons < 20 MeV	10
Alpha particles	20
Protons	10

The ICRP recommended a relaxation in choice of reference radiation in 1955. In addition to radium gamma rays, they recommended that 'ordinary x-rays' could also be used as the reference radiation with an RBE of 1. Ordinary x-rays were defined as x-rays which produced 100 ionizations per micron or deposited an average of 3.5 keV per micron of water.

In 1959, the ICRP recommended that term RBE be dropped from use in radiation protection and instead recommended another name to be used. They recommended the term radiation quality factor (QF). This factor was to be based entirely on radiation LET and was to be used to provide a common scale for all ionizing radiations. They also defined another quantity called the dose equivalent which was taken as the product of dose D and quality factor QF. Thus, at this time RBE is only used in the field of radiation protection through the quality factor and the radiation weighting factor.

The choice of reference radiation was again relaxed in ICRP publication 60 (ICRP, 1991) where any low-LET radiation could be used as the reference radiation for the radiation weighting factor. This choice suggests that the variation in biological effectiveness between photons and electrons of any energy is not significant enough to require differentiation in radiation weighting factors. However, it should be noted that this relaxation does not extend to RBE measurements. ICRP publication 60 acknowledges the differences in LET between various photon sources as shown in Figure 1 where the unrestricted LET of Co-60 is about an order of magnitude smaller than that of 30 kVp x-rays. (Dietze *et al.*, 2004)

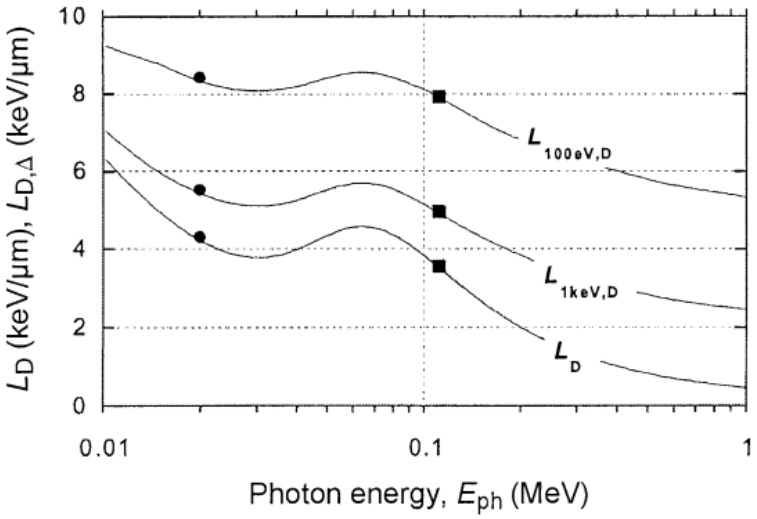

Figure 1 Average restricted and unrestricted LET for monoenergetic photons. 30 kVp and 200 kVp x-ray LET values are displayed as dots and squares respectively.

In ICRP publication 92 (ICRP, 2003), hard gamma rays are suggested as a convenient reference radiation because of practical considerations. Several reasons are quoted including, the precedent of using hard gammas, availability of epidemiological data related to hard gammas, the relatively low LET and the tendency for more uniformity dose distributions.

Current ICRP recommendations for the radiation weighting factor can be found in publication 103 (ICRP, 2007) and are shown below:

Table 2 - Current radiation weighting factors w_R (ICRP Publication 103)

Radiation Type	Radiation Weighting Factor
Photons	1
Electrons and muons	1
Protons and charged pions	2
Alpha Particles	20
Fission Fragments	20
Heavy Ions	20
Neutrons	A continuous function

Publication 103 notes that the electron weighting factor does not address Auger electrons. One can refer to Publication 103 (ICRP, 2007) for the neutron weighting factor continuous function.

The use of the weighting factor remains as a quantity which allows different radiations to be measured on the same scale of biological detriment. To determine equivalent dose, the absorbed dose D is multiplied by the weighting factor w_R. The total equivalent dose is found by a summation over all radiations as in Equation 2.

$$H_t = \sum_R w_R D_{T,R} \qquad \textbf{Equation 2}$$

It is important to note that radiation weighting factors are designed for the purposes of radiation protection and are not applicable for specific risk assessments. This assertion is explicitly stated in ICRP publication 92 (ICRP, 2003) paragraph 82: w_R is designed for the practice of radiological protection, not for specific risk assessment. Even the RBE values from experimental systems have limited applicability to risk assessment. For example, it would be inappropriate to base cost-benefit considerations for mammography screening primarily on risk estimates for gamma rays and RBE values, rather than using the relevant epidemiological data for x-rays.

There are two experimental methods for determining RBE: a low-dose method and a high dose method. Of these two, only the low-dose method is relevant to this work. The low dose method calculates RBE values under the conditions of low-dose and low dose rate. Since RBE is largest under these conditions (ICRP, 2003), these values are labeled as RBE_M. The method recommended by the National Council on Radiation Protection (NCRP, 1990) to determine RBE_M is to find the ratio of the linear coefficients of the dose-response fit. This approach has been used in several experimental attempts to find RBE values.

One such paper **(**Mestres *et al.,* 2008*),* involved the use of florescence in-situ hybridization to quantify DNA damage to cells from a human blood sample irradiated by x-rays. Blood samples taken from a 40 year old human male were cultured in RPMI-1640 medium, calf serum, antibiotics and other supplements. Portions of the culture were then placed in specially designed containers to attempt homogenous irradiation. The samples were then exposed to x-rays from a Therapax model source in one of three configurations: (120 kVp, 1.3mm Al, 0.3 mm copper), (80 kVp, 2mm Al) and (30 kVp,

0.8 mm Al). The samples were irradiated to 0.05, 0.1, 0.2, 0.4, 0.6, 0.7, 0.8, 1, 2 and 3 Gy at 1.15, 0.95 and 0.25 Gy min^{-1} dose rates for the 120, 80 and 30 kVp sources respectively. The dose measurements were performed using a M23342 ionization chamber and a Unidose electrometer model 1001. Chromosome aberrations were then quantified by florescence *in situ* hybridization. Using 120 kVp x-rays as a reference radiation, the RBE for 80 kVp x-rays was reported to be 1.08 ± 0.4 for dicentric aberrations and 1.26 ± 0.4 in the case of 30 kVp x-rays (Mestres *et al.*, 2008).

Another recent experimental paper investigating low-LET RBE (Beyruther *et al.*, 2009) investigated the RBE of low tube voltage x-rays. They found an RBE of 1.3 ± 0.2 and 1.7 ± 0.3 for 25 kV and 10 kV x-rays respectively. In this particular study the experimenters used two types of human mammary glands, MCF-12A and 184A1. The cells were independently placed in a growth medium and allowed to incubate for 12 days and then were prepared for irradiation. For the reference radiation, the cells were irradiated an Isovolt x-ray tube operated at 200 kV with a tungsten anode, Be filtration and additional Cu filtration. The cells were placed at a 45 cm focus to cell distance. Dosimetry was performed with a Unidose dosimeter and an ionization chamber. For the soft x-rays, a Darpac x-ray tube was used at 25 kV and 10 kV with a Be filter. The focus to cell distance was 25 cm in this case. The dose rates were measured with an ionization chamber and a Unidose dosimeter. The cells were irradiated through the bottom of the flasks. The dose distribution was verified using Gaf-Chromic dosimetry films and the variation was found to be lower than 4% in all cases. To account for the attenuation through the bottom of the flask, a dose versus depth correction was used. It is unclear how this correction was developed. Acentric, dicentric and centric aberration analyses

were performed using a microscope at 1000 magnification. The number of cells ring aberrations and dicentric aberrations were tallied for various doses. The data were then fitted to a linear quadratic dose response curve and RBE values were calculated based upon these fits. The dose values used for irradiation were 0, 0.5, 1, 2, 3 and 5 Gy for the reference radiation and similar values for the soft x-rays (Beyruther *et a.l,* 2009).

Another experimental study making use of the micronuclei formation and survival as a biological endpoint, "RBE of 25 kV x-rays for the survival and induction of micronuclei in the human mammary epithelial cell line MCD – 12A", was conducted by Lenhert *et al.* In this work the authors investigated micronucleus formation as a result of x-ray irradiation. In particular the RBE of 25 kV x-rays was determined with 200 kV x-rays as a reference radiation. Mammary gland cell line MCF-12A was chosen for the cell culture. The cells were incubated in culture flasks with a base of 25 cm^2 for several days. The monolayer cultures were irradiated with doses ranging from 0.5 to 3.5 Gy. After irradiation, the cultures were immediately treated, stained, and examined under a light microscope. From these cultures, the fraction of bi-nucleated cells and bi-nucleated cells with micronuclei was determined. Irradiation was performed with an Isovolt x-ray tube and a Darpac x-ray tube for the reference radiation and the test radiation respectively. The reference radiation with filtered with the inherent 7mm Be along with a 0.5 mm Cu filter while the test radiation was filtered with 2mm inherent Be along with a 0.3 mm Al filter. The cultures were irradiated through the base of the flask so there was an additional 1mm plastic attenuator in all irradiation cases. Irradiation times did not exceed 4 minutes. Dose measurements were performed using an ionization chamber and

a Unidose dosimeter. One of the main results, RBE vs. survival fraction, has been displayed in Figure 2. RBE values were determined from the linear coefficients to a linear quadratic fit on the data (Lenhert *et al*, 2006).

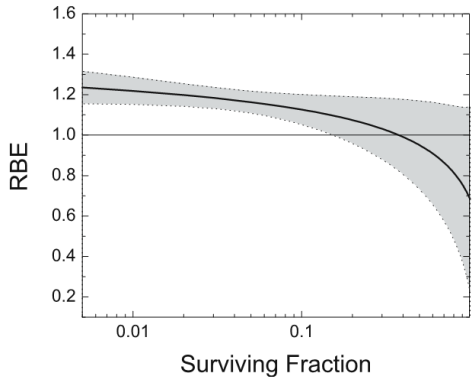

Figure 2 – The RBE dependence on the survival fraction for 25 kV x-rays relative to 200 kV x-rays. The grey shading represents the 95% confidence interval (Lenhert *et al.* 2006).

There are hundreds of other experimental RBE studies in addition to the previous three and an exhaustive review would not be appropriate for this section. There are published RBE reviews (Nikjoo 2010, Little 2008) and further details can be found there and in their respective references.

Another technique for quantifying biological effect makes use of computers to model the effect of radiation on DNA. Monte Carlo electron transport codes facilitate this effort by using water as a surrogate for tissue. Monte Carlo electron transport codes simulate the transport of electrons providing an event by event description of energy deposition. These codes have been used to improve our understanding of radiation-tissue interactions by allowing initial cell damage to be estimated. While biological effect is affected by many factors such as cell type, endpoint and scavenger concentrations, it is also affected by radiation quality and thus characterizing the electron track is an

important step in understanding low-LET radiation effects and Monte Carlo codes aid in this process. NOREC (Semenenko *et al.* 2003*)* , a predecessor of OREC (Wright *et al.*, 1983), simulates the deposition of energy into water by using ionization and excitation cross section databases. For each collision, the code decides whether an ionization event, an excitation or an elastic scattering event occurs. If an ionization event is occurs, the code then computes the energy of the secondary electron and tracks it fully. If an excitation event occurs, the code then determines which excitation state was produced and how much energy is deposited. Lastly, in the case of an elastic scatter, the code registers the events and updates the energy of the energetic electron. For very low energy electrons, elastic scattering is dominant while at energies above 1 keV, ionizing events dominate the deposition spectrum. For a single electron track, NOREC provides the following details on every deposition event including particle order (primary, secondary, etc), interaction type (excitation, ionization, and elastic), Cartesian coordinates and the energy deposited (Nikjoo 2006).

Often, computational studies on radiation induced damage include a DNA model which is used in conjunction with the radiation code. The complexity of the models vary greatly- from a line to as complicated as a full atomistic model of the entire genome. On the smallest scale, DNA is composed of two sugar-phosphate strands which exist in an anti-parallel configuration. At each site on the strands one of four bases may be attached: Adenine, Cytosine, Thiamine and Guanine. The longest human chromosome is approximately 220 million base pairs long. These long strands of DNA undergo several orders of folding and the most basic folding configuration is the double helix. In this configuration, DNA strands forms a right-handed double helix structure which is about

20 angstroms in diameter and there are 10 base pairs contained in each 34 angstrom helical pitch (3.4 angstrom distance between base pairs). The double helix may be folded into a more compact configuration called the nucleosome. In the nucleosome configuration, eight histone proteins come together to form a spool like structure around which the DNA is wrapped to form the nucleosome configuration. When combined, the eight histone proteins are 11 nm in diameter and are each surrounded by 200 base pairs of DNA. The packing ratio of DNA is the length of unfolded DNA divided by the length of folded DNA. The packing ratio of DNA in the nucleosome configuration is around 6. A packing ratio 40 is estimated for the next level of DNA folding. In the chromatin fiber configuration, the nucleosome itself arranges into a tight spiral with a diameter of 30 nm and about 5 nucleosomes per turn and a 11 nm pitch. It is this configuration which is used in the current study to model DSB yields as it represents the first level of folding in a transcriptionally inactive nucleus. Some details about the 30 nm chromatin fiber's configuration are still under scientific debate due to difficulty in imaging this structure (Staynov, 2008).

In 2001, a Monte Carlo electron track simulator was used to generate electron tracks and the subsequent chemical track thereby estimating simple and complex double strand breaks *(*Nikjoo *et al.* 2001*).* This program provided the spatial location of interactions, energy deposited by each interaction and the type of interaction. These tracks were generated using liquid water as a tissue surrogate. A virtual cylinder was used to enclose each track in such a way that there was charge equilibrium within the cylinder. Next, linear segments of DNA were randomly placed within the cylinder. Direct and indirect hits were tallied for each linear segment of DNA noting the relative position of

each interaction with DNA. Damage sites were then classified according to the scheme described in Figure 3. In this figure SSB, SSB*, DSB, DSB* and DSB** break configurations are described.

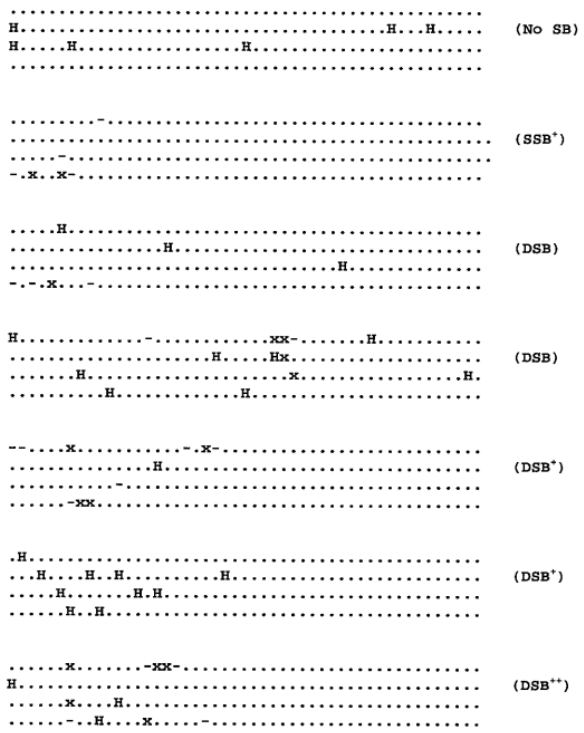

Figure 3 - DNA damage site classification scheme describing SSB, SSB*, DSB, DSB* and DSB. Dashes "-" denote hits which caused no strand damage. "H" symboles represent damage due to hydroxyl radical and the "x" denotes direct deposition damage. (Charlton *et al* 1989)**

Simulations in this investigation show that the majority of DNA breaks are of a simple type. For low energy electrons, about 20% -30% of the breaks are complex. The damage associated with DNA strand breaks shifts towards greater complexity as LET increases. This trend is best seen as the proportion of DSB* to DSB increases for higher LET radiation.

Later on in 2008, Freidland used a detailed model of DNA which is based upon a spherical chromatin domain model to simulate radiation induced biological effect. Each chromosome of the human genome is modeled by a chain of spherical 1 Mbp chromatin clusters with a 500 nm diameter (Friedland *et al.,* 2008). The spherical chromatin domains are not physically connected, but are linked with an entropic spring potential to approximate the real behavior of DNA. The DNA target used for radiation simulation was approximately 6 Gbp composed of 6070 spherical chromatin domains. The Monte Carlo code PARTRAC (Dingfelder *et al.,* 1998) was used to generate radiation tracks which begin with a primary ions and ends after total energy deposition. PARTRAC makes use of water cross sections for ionization and excitation processes and these cross sections are energy and angular dependent. When PARTRAC was compared to experimental benchmarks such as stopping power and radial dose distribution, good agreement was found. This model relied on other scientific results for parameters such as DSB yield, SSB/DSB ratio and a direct/indirect effect ratio. The probability for DNA strand break induction was assumed to increase linearly from 0 at 5 eV to 1 at 35.7 eV deposited energy within a base. DSB induction was assumed whenever two SSBs occurred within 10 base pairs on opposite DNA strands. Additionally, DSB induction was assumed to occur after any SSB event with a 0.01 probability. Electron and photon irradiation was not the focus of this paper. Instead, emphasis was placed on heavy ions such as protons and alpha particles. The authors reported DSB yields as a function of LET, DNA fragment size yields and dose response curves for chromosomal aberrations (Freidland *et al.,* 2008).

At its heart, radiation biophysics can be summarized into several stages of radiation induced biological damage. The process is initiated by the initial interaction of photons, charged particles or uncharged particles (or some combination of these) with body tissues. These initial interactions are responsible for some spatial and temporal distribution in the organism and these energy deposition events may then lead to the production of chemically active species such as electrons, ions and radicals. Both the initial energy deposition from the incident radiation or the subsequently produced chemical species may interact with important biological structures such as DNA to disrupt regular tissue function. This disruption may be in one of several forms including damage to important molecules, influence on repair, protection or recovery processes, influence on cell survival or the viability of cell daughters or finally, damaged genes. It is unfortunate that our current knowledge and understanding does not accurately extend far beyond the chemical stage of this process. Despite this, with certain reasonable assumptions, fairly accurate predictions can be made about various outcomes.

CHAPTER 3

METHOD

In this work, photon and electron RBE were determined using a detailed biological model of DNA in the chromatin fiber form in conjunction with electron track modeling. The biological endpoint chosen was DSB yield and this was estimated primarily by a new method of characterizing the distances between ionizations in the track. This method involves estimating the likelihood of two arbitrary ionizations in a given electron track would be separated by a particular distance. This separation function was determined for electrons of varying starting energy. In conjunction with this track characterization, the probability that ionizations would cause an additional SSB given that a SSB has occurred was next estimated using the biological model and reactive species diffusion data. Using these two functions, the SSB/DSB ratio and subsequently the DSB yield was then calculated for monoenergetic electrons. By choosing the reference radiation to be 1 MeV electrons, the RBE is determined for monoenergetic electrons. Once RBE is known for single energy electrons of arbitrary energy, then nuclides which emit beta radiation can then be analyzed. Using the energy-intensity data from nuclear tables to weigh the electron and photon RBE values, the RBE of the radionuclide's radiological emission is determined. Monoenergetic photon RBE is next

determined. Using photoelectric, Compton scatter and pair production cross sections, the resulting initial electron energy spectrum is determined. This spectrum is then folded over monoenergetic electron RBE to determine the photon RBE. Once photon RBE is established for as a function of energy, x-ray sources are then investigated to determine their RBE. The spectra for x-rays are computed by MCNP simulation and the spectra are folded over monoenergetic photon RBE to determine the resulting x-ray RBE.

By the standard definition, the RBE of some test radiation (*T*) is defined as the quotient of the dose of some reference radiation (*R*) and the same dose of the test radiation required to produce an identical biological effect. This definition is represented in Equation 3 where D_R represents the dose of the reference radiation required to produce some biological effect and D_T represents the dose of the test radiation required to produce an identical effect with all other variables held constant.

$$RBE(T) = \frac{D_R}{D_T} \qquad \textbf{Equation 3}$$

That is, the relative biological effectiveness of some test radiation *T* relative to some reference radiation *R* is the quotient of the dose of *R* and the dose of *T* if both doses produce an identical biological response. An accepted approximation of the dose response curve is the linear-quadratic model which states that the biological response to radiation has both a linear component and a quadratic component. The linear coefficient of this fit is represented by α while the quadratic component is represented by β as seen in Equation 4:

$$E(D) = \alpha D + \beta D^2 \qquad \textbf{Equation 4}$$

where E represents the biological effect after some radiation dose *D* is administered. The linear-quadratic model assumes that at low dose, the effect of radiation increases linearly.

At high dose, the model assumes quadratic growth in biological effect. A new quantity, is RBE_M defined by the NCRP (NCRP, 1990) to be the RBE of a radiation under the assumption of low dose; i.e. where the linear term of the linear-quadratic expression dominates. Thus in estimating RBE_M the following approximation was used:

$$E(D) = \alpha D \qquad \textbf{Equation 5}$$

The justification for this assumption lies in the behavior of a second order polynomial. At high doses, the quadratic term will dominate the effect while at low dose, the quadratic term is insignificant relative to the linear term. Based upon this, the quadratic term is dropped resulting in Equation 5 restricting the RBE estimates in this work to low dose. Rearranging Equation 5 to express dose D in terms of effect E yields the following equation:

$$D = \frac{E}{\alpha} \qquad \textbf{Equation 6}$$

Substituting this expression for dose into Equation 3 yields an expression for RBE under the low-dose assumption. Here E_R and E_T represent the effect of the reference and test radiation respectively. α_R and α_T represent the linear coefficients in the dose response curve of the reference radiation and the test radiation respectively.

$$RBE_M(T) = \frac{\frac{E_R}{\alpha_R}}{\frac{E_T}{\alpha_T}} \qquad \textbf{Equation 7}$$

Since E_R and E_T are by definition equal, the following simplifications can be made:

$$RBE_M(T) = \frac{\frac{1}{\alpha_R}}{\frac{1}{\alpha_T}}$$ **Equation 8**

and

$$RBE_M(T) = \frac{\alpha_T}{\alpha_R}$$ **Equation 9**

That is, the RBE_M of some test radiation T relative to some reference radiation R is the quotient of the linear coefficients of the dose – response curves. RBE_M represents the RBE value under a low-dose assumption. Here, low-dose refers to dose ranges where the linear term, α, is the dominant expression in the linear-quadratic fit.

The biological endpoint used in this method is the number of double strand DNA breaks. With this endpoint, according to Equation 5, the unit for α is DSB Gy^{-1}. That is since α is the linear term of the dose response curve, it can be considered to be the number of double strand breaks induced after one joule of radiation is deposited in one kilogram of tissue. It is assumed that a double strand break is induced in DNA when two or more single strand breaks on opposite sugar phosphate strands occur within 10 base pairs. Therefore, we can approximate α as the product of the number of single strand breaks with the probability that a single strand break is converted to a double strand break. Additionally, because a double strand break is composed of two or more single strand breaks, the average number of single strand breaks in a double strand break ($\frac{1}{\tau}$) is needed to correctly of the DSB yield. Mathematically, the linear coefficient in the dose response curve (α) is directly proportional to the SSB yield, SSB(E) and probability that a single strand break is converted to a DSB, P(T).

$$\alpha = SSB(E)\, P\, \tau$$ **Equation 10**

That is, α is approximately equal to the number of SSBs per gray induced by an electron with energy E (SSB(E)) multiplied by the probability that a SSB is converted to a DSB.

In order to estimate α, the probability that a SSB is converted to a DSB, P must be calculated. A DSB is assumed to occur when two or more SSBs interact within 10 base pairs on the DNA molecule and SSBs occur when ionizations in the track successfully interact with DNA. Given the number of ionizations in an electron track (N) and the probability of successfully interacting with the DNA, termed , then the binomial distribution can be used to estimate the total probability P that an arbitrary SSB is converted to a DSB as follows:

$$\mathrm{P} = \sum_{i=1}^{\mathbf{N}} \binom{\mathrm{N}}{i} \chi^{\boldsymbol{i}} (1-\chi)^{\mathrm{N}-i} \qquad \textbf{Equation 11}$$

Here P represents the SSB to DSB conversion probability, N represents the total number of ionizations in the track, χ represents the probability that a random ionization in the track successfully causes a SSB.

It is noted that the binomial distribution is an approximation of P as there are at least two theoretical issues with this distribution. The first issue is that independence of successes is difficult to prove and is more than likely not strictly true. The second issue is that the number of ionizations in the electron track is not a fixed number, but itself a probabilistic distribution centered on a mean. In this work, the value used for N was taken as the closest integer value to the mean number of ionizations. In spite of these issues, the binomial distribution was used as no superior alternative was available. The DSB yield values predicted by using the binomial distribution fall within experimentally determined parameters.

χ is approximated by determining the probability that two ionizations in an electron track are separated by some distance r and is a new method of characterizing the electron track which is more detailed yet related to the concepts of LET. To calculate χ, the quantity, $\theta_E(r)$, which represents the average number of ionizations located in the distance interval *(r, r+dr)* from an arbitrary ionization in the electron track is used. Intuitively, the electron track was characterized in this manner because two ionizations separated by a small distance relative to the width of DNA are more likely to cause a DSB than sparsely spaced ionization pairs. The calculational model which was used to estimate $\theta_E(r)$ is described in the next section.

Another function, $\xi(r)$, is needed to determine χ by weighing the importance of two ionizations separated by some known distance relative to causing a DSB break. This function $\xi(r)$, represents the probability that two ionizations will cause a DSB given that one of the ionization events has already caused a SSB. Intuitively, this function assesses the importance of ionization pairs with respect to DNA damage. Ionization pairs separated by a 'large' distance could form two distance SSBs but they cannot form a DSB. Ionization pairs which are separated by a short distance, of the order of the width of DNA, are likely to form DSBs.

Together, $\theta_E(r)$ and $\xi(r)$ can be used to assess how likely an electron track is to form DSB relative to SSBs. By integrating these two functions over all distances, the probability that an arbitrary ionization pair will form an additional SSB χ_e can be determined as follows:

$$\chi_e = \int_0^\infty \theta_e(r)\xi(r)\,\mathrm{d}r \qquad \textbf{Equation 12}$$

This allows for a more detailed definition of P by substituting Equation 13 into the previous definition of P:

$$\mathrm{P} = \sum_{i=1}^{\mathbf{N}} \binom{\mathrm{N}}{i} \left[\int_{\mathbf{0}}^{\infty} \theta_{\boldsymbol{e}}(r)\xi(r)\,\mathrm{d}r\right]^{\boldsymbol{i}} \left(1 - \left[\int_{\mathbf{0}}^{\infty} \theta_{\boldsymbol{e}}(r)\xi(r)\,\mathrm{d}r\right]\right)^{\mathrm{N}-i} \qquad \textbf{Equation 13}$$

This in turn allows for a more detailed definition of α:

$$\alpha = SSB(T) \sum_{i=1}^{\mathbf{N}} \binom{\mathrm{N}}{i} \left[\int_{\mathbf{0}}^{\infty} \theta_{\boldsymbol{e}}(r)\xi(r)\,\mathrm{d}r\right]^{\boldsymbol{i}} \left(1 - \left[\int_{\mathbf{0}}^{\infty} \theta_{\boldsymbol{e}}(r)\xi(r)\,\mathrm{d}r\right]\right)^{\mathrm{N}-i} \tau \qquad \textbf{Equation 14}$$

Substituting Equation 11 and Equation 9 into Equation 10 gives the following expression for RBE:

$$RBE_M(T) = \frac{SSB(T) \sum_{i=1}^{N_T} \binom{N_T}{i} \chi_{\boldsymbol{T}}{}^{\boldsymbol{i}} (1-\chi_T)^{N_T - i} \tau}{SSB(R) \sum_{i=1}^{N_R} \binom{N_R}{i} \chi_{\boldsymbol{R}}{}^{\boldsymbol{i}} (1-\chi_R)^{N_R - i} \tau} \qquad \textbf{Equation 15}$$

Finally, substituting Equation 12 into Equation 15 yields the complete expression for $\mathrm{RBE_M}$ using 1 MeV electrons as the reference radiation leads to equation 16. Here it is assumed that τ is roughly equal in the test radiation and the reference radiation. While there is some variation in the break complexity as a function of energy, this value remains relatively constant as shown in the break complexity section of the results. The full expression for $\mathrm{RBE_M}$ is shown below:

$$RBE_M(T) = \frac{SSB(T) \sum_{i=1}^{N_T} \binom{N_T}{i} \left[\int_{\mathbf{0}}^{\infty} \theta_{\boldsymbol{T}}(r)\xi(r)\,\mathrm{d}r\right]^{\boldsymbol{i}} \left(1 - \left[\int_{\mathbf{0}}^{\infty} \theta_{\boldsymbol{T}}(r)\xi(r)\,\mathrm{d}r\right]\right)^{N_T - i}}{SSB(R) \sum_{i=1}^{N_R} \binom{N_R}{i} \left[\int_{\mathbf{0}}^{\infty} \theta_{\boldsymbol{T}}(r)\xi(r)\,\mathrm{d}r\right]^{\boldsymbol{i}} \left(1 - \left[\int_{\mathbf{0}}^{\infty} \theta_{\boldsymbol{T}}(r)\xi(r)\,\mathrm{d}r\right]\right)^{N_R - i}} \qquad \textbf{16}$$

In the following section, computational methods, all of the variables are approximated.

Several assumptions were made leading up to the final expression for electron RBE_M. First, a double strand break (DSB) was assumed to occur when two single strand breaks (SSB) occur within 10 base pairs on opposite DNA strands (Friedland *et al*, 2008). Next, the average yield of SSB per absorbed dose per base pair was taken from experiment (Millar 1981, Moiseenko 1998). Related to this, the average yield of SSB per absorbed dose was assumed to be directly proportional to the number of ionizations per absorbed dose (Friedland *et al*, 2008). Double strand breaks were only considered from ionizations arising from a single electron track. (Goodhead 2006). To aid in estimating, the ratio of single strand breaks resulting from direct effects to indirect effects was assumed to be 35:65 (B Michael and P O'Neill, 2000). The binomial distribution requires assumption of the independence of trials. Finally, the initial locations of electron tracks were assumed to be random relative to DNA molecules.

RBE values for monoenergetic photons were determined after RBE_M for monoenergetic electrons was calculated. The spectrum of initial electrons produced by a photon was simulated using the interaction cross sections of water. In order to accomplish this, the photoelectric, Compton scattering and pair production cross sections of water and, isotropic scattering in the center of mass frame for Compton scattering. To determining the initial electron spectrum, a computer program was written which contained a Klien-Nishina related class, a water cross section class and a photon class. The photon class tracked the energy of the photon and returned the energy of any electrons produced. The Klein-Nishina class returned a lab angle of the recoiled electron under the assumption of isotropic scatter in the center of mass frame. Finally, the cross-

section class returned the cross section values of Compton scatter, photoelectric scatter and pair production scatter. The cross section class also returned the probabilities that the next collision would either be pair production, Compton scatter or photoelectric effect as a function of photon energy. Finally, this class returned a randomized collision type based upon the photon energy. Photons were initialized with a fixed energy and were tracked until all of the energy was converted to electron kinetic energy. Multiple Compton scatters were allowed as well as full tracking of positrons and electrons produced by pair production events. In all cases the energies of all electrons and positrons produced were tracked and used to produce the initial electron spectrum. Positrons were treated the same as electrons in this study. To produce a single initial electron spectrum for a monoenergetic photon, multiple photons were tracked and histogrammed until convergence was achieved in the final spectrum. The total energy of the electron formed was equal to the initial photon energy in all cases. Typically, over 10000 iterations were needed to produce a converged electron spectrum. The number of electrons produced at a specific energy for several photons interacting in water has been shown below in Figure 4. At 1 MeV, few electrons are formed at full energy because of the low probability of photoelectric interaction at this energy. Instead, electrons are typically formed at energies under the characteristic energy of the Compton edge. However, at lower energies, such as 0.01 MeV most of the electrons are formed by photoelectric effect of the primary photon.

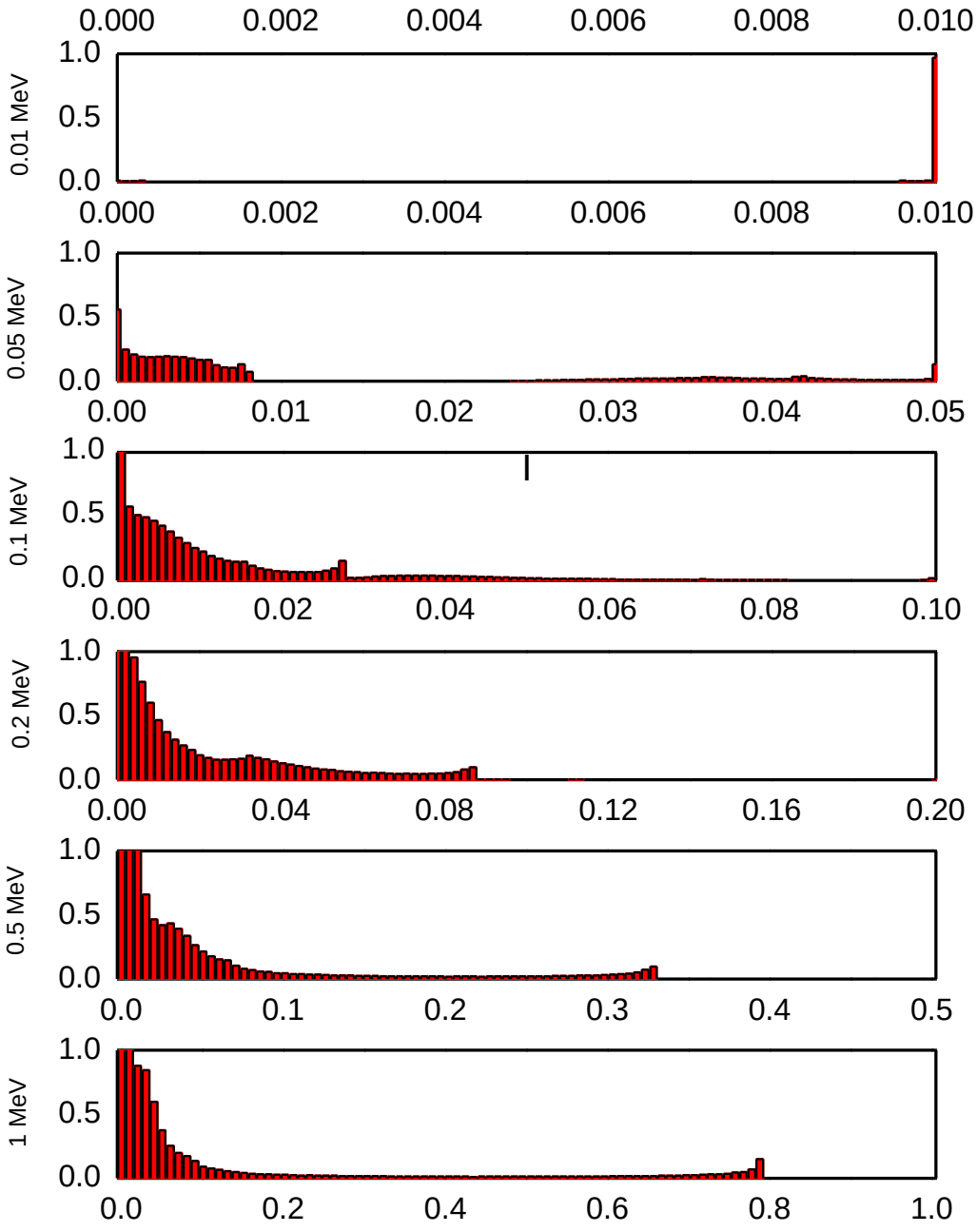

Figure 4 – Initial electron spectrum of several monoenergetic photons interacting in water. Photon energies from top to bottom: 1 MeV, 0.5 MeV, 0.2 MeV, 0.1 MeV, 0.05 MeV and 0.01 MeV.

Once the electron spectrum produced by photons was produced the RBE of monoenergetic photons was calculated as follows:

$$RBE_{\gamma}(E) = \frac{\int_0^{\infty} RBE_e(z)S(z,E)z\,dz}{\int_0^{\infty} S(z,E)z\,dz} \qquad \textbf{Equation 17}$$

where $RBE_e(z)$ represents the RBE of a monoenergetic electron with energy z, $S(z,E)$ represents the intensity of electrons of energy z produced from a photon of energy E.

Once the photon RBE value dataset is populated using Equation 17 and Equation 16, the RBE of photon sources such x-ray tubes can be estimated by using a photon dose weighting function. In this work, the RBE of photon sources is estimated using the following formula:

$$RBE_X(E) = \frac{\int_0^{\infty} RBE_{\gamma}(z)S(z)z\,dz}{\int_0^{\infty} S(z)z\,dz} \qquad \textbf{Equation 18}$$

where $RBE_X(z)$ represents the RBE of a monoenergetic electron with energy z, $S(z)$ represents the intensity of photons of energy z produced from the source.

The RBE of electron sources are also calculated using the dose weighted average which was used for photons. To calculate an RBE value for a beta source two things are needed: the monoenergetic RBE values for electrons and the energy vs. intensity spectrum of the beta source. The first dataset can be obtained using Equation 16 while beta source spectra may either calculated in some cases or obtained from published sources such as the ICRP publication 107 (ICRP 2009). The RBE values were calculated using the following dose weighted average formula:

$$RBE_{\beta}(E) = \frac{\int_0^{\infty} RBE_e(z)S(z)z\,dz}{\int_0^{\infty} S(z)z\,dz} \qquad \textbf{Equation 19}$$

where $RBE_e(z)$ represents the RBE of a monoenergetic electron with energy z, $S(z)$ represents the intensity of electrons of energy z produced from the beta source.

CHAPTER 4

MODELS

This section describes the computational models which estimate the unknown variable in the previous section. The first section of this chapter deals with the modeling of the electron track. Next the construction and parameters of the DNA model is addressed. Finally, the treatment of the photon, x-ray and radionuclide folding is described. The algorithms in this section are summarized Figure 6, Figure 7 and Figure 8 and the full C++ and Python implementations can be found in the appendix.

An electron propagating through tissue may leave a track of ionization and excitations whereby every one of the ionization in the track will be separated from other ionizations by varying distances. For a particular ionization, there may be ionizations which are separated by a close distance (on the order of 3nm) or ionizations which are much further. In light of this, an electron track is characterized in this work by the yield of ionization pairs as a function of inter-ionization distance, $\theta_e(r)$ as seen in Equation 12 and 16. How $\theta_e(r)$ fits into the electron RBE framework was discussed in the previous chapter and is also shown in Figure 5 - Flowchart description of electron RBE algorithm

In this approach, the ionization density, $\theta_e(r)$, was characterized by examining the distance between two arbitrary ionizations in the electron track. The quantity $\theta_E(r)\,dr$ was defined as the probability that two arbitrary ionizations will be separated by a distance in $(r, r+dr)$. This information allows one to estimate the fraction of ionizations with close neighbors. Events with several close neighbors can be considered to be part of an ionization cluster. Thus, radiation which is efficient at producing pairs of events separated by between 3 and 30 Å will be particularly effective at producing DSBs. However, if the radiation does not produces a pair of events which can diffuse to form two SSB within 10 base pairs, then this radiation cannot result in DSBs unless it does so by quantum resonant strand breakage (Boudaiffa 2008). Quantum resonant strand breakage has not been considered in this approach. For low energy electrons, there is a greater probability that events will closer together than those for higher energy electrons and this information would be contained within$\theta_E(r)$. The transport code NOREC (Semenenko 2003) was used to determine $\theta_E(r)$ as a function of initial electron energy E_0. Note, $\theta_E(r)$ depends only on the electron track ionization density and is independent of the DNA geometry and the diffusion of formed radicals. $\theta_E(r)$ has been shown for a few electron energies in Figure 10.

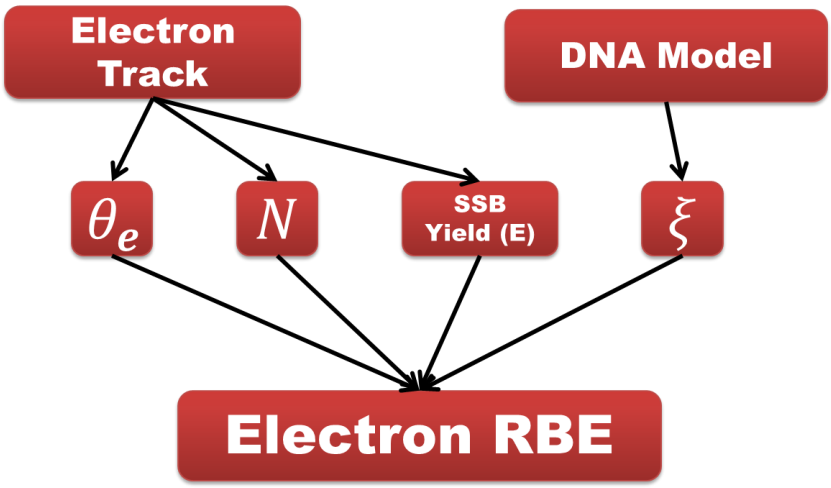

Figure 5 - Flowchart description of electron RBE algorithm

The yield of ionizations separated by a particular distance was investigated using electron track simulation software. The code chosen for this task was NOREC (Semenenko 2003,) because it is freely available, provides sufficient electron track details and has been publicly validated (2008 Dingfelder, Cho 2007, Nikjoo 2006, Seltzer 1991). For the purposes of this work, a C++ computer program was developed to compute the ionization pair yields. A nested loop has been used to iterate over all possible ionization pairs. Ionization pairs are then binned according to their separation distance. This process is repeated for several electron tracks and the average yield is recorded. The main rational behind this step in the method is to quantify how many "close" ionization pairs are produced by electrons of various energies. In this study, close ionizations are defined as those which may together interact to form a DSB. Ionizations which are separated by a large distance cannot interact with DNA to cause a DSB because of diffusion length restrictions. On the other hand, two 'nearby' ionizations may interact with DNA to cause

a DSB so determining the distribution of inter-ionization distances is an important step in calculating DSB yield and ultimately the RBE of electrons.

The program, named inter-ionization distance profiler, was written using C++. Because of NOREC library restrictions, this code can only be compiled using Microsoft Visual C++ Express edition 2008. This is likely because the code's author did not choose to release the source code, but rather released NOREC as a precompiled library which is compiler dependent. In programming the track profiler, a user defined data structure, labeled "Point", was first defined to store information about each energy deposition point in the electron track including the deposition type, the order of the depositing electron (primary, secondary, etc.), the Cartesian coordinates, the energy at the point of deposition, a special Boolean variable which records whether that particular ionization has already been considered in the profiling process and finally variables which store information related to the number and energy of the nearby ionizations were defined. Next, a histogram object was defined and initialized with the purpose of storing the inter-ionization track information in a flexible manner. A function which computes the distance between two "points" was defined using standard three dimensional Pythagoras theory.

Upon execution, the program reads command line variables which define the histogram, number of iterations and electron energy. After all variables are initialized, the program begins a loop over the specified number of ionizations. Within this loop, electron tracks are generated and stored using vector of points from the standard C++ library. Track related point information such as neighborhood energy is then computed. Next, two nested loops are constructed which iterate over every ionization pair in the

electron track, determining and histogramming the distance between each ionization pair. The histogram data are tested for validity, formatted then saved as a file for further analysis.

There are unique advantages to characterizing an electron track in this manner. The absolute number of ionization pairs produced is contained in the characterization. In the normalization used in this characterization, integrating the yield over all distances results in the total number of ionizations in the track. Also, other important quantities can be derived from this characterization including the fraction of ionizations with close neighbors.

The biological target is an important component of any computational study on radiation induced effects and in this work new parametric model of DNA based upon experimental parameters was constructed. Specifically, this DNA model was used exclusively to aid in estimating $\xi(r)$ (See Equation 15). This model was based upon experimentally measured parameters of DNA such as strand width, inter-base distance, double helix pitch and several others. A computer program which implements three-dimensional parametric equation theory was used to build the 30-nm chromatin fiber model used in this work.

Experimentally measured DNA parameters were used heavily in constructing this model. A right-handed double helix structure was used to model the unfolded DNA. In this configuration, the diameter of the double helix strand was set to 20 angstroms with a 34 angstrom helical pitch. That is traveling along the strand, for each complete turn of DNA, a distance of 34 angstroms would be covered. The inter-base-pair distance was set

to 3.4 angstroms. In modeling the first level of folding, the nucleosome, a continuous spiral with a 11 nm angstrom radius was used. Next, the nucleosome was then folded into the 30-nm chromatin fiber which had 5 nucleosomes per turn arranged in a helical structure (S. Neidle, 1999). The geometry of this model was based upon the solenoid model described in (Schiessel *et al*, 2001) and it does not make use of crossed liners described in (Woodcock *et al.*, 1993).

These published experimental parameters were integrated into solenoid model with the aid of a computer program written explicitly for this purpose. The full computer program has been included in Appendix D. After initializing the geometrical parameters, the program first implements the chromatin vectorization, using the chromatin radius and pitch. Next, the nucleosome vectorization is performed using the nucleosome pitch and radius while continually computing the appropriate rotational origin formed by the chromatin vectorization. The final vectorization performed is performed at the helix level which predicts the locations of the base-pair sugar-phosphate junctions. The entire 30 nm chromatin dataset is then plotted and exported to disk for further analysis.

A double strand break was assumed to be caused by two or more neighboring single strand breaks. Given that a single ionization event formed a *SSB*, the probability that any neighboring ionization event will form another nearby *SSB* was estimated by considering its distance from the original *SSB*. This probability is denoted as $\xi(r)$ where r is the distance between events. To estimate $\xi(r)$ the probability that an ionization event would either hit or diffuse to the DNA molecule within ten base pairs of the original SSB was calculated using three cases: 1) direct-direct, 2) indirect-indirect and 3) direct-

indirect. The first case estimates the probability that of additional SSB formation were both DNA interactions were direct energy depositions. The second case estimates the probability of additional SSB formation within 10 base pairs when the DNA interactions are of a mixed type and the last case estimates the probability when both DNA interactions results from reactive ion species interactions. An isotropic model was used for indirect effects so the rate of diffusion was assumed to be equal in all directions. Reactive radical diffusion was modeled using published lifetimes and diffusion distances from Terrissol (1990) and (Roots 1975). It was assumed that indirect action accounted for 44% of all SSBs (Milligan 1993) and the three cases were weighed accordingly. SSBs were assumed to be induced when a radical reacted within the volume the DNA sugar phosphate backbone. For direct effects, a SSB was assumed to be induced whenever the ionization event occurred within the volume of the DNA backbone described in the previously described DNA model. $\xi(r)$ was calculated by first determining probability than an arbitrary ionization event pair forms two single strand breaks in each of the three cases then determining the weighted average based upon a 0.44 probability of indirect action.

The SSB yield per unit absorbed dose was determined as a function of electron energy and denoted as SSB(T) as seen in Equation 10. In this work, the SSB yield was calculated assuming that an arbitrary ionization pair has a fixed probability of interacting with DNA to form a SSB. This probability was estimated from the number of ionization pairs per Joule for an electron of initial energy 1 MeV electrons along with the SSB yield of Co-60 from experiment. The first quantity, the average number of ionization pairs (IP)

per absorbed dose produced by a 1 MeV electron, was determined from a NOREC simulation and was found to be 2.4×10^{17} (IP J^{-1}). The second quantity, the average yield of SSB per absorbed dose per base pair for Co-60, was determined experimentally to be 8.4×10^{-8} (Gy BP)$^{-1}$ (Millar 1981, Moiseenko 1998). The probability of an ionization pair forming a single strand break (SSB BP^{-1} IP^{-1}) was calculated from the experimental SSB yield (SSB Gy^{-1} BP^{-1}) in conjunction with the simulated ionization yield (IP J^{-1}). Additional ionization yields were obtained from NOREC simulations to determine energy dependent SSB yields.

The spectrum of initial electrons produced by a photon can be simulated using the interaction cross sections of water. In order to accomplish this, the photoelectric, Compton scattering and pair production cross sections of water must be known and in this work, isotropic scattering in the center of mass frame for Compton scattering.

To determining the initial electron spectrum, a computer program was written which contained a Klien-Nishina related class, a water cross section class and a photon class. The photon class tracked the energy of the photon and returned the energy of any electrons produced. The Klien-Nishina class returned a lab angle of the recoiled electron under the assumption of isotropic scatter in the center of mass frame. Finally, the Cross-Section class returned the cross section values of Compton scatter, photoelectric scatter and pair production scatter. The cross section class also returned the probabilities that the next collision would either be pair production, Compton scatter or photoelectric effect as a function of photon energy. Finally, this class returned a randomized collision type based upon the photon energy.

In order to determine the RBE of an x-ray source the spectrum of the particular source must be known. X-ray spectra depend on several factors including tube voltage, beam angle, filter material, filter thickness. MCNPx simulation was used to determine the various x-ray spectra. The method outlined in (Ay, 2004) was used to as a basis for producing the spectra.

MCNPX was used to simulate the x-ray spectra for several tube voltages and filter materials. The source was set to a monoenergetic beam of electrons. The target was set to either tungsten or other electrode materials. A binned surface flux tally was implemented to determine the energy dependent flux of photons at the target. Statistical variance reduction implemented to speed up the simulation by encouraging additional production of bremsstrahlung photons. The resulting spectra were then folded over the photon RBE data to determine the x-ray RBE as described in Equation 18 and summarized in Figure 7 flowchart description of x-ray RBE algorithm.

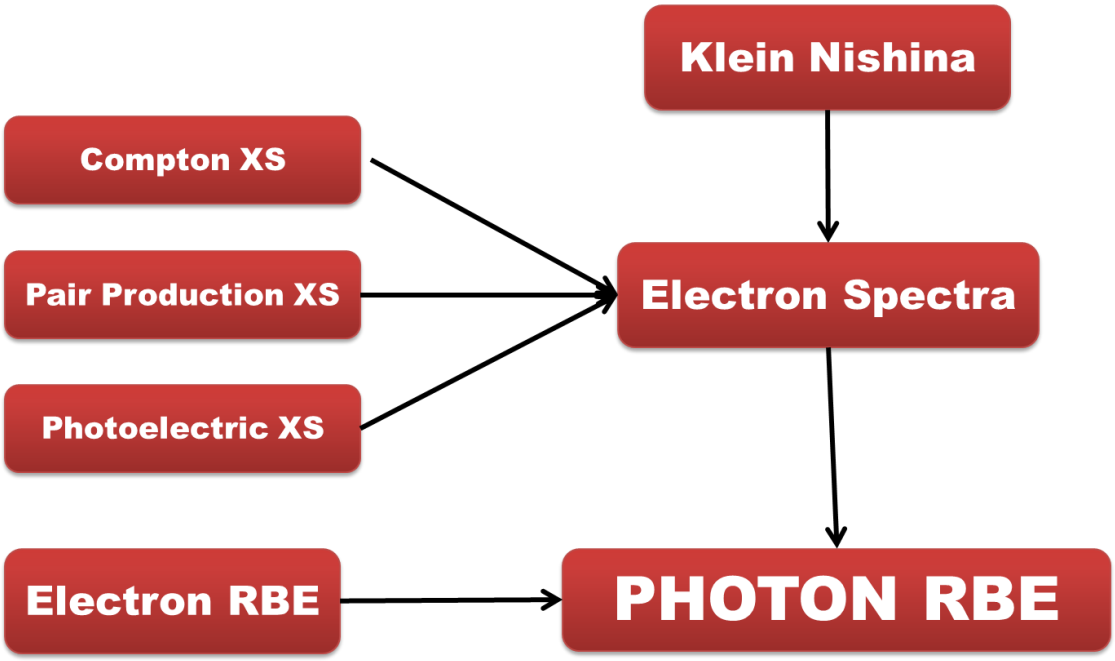

Figure 6 flow chart description of photon RBE description

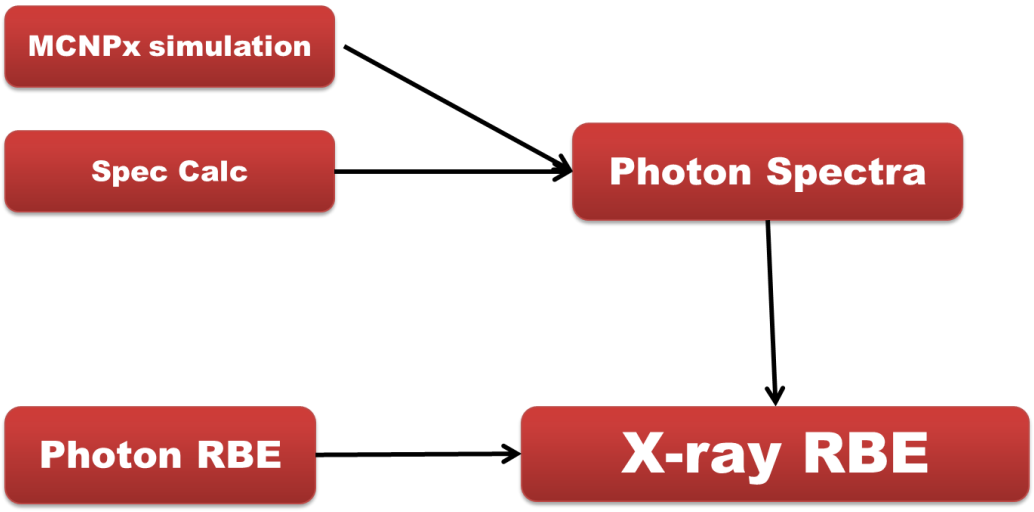

Figure 7 flowchart description of x-ray RBE algorithm

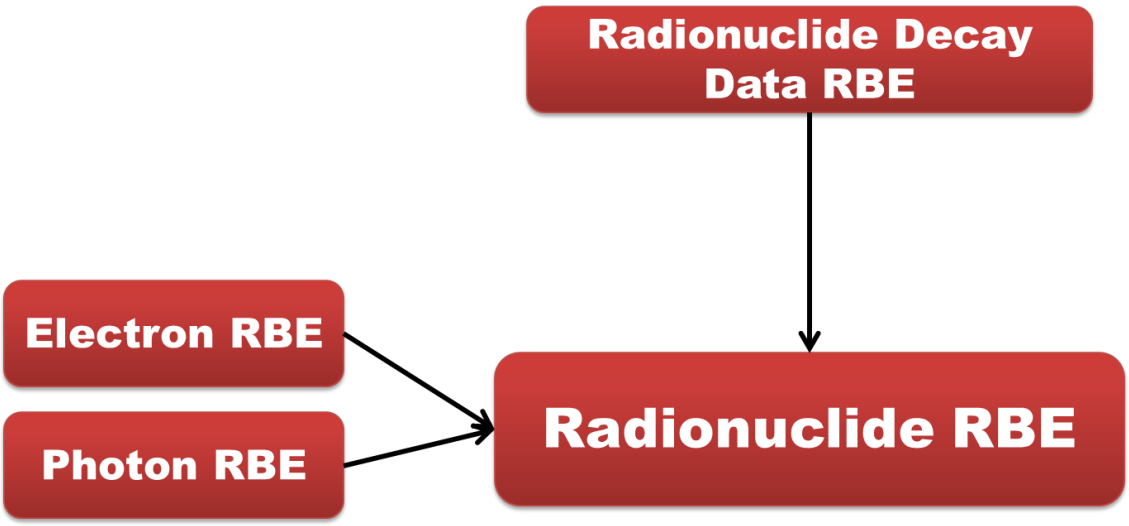

Figure 8 flowchart description of radionuclide RBE algorithm

CHAPTER 5

RESULTS

In this chapter, electron RBE, photon RBE, x-ray RBE and radionuclide RBE values in that order are presented. For electrons, preliminary results such as single strand DNA break yield as a function of electron energy, interionization distance yields, and double strand DNA break yields are first presented before the electron RBE values are shown. Next, photons are addressed starting with the electron spectra arising from photon irradiation and finishing with RBE values for monoenergetic photons. Finally x-ray and radionuclide RBE values are addressed.

The single strand break yield per unit dose as a function of monoenergetic electron energy is shown in Figure 9. The yield is in units of SSB per gray per DNA base pair. From 1 MeV to 1 keV , monoenergetic electron SSB yields stay relatively constant when comparing identical dose situations. However, the SSB yield drops quickly as the electron energies decrease from 1 keV to 10 eV.

A subset of the electron characterization results are shown in Figure 10 and Figure 11. These figures both describe how likely ionization pairs separated by a specified distance

occur. Five energies ranging from 500 eV to 1 MeV are Figure 10 with the expected number of ionizations on the y axis and inter-ionization distance shown on the x axis units of microns. In this figure, one can see that for a given dose, 500 eV electrons are particularly efficient at producing ionization pairs of this dimension relative to 1 MeV electrons. One can also see that 1 MeV electrons tend to produce less ionization pairs in this range relative to 50 keV electrons although the yields are comparable.

Similar ionization pair results can be seen when examining longer inter-ionization distances as seen in Figure 11. In this figure, 1 MeV, 56 keV, 3 keV, 100 eV, 200 eV and 500 eV monoenergetic electron profiles have been displayed. Note that these figures have been normalized such that the integral is equal to the average number of ionizations in the electron track.

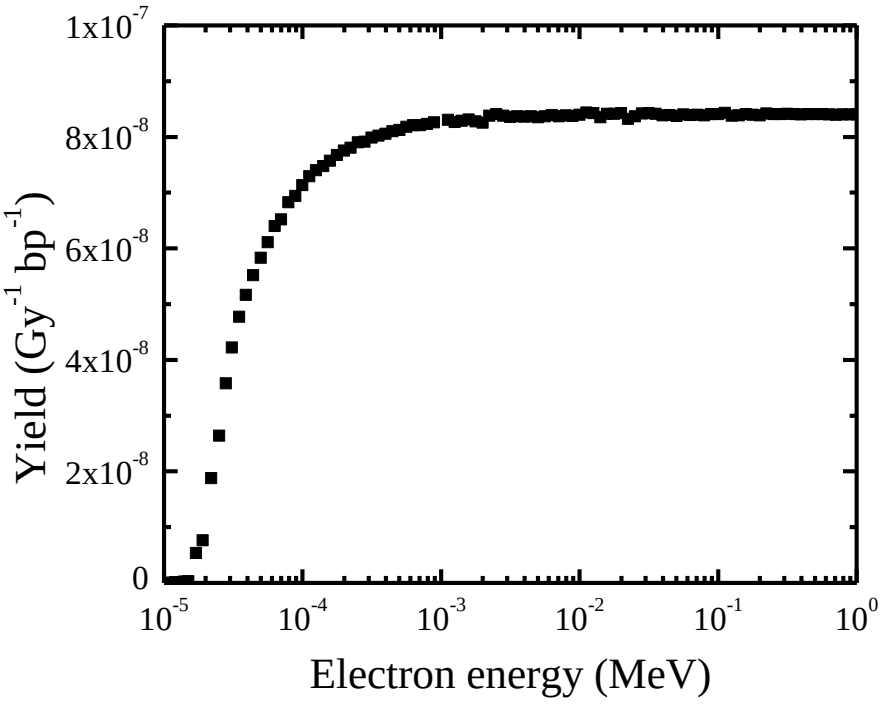

Figure 9 Yield of SSBs as a function of electron energy.

The yield of double strand DNA breaks as a function of monoenergetic electron energy has been shown in Figure 12. DSB yield is displayed on the y-axis in units of DSB per gray per base pair and initial electron energy is displayed on the x axis in units of MeV. At 1 MeV the DSB break yield has been predicted to be 4.1E-9 and it rises to a peak value of 2.2E-8 at 600 eV.

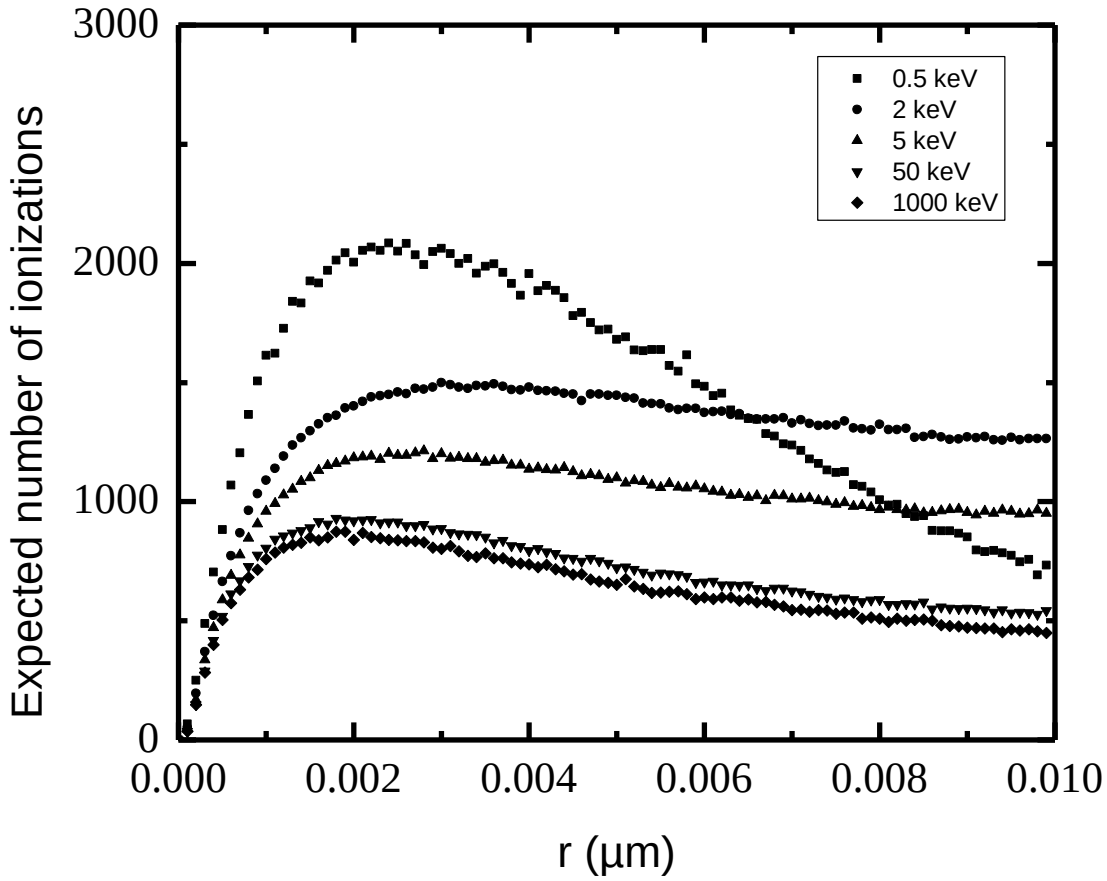

Figure 10 - Expected number of ionization pairs formed in an electron track as a function of separation distance for several initial electron energies.

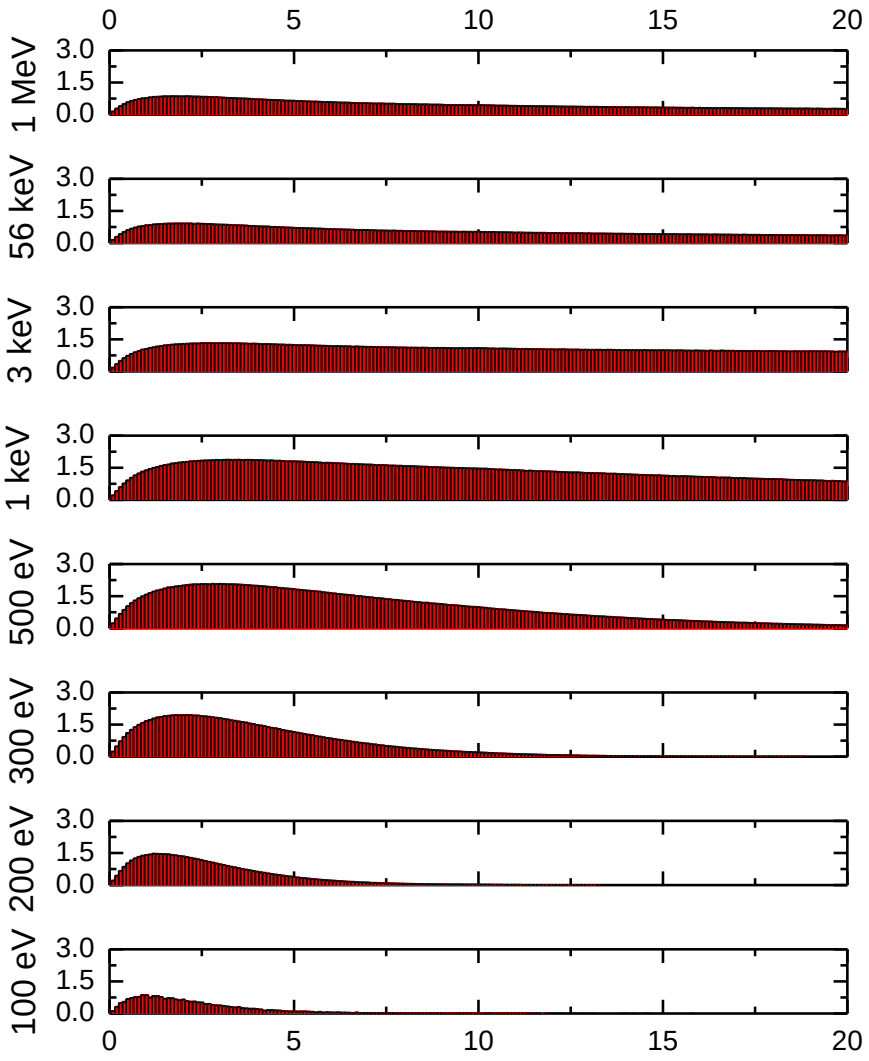

Figure 11 - Profiles of the frequency of particular inter-ionization distances. Several energies are shown with distance in nm on the x-axis. The y-axis shows frequency of ionization pairs per electron track.

The RBE of electrons as a function of energy has been shown in Figure 13. Shown on the x axis of this figure is the initial energy of the electrons. While the

electrons slow down and eventually come to rest, it is important to note that RBE shown here is for the initial energy only. The RBE of the electrons is shown on the y axis. Here, 1 MeV electrons are the reference radiation under a DSB yield endpoint. The solid line reflects values calculated in this thesis while data from Nikjoo (2010) have been included as + symbols for comparison.

For most electron energies, the RBE values in this work are slightly higher than those predicted by Nikjoo (2010) although there is general agreement. Both models predict that the RBE of electrons is near to 1 for energies above 100 keV. Both models also predict that there is a sharp rise in RBE for electron energies near to 1 keV. The data from this thesis covers a greater energy range than Nikjoo 2010 and predicts that RBE drops to zero for electrons with energies around 7 eV.

These monoenergetic electron RBE data have been used to construct RBE estimates for photons, x-rays and radionuclide spectra which have been shown later in this section. Tabulated RBE values have been included in Appendix B.

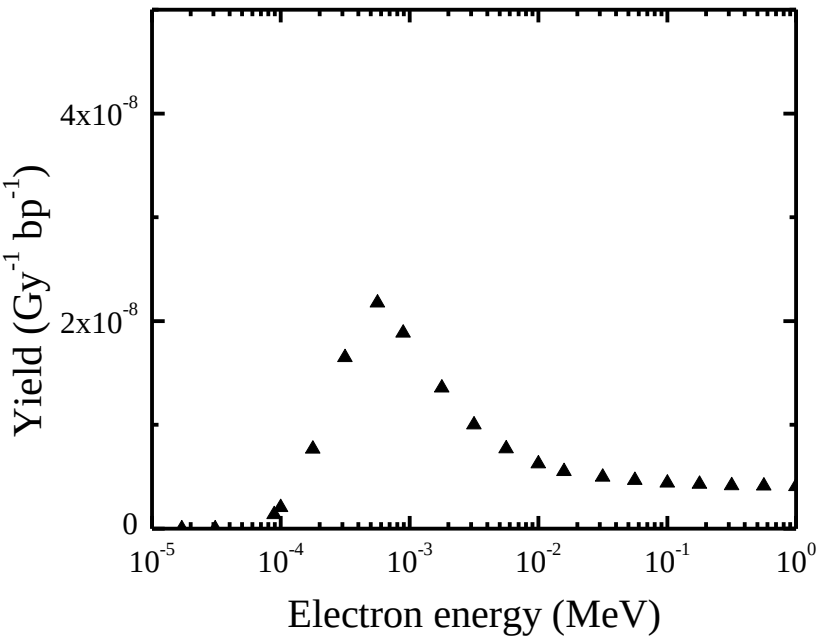

Figure 12 Yield of DSBs as a function of electron energy.

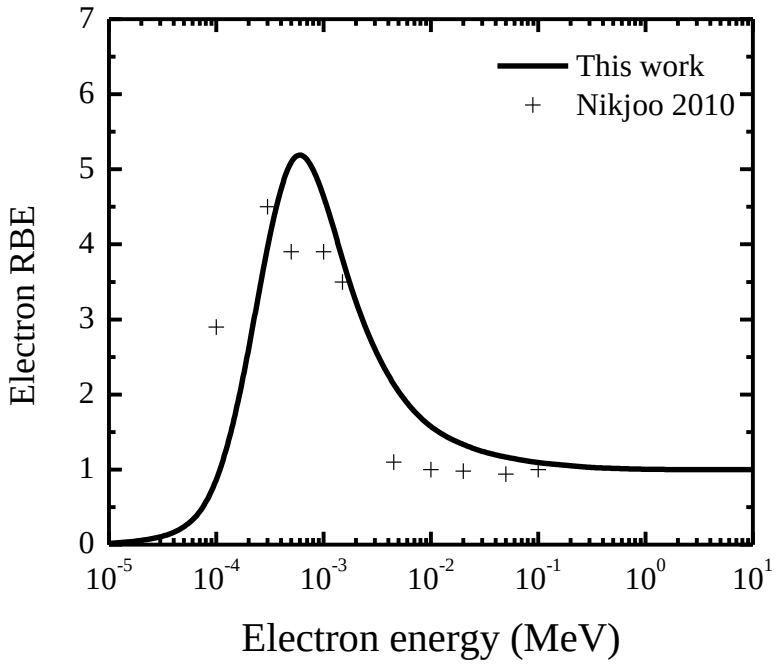

Figure 13 - RBE of monoenergetic electrons as a function of initial electron energy. Results of (Nikjoo, 2010) have been included for comparison.

The initial electron spectra of various monoenergetic photon sources have been shown in Figure 14. Electron energy has been shown on the x-axis in units of MeV and the maximum energy in each case corresponds to the energy of the incident photon. Energies shown in this figure include 1 MeV, 0.5 MeV, 0.2 MeV, 0.1 MeV, 0.05 MeV and 0.01 MeV photons. Photoelectric interactions become more likely for lower energy photons while Compton scattering dominates interactions originating from 1 MeV photons. Note the ability of photons near to 0.05 MeV to predominantly produce electrons of much lower energy than the incident photon. In this energy range, Compton scattering is the main interaction, but the photon momentum is sufficiently low to produce a Compton edge with only small fraction of the incident photon's energy.

The RBE of photons as a function of energy has been shown in Figure 15. Shown on the x axis of this figure is the initial energy of the electrons. To compute these values, the photon energy deposition was fully tracked through Compton scatters, pair production events and photoelectric ionizations so the RBE shown here relates to the initial energy of the photon only. Just as in electron RBE, 1 MeV electrons have been used as the reference radiation under a DSB yield endpoint. The solid line reflects values calculated in this thesis while experimental data summarized in Nikjoo (2010) have been included for comparison.

The photon RBE data were found to be an almost exact match to the electron RBE data. However, one notable difference is the local maximum in the photon data

around 100 keV. This feature arises primarily from the increased probability of these photons to produce high RBE electrons through Compton scattering and secondarily from the downshift of the Compton edge as the primary photon energy decreases. The initial electron spectrum of several monoenergetic photons interacting in water can be seen in Figure 14 on page 48. This feature is important because it is in the energy range of commonly used x-rays and thus lessens the predicted RBE difference between high and low tube voltage x-rays as seen in the next section.

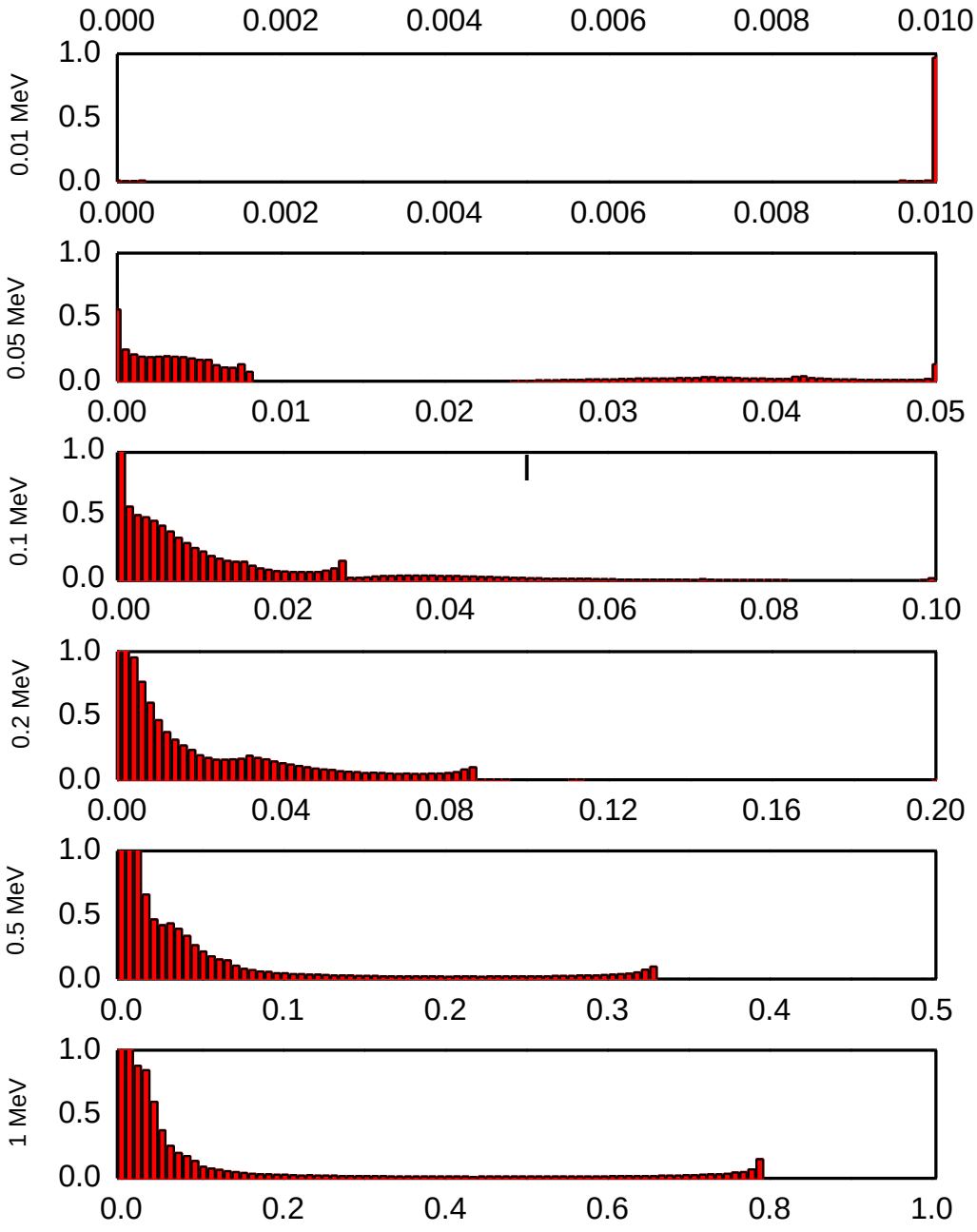

Figure 14 – Initial electron spectrum of several monoenergetic photons interacting in water. Photon energies from top to bottom: 1 MeV, 0.5 MeV, 0.2 MeV, 0.1 MeV, 0.05 MeV and 0.01 MeV.

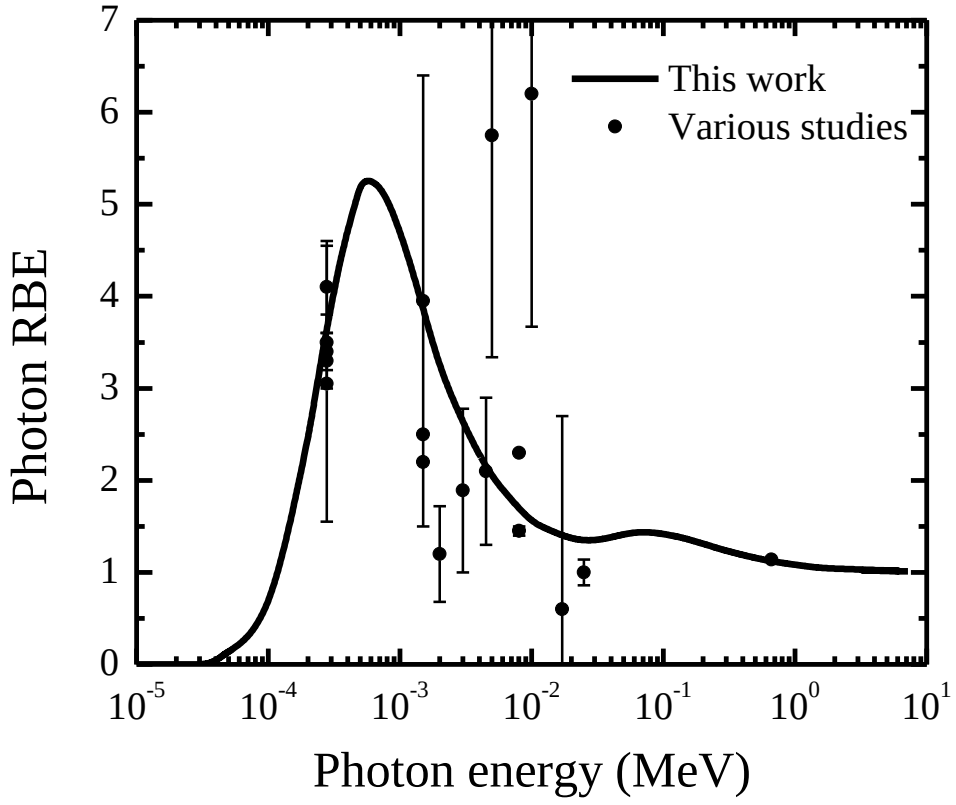

Figure 15 –RBE values of monoenergetic photons as a function of energy. Experimental data has been included for comparison (Nikjoo 2010).

RBE values for various x-ray spectra have been presented in Table 3. X-rays tube voltages of 20, 40, 80 and 120 have been used in this calculation. Both unfiltered and 1mm Cu filtered x-ray spectra have been included. Algorithms for generating x-ray spectra described in (Boone 1997, Boone 1998).

RBE values computed for radionuclides have been displayed in Figure 17 below on page 53. Values for over one thousand values have been summarized in this figure and a few of the highest RBE radionuclides along with tritium have been labeled. The decay mode

has also been included for all of these radionuclides. A complete listing of the radionuclide RBE calculation results have been tabulated in appendix A. The vast majority of the radionuclide emissions are close to one and a small fraction exceed two.

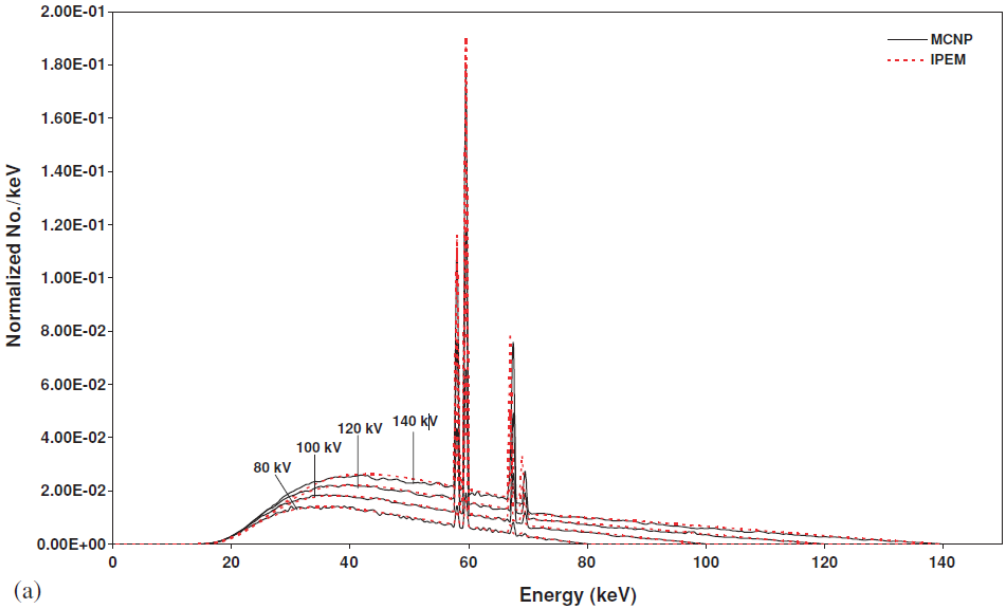

Figure 16 - A comparison between several MCNP simulated spectra and experimentally recorded spectra showing the accuracy and precision of current compter simulation of X-RAYs. (Ay, 2004) 0.1 mm Cu filters were present.

Table 3- x-ray RBE values predicted by the cumulative dose and the DSB yield methods. Filtered and unfiltered spectra of 20, 40, 80 and 120 kVP x-rays from a tungsten target.

x-ray source		
Voltage (kVP)	Filter	RBE
20	1mm Cu	1.35
40	1mm Cu	1.36
80	1mm Cu	1.41
120	1mm Cu	1.40
20	Unfiltered	1.53
40	Unfiltered	1.44
80	Unfiltered	1.38
120	Unfiltered	1.40

Egbert et al. (2007) have tabulated the photon fluence at Hiroshima and Nagasaki at several ground distances from the hypocenter. The tissue kerma-weighted mean energy of the photon spectrum is 3.2 and 3.3 MeV at Hiroshima and Nagasaki, respectively. The spectrum of secondary electrons liberated within the body at 1500 m ground distance was calculated using the MCNPX code (Pelowitz 2008), and the RBE for this spectrum was calculated. For both cities the resultant photon RBE was 1.0, the same as also is the RBE for Co-60 gamma rays. Thus, it appears the Co-60 gamma rays are no more effective than Hiroshima and Nagasaki photon fluence, in contrast to an earlier suggestion (by Straume (1995).

Because of the ongoing discussion about the nature of the biological target, DNA break complexity is an important consideration (Goodhead 2006). The cell, the nucleus and DNA are all candidates for this sensitive volume. Double strand breaks are the endpoint of choice in this dissertation but since simple double strand breaks are readily repaired, examining the ability of a radiation to induce clustered damage in the form of complex DNA breaks may be important in predicting the RBE of more complicated endpoints. In Figure 18 below, the fraction of simple double strand breaks, and two categories of complex double strand breaks have been presented for four electron energies. DSB+ denotes double strand breaks with one additional base or backbone damage site while DSB++ denotes double strand breaks with more than one additional damage site. For very low electron energies like 100 eV and for relatively high electron energies such as 1 MeV electrons, above 80% to 90% of the strand breaks are simple in nature.

The percentage of complex strand breaks is higher for 1 keV electrons, with greater than 40% of the breaks being either DSB+ or DSB++. If a DSB+ endpoint is chosen, the RBE vs. energy relationship can be seen below in Figure 19. The DSB+ endpoint predicts much higher RBE values than the simple double strand break endpoint with maximum RBE values approaching 15.

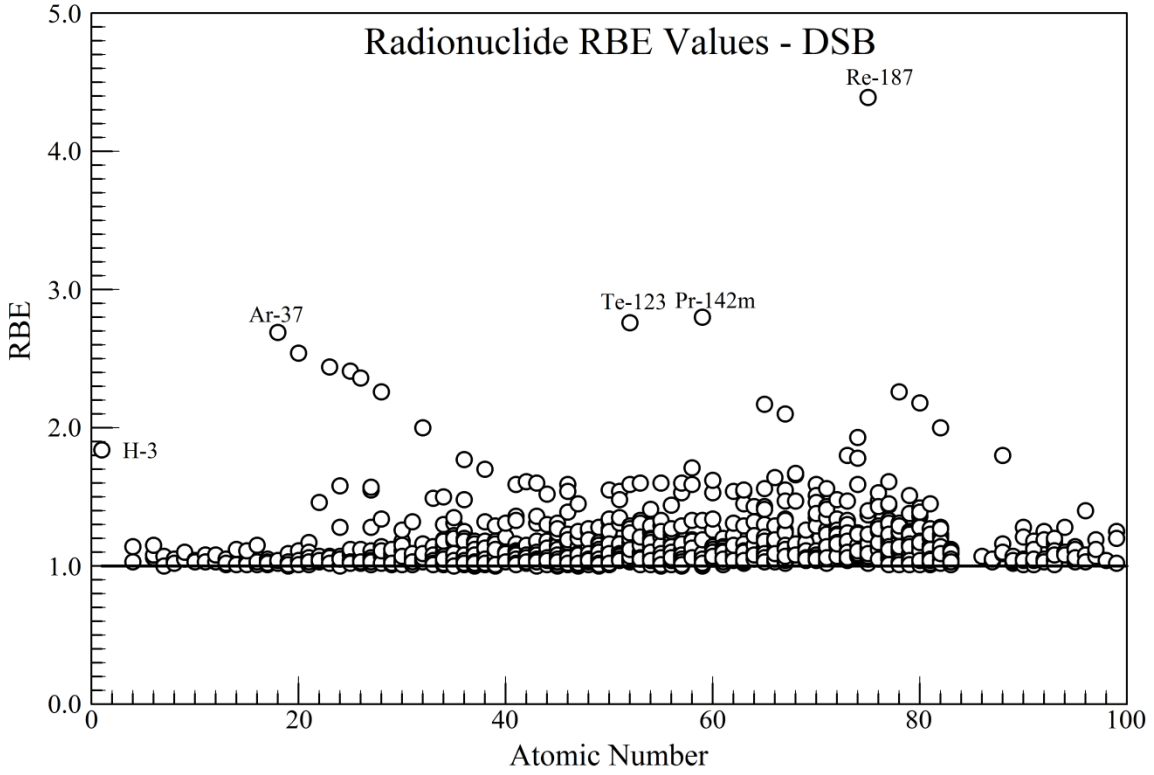

Figure 17- Calculated RBE values from the photon and beta emission spectra of radionuclides. The radionuclides in this figure have been ordered by atomic number on the x-axis and RBE values are represented on the y-axis.

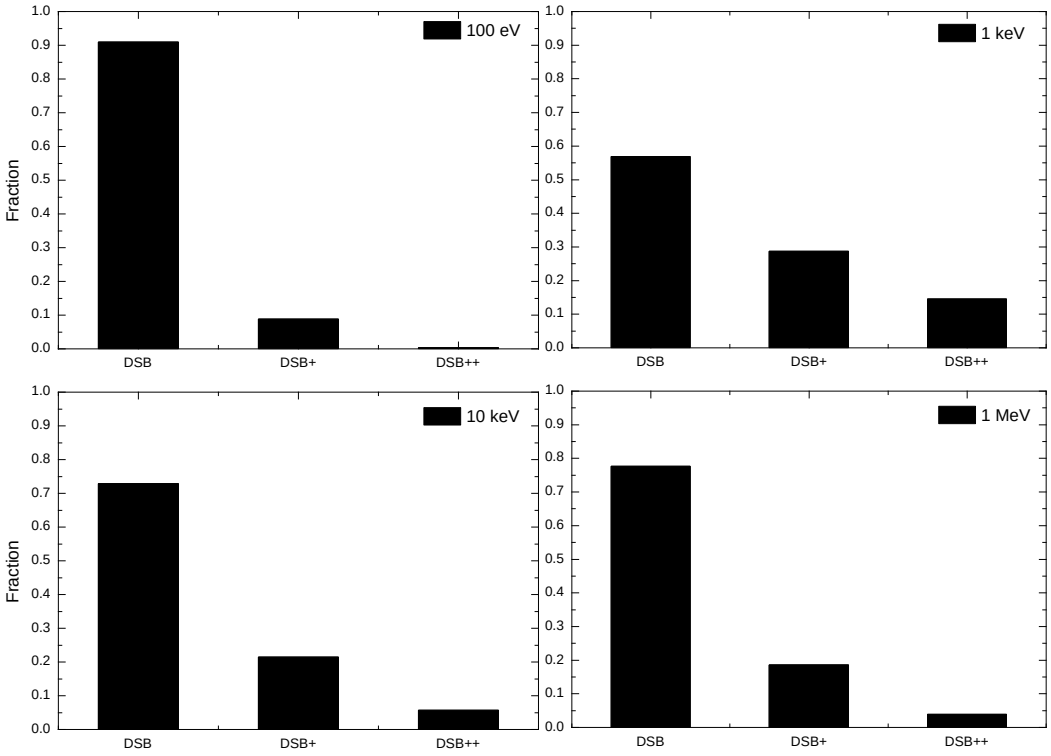

Figure 18 - Break complexity of double strand DNA breaks for four energies. In this figure, 'DSB' represents double strand breaks with no additional damage, DSB+ represents double strand breaks with one additional damage site and DSB++ represents double strand breaks with more than one additional break.

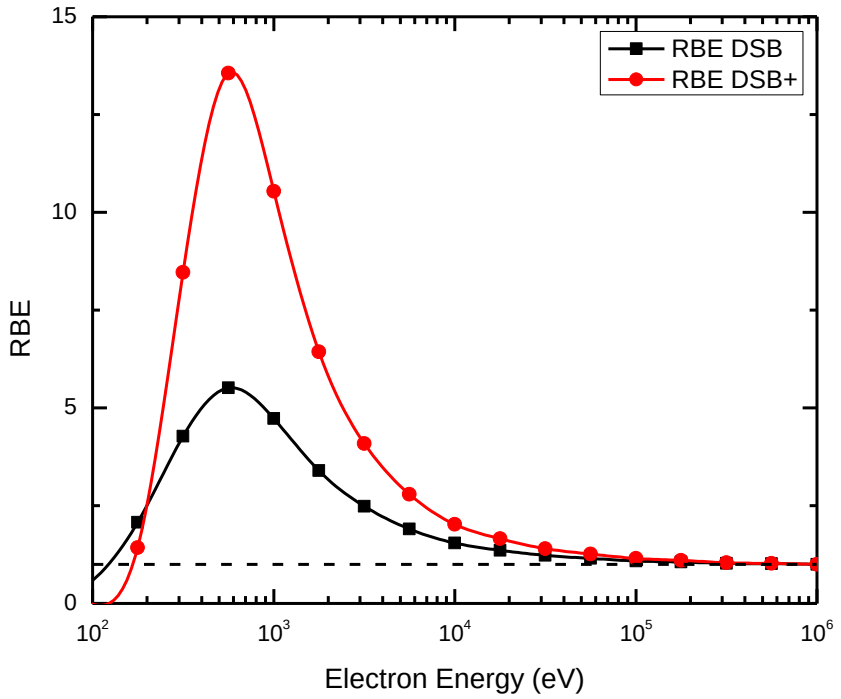

Figure 19 - The relationship between electron energy and DSB break complexity. RBE values are displayed on the y-axis while initial electron energy is displayed on the x-axis. In this figure, DSB+ denotes double strand breaks with one or more additional damage sites. The dashed horizontal line in this figure represents an RBE of one.

CHAPTER 6

DISCUSSION

In this section, the RBE values of electrons and photons are discussed first. Next, a possible explanation of the underlying cause of the energy dependence is offered. After this, SSB to DSB values, C_k RBE values and monoenergetic electron RBE values from published results are compared with the predictions in this work. Next, the validity of RBE values in this work is discussed. Finally, the significance of the results in this thesis is addressed.

The RBE of electrons and photons has been found to vary with radiation energy. In general, RBE values increase with decreasing energy. However, as radiation energies approach the ionization threshold of 7.4 eV, the RBE quickly decreases to zero. The maximum RBE value for both electrons and photons was found to be around 5 as shown in Figure 13 and in Figure 15. These RBE values have been applied to x-rays and radionuclides and the results are shown in Table 3 and appendix A.

The electron RBE values predicted in this work show similar characteristics to those published in Nikjoo (2010). In both sets of results, the RBE of monoenergetic electrons is close to 1 for electron energies between 100 and 1000 keV. Also, both sets of results predict a maximum RBE value around 5. One notable difference between

predictions is in the 5keV to 100keV energy range, where the RBE values predicted in this work are higher than those predicted by Nikjoo.

The likely cause of the energy dependent nature of RBE is the variation in ionization density for different electron tracks. This variation is related to the ability of a radiation to cause clustered DNA damage which in turn leads to double strand DNA breaks. Low energy electrons have been shown to produce a greater yield of ionization pairs of DNA dimension and so produce complex strand breaks more often than electrons with energies comparable to 1 MeV. Photons and x-rays primarily deposit their energy through electrons thus by the same argument, the energy dependent nature is also reflected in these radiations.

Various quantities predicted in work agree with published results. Siddiqi and Bothe (1987) published SSB to DSB ratios ranging between 13 and 25 and the ratios predicted in this work fall within this range. RBE values published by Goodhead *et al (*1979), Thacker *et al* (1986), Raju *et al* (1987) and Folkard *et al* for C_k are also in agreement with values predicted in this work. Also, monoenergetic electron RBE values published by Nikjoo (1994) from a different method are similar to those predicted in this work as seen in Figure 13. It should be noted that this work predicts the RBE of all electrons from zero to 1 MeV and it is difficult to find another paper which makes predictions over a similar range.

According to Goodhead (2006) in his invited paper, "Energy Deposition Stochastics and track structure: What about the target?" a high proportion of DSB formed from low-LET radiation are complex. Specifically, the proportion of complex DSB rises from 20% to around 30% and the majority additional damage is found within 10 base

pairs from the DSB lesion. The same quantity has been calculated and shown in Figure 18, the proportion of complex DSB calculated in this thesis rises from 20% to around 40% across the same energy range. Because of the similarity of these ranges, one can claim general agreement between Goodhead's published values and values calculated in this work although it should be noted that this work predicts slightly greater break complexity.

In this work, the electron track was characterized individually under the assumption that track overlap can be ignored. There are two special cases where this assumption is invalid and thus the calculated RBE values may be under-predictions. The first case is in high dose scenarios. In this scenario, so many electrons will be deposited in the tissue that the probability of track overlap will become significant. This would be in the quadratic region of a linear-quadratic dose-response curve. However, even under very high medical therapy doses, the probability of track overlap is small enough for track overlap to be ignored (Goodhead 2006). In addition, the track overlap assumption also breaks down when considering Auger beta-emitting radionuclides. These radionuclides emit several electrons from the same starting physical location so track independence cannot be assumed. Therefore predictions made in this work would likely under-predict the actual RBE of these sources. The methods employed in this work can potentially be refined to account for this phenomenon but this endeavor is outside the thesis scope. Nevertheless, Auger electron RBE values have been included in Appendix as a reference. The difficulty of computing Auger emitter RBE is a known issue and is outside the scope of this work.

Another assumption in this work is that electrons are completely absorbed in tissue. This means that they start and deposit all their energy within the tissue volume. Because of the short range of charged particles in tissue, most electrons will fall under this criterion. However, very high energy electrons such as those around greater than 50 MeV may escape a tissue volume which are around the size of a human and only partially deposit their energy within the tissue volume. Since the beginning of these electron tracks are typically low density, very high energy electron RBE may be lower than that of the reference radiation.

As photon energies decrease, the maximum fraction of photon energy available to Compton scattered electrons is also reduced. This leads to an unexpected phenomenon where some photons may on average produce a softer electron spectrum than lower energy photons. This phenomenon is illustrated in the top two tiles above in Figure 14 where a 0.05 MeV photon produces a softer spectrum than a 0.01 MeV photon. Although subtle, this effect has consequences to x-ray RBE because RBE does not monotonically increase with decreasing photon energy.

The results presented in this thesis could provide a basis for improved risk estimates. According to the ICRP, nuclide specific RBE values are valuable when recreating dose values in specific cases of irradiation. While experimental RBE values would be most applicable to those scenarios, they are not always available. In such a case, values presented here could be used if no superior alternative is available.

CHAPTER 7

CONCLUSION

Experimental, computational and epidemiological studies imply that there is a rise in biological effectiveness with decreasing energy of electron and photon radiations. The exact extent and shape of the increased RBE as a function of energy is difficult to obtain from epidemiological studies and cell experiments. A newly developed theoretical approach was found to yield results which are generally consistent with the experimental observations. RBE values for monoenergetic electrons, photons and selected isotopes have been calculated and reported.

The methods employed in this thesis predict an increased RBE with decreasing electron and photon energy. The DSB yield method predicts that electron RBE values remains near one for electrons above 100keV but increases to as much as 5.5 at lower energies (Figure 13).

Investigating RBE for a DSB+ endpoint reveals that the RBE may be up to three times larger than for a DSB endpoint (Figure 19). This may be relevant as complex strand breakage may play an important role in mutagenesis and oncogenesis. It is however, difficult to validate this result due to lack of experimental data for these endpoints.

The predicted RBE values for tritium and carbon-14 are 2.0 and 1.3 respectively; these two common low energy beta emitters are widely distributed in the tissues of the body. Machine generated 20 kVP x-rays have a higher RBE than 120 kVP x-rays and for the tube voltages examined in this work, the hardening of the beam achieved with a 1 mm Cu filter reduces the RBE (Table 3). The RBE values of over 1000 radionuclides have been estimated (Figure 17). An extensive list of radionuclides along with their corresponding RBE values is included in Appendix A.

CHAPTER 8

FUTURE WORK

Because of the novel nature of this approach there are several areas in which future research efforts can be directed. In this section, some of these areas will be identified and briefly discussed.

A natural extension of this work would be in the estimation of high-LET RBE values. There is ample experimental data quantifying radio-biological interactions of alphas, protons and other heavy ions and the approach described in this work should be valid for modeling those particles. The approach would be identical but a new transport could would be needed (such as geant4-DNA) as NOREC is incapable of transporting these particles. While presenting this thesis research at various conferences, this area of future work was consistently suggested.

Another potential area of future work would be in the analysis of uncertainties. There are uncertainties introduced at every step of this RBE derivation; so much so that efforts in this field often seem to be as much art as science. Potential sources include cross-section uncertainties in the electron code, uncertainties in the newly developed 30-nm solenoidal DNA model, uncertainties in the inter-ionization distance profile, uncertainties in the diffusion lengths, uncertainties resulting from the use of the Binomial distribution just to name a few. Completely quantifying these uncertainties would be

either impossible or at the very least prohibitively time consuming due to our lack of knowledge in critical areas. Presenting computational model results without uncertainty analyses is typical in the field of microdosimetry but this is certainly a potential avenue for future work.

Another potential area of investigation would be to test the assumption that electron RBE remains constant at energies over 1 MeV. This was impossible with the current code, but there are other codes (Nikjoo 2006) which have the ability to transport higher energy electrons. Using another electron code to extend the energy range also has the added benefit of validating the existing results from NOREC.

Inclusion of quantum resonance strand breakage into this model (Boudaïffa 2000) would be another avenue of future work. Including this break mechanism into the model would be possible straightforward once although it would substantially complicate the mathematical RBE model. It is unlikely to significantly impact the RBE results as the number of ionizations per unit dose is relatively constant over the entire energy range.

A more thorough investigation of Auger emitting radionuclide RBE could be another future direction of this work. It is likely that a new way of quantifying the electron tracks will be necessary due to the highly correlated spatial ionization pattern of this form of radiation. If this Auger model is developed, quantifying and estimating the overkill effect would be an important part of the effort.

This is by no means an exhaustive list of future topics which could build upon this work. This approach could be used to compare and validate several parameters from modeling and experimental works. As a single example, it would be interesting to fully

compare the predictions of breakage complexity predicted from this model to those predicted by the spatial overlay model popularized by Turner, Freidland and Nijkoo.

APPENDIX A

RADIONUCLIDE RBE VALUES

*Ordered by Z

Radionuclide	Decay Mode	Halflife	Gy/Bq s	Sv / Bq s	RBE
H-3	B-	12.32y	1.31E-17	2.41E-17	1.838
Be-7	EC	53.22d	4.03E-17	4.60E-17	1.144
Be-10	B-	1.51E+6y	5.82E-16	6.02E-16	1.033
C-10	ECB+	19.255s	3.27E-15	3.45E-15	1.057
C-11	ECB+	20.39m	1.71E-15	1.85E-15	1.079
C-14	B-	5.70E+3y	1.14E-16	1.31E-16	1.152
N-13	ECB+	9.965m	1.96E-15	2.09E-15	1.068
N-16	B-	7.13s	8.61E-15	8.64E-15	1.003
O-14	ECB+	70.606s	4.14E-15	4.31E-15	1.042
O-15	ECB+	122.24s	2.52E-15	2.65E-15	1.051
O-19	B-	26.464s	4.76E-15	4.84E-15	1.016
F-17	ECB+	64.49s	2.53E-15	2.66E-15	1.051
F-18	ECB+	109.77m	1.36E-15	1.49E-15	1.096

Radionuclide	Decay Mode	Halflife	Gy/Bq s	Sv / Bq s	RBE
Ne-19	ECB+	17.22s	3.04E-15	3.17E-15	1.041
Ne-24	B-	3.38m	2.29E-15	2.37E-15	1.032
Na-22	ECB+	2.6019y	2.15E-15	2.32E-15	1.081
Na-24	B-	14.9590h	4.03E-15	4.15E-15	1.029
Mg-27	B-	9.458m	2.32E-15	2.39E-15	1.032
Mg-28	B-	20.915h	1.43E-15	1.54E-15	1.079
Al-26	ECB+	7.17E+5y	2.99E-15	3.15E-15	1.054
Al-28	B-	2.2414m	4.11E-15	4.17E-15	1.014
Al-29	B-	6.56m	3.27E-15	3.33E-15	1.019
Si-31	B-	157.3m	1.37E-15	1.39E-15	1.012
Si-32	B-	132y	1.58E-16	1.77E-16	1.117
P-30	ECB+	2.498m	4.14E-15	4.26E-15	1.029
P-32	B-	14.263d	1.60E-15	1.62E-15	1.009
P-33	B-	25.34d	1.76E-16	1.95E-16	1.108
S-35	B-	87.51d	1.12E-16	1.30E-16	1.153
S-37	B-	5.05m	3.64E-15	3.69E-15	1.014
S-38	B-	170.3m	2.30E-15	2.36E-15	1.026
Cl-34	ECB+	1.5264s	5.57E-15	5.68E-15	1.021
Cl-34m	ECB+IT	32.00m	2.55E-15	2.67E-15	1.047
Cl-36	B-ECB+	3.01E+5y	6.30E-16	6.50E-16	1.031
Cl-38	B-	37.24m	4.57E-15	4.62E-15	1.01
Cl-39	B-	55.6m	2.98E-15	3.07E-15	1.029

Radionuclide	Decay Mode	Halflife	Gy/Bq s	Sv / Bq s	RBE
Cl-40	B-	1.35m	6.19E-15	6.29E-15	1.016
Ar-37	EC	35.04d	5.88E-18	1.58E-17	2.693
Ar-39	B-	269y	5.05E-16	5.24E-16	1.039
Ar-41	B-	109.61m	2.03E-15	2.10E-15	1.036
Ar-42	B-	32.9y	5.37E-16	5.57E-16	1.036
Ar-43	B-	5.37m	4.25E-15	4.32E-15	1.017
Ar-44	B-	11.87m	2.60E-15	2.70E-15	1.041
K-38	ECB+	7.636m	5.07E-15	5.24E-15	1.033
K-40	B-ECB+	1.251E+9y	1.32E-15	1.34E-15	1.016
K-42	B-	12.360h	3.51E-15	3.53E-15	1.004
K-43	B-	22.3h	1.49E-15	1.62E-15	1.088
K-44	B-	22.13m	5.02E-15	5.11E-15	1.017
K-45	B-	17.3m	3.60E-15	3.69E-15	1.026
K-46	B-	105s	7.27E-15	7.34E-15	1.011
Ca-41	EC	1.02E+5y	7.46E-18	1.89E-17	2.539
Ca-45	B-	162.67d	1.78E-16	1.97E-16	1.107
Ca-47	B-	4.536d	1.60E-15	1.67E-15	1.041
Ca-49	B-	8.718m	3.93E-15	3.98E-15	1.013
Sc-42m	ECB+	62.0s	6.10E-15	6.38E-15	1.046
Sc-43	ECB+	3.891h	1.76E-15	1.89E-15	1.075
Sc-44	ECB+	3.97h	3.05E-15	3.22E-15	1.059
Sc-44m	ITEC	58.61h	2.92E-16	3.43E-16	1.171

Radionuclide	Decay Mode	Halflife	Gy/Bq s	Sv / Bq s	RBE
Sc-46	B-	83.79d	1.81E-15	1.95E-15	1.075
Sc-47	B-	3.3492d	4.61E-16	5.10E-16	1.105
Sc-48	B-	43.67h	3.07E-15	3.26E-15	1.063
Sc-49	B-	57.2m	1.89E-15	1.90E-15	1.006
Sc-50	B-	102.5s	6.17E-15	6.33E-15	1.026
Ti-44	EC	60.0y	1.50E-16	2.18E-16	1.458
Ti-45	ECB+	184.8m	1.56E-15	1.68E-15	1.075
Ti-51	B-	5.76m	2.30E-15	2.36E-15	1.028
Ti-52	B-	1.7m	1.84E-15	1.91E-15	1.037
V-47	ECB+	32.6m	2.65E-15	2.78E-15	1.046
V-48	ECB+	15.9735d	2.59E-15	2.78E-15	1.074
V-49	EC	330d	1.03E-17	2.51E-17	2.445
V-50	ECB-	1.50E+17y	1.08E-15	1.14E-15	1.062
V-52	B-	3.743m	3.53E-15	3.59E-15	1.017
V-53	B-	1.61m	3.12E-15	3.18E-15	1.021
Cr-48	ECB+	21.56h	3.69E-16	4.72E-16	1.281
Cr-49	ECB+	42.3m	2.25E-15	2.40E-15	1.07
Cr-51	EC	27.7025d	3.68E-17	5.80E-17	1.578
Cr-55	B-	3.497m	2.54E-15	2.55E-15	1.003
Cr-56	B-	5.94m	1.49E-15	1.56E-15	1.048
Mn-50m	ECB+	1.75m	7.09E-15	7.39E-15	1.043
Mn-51	ECB+	46.2m	2.96E-15	3.08E-15	1.041

Radionuclide	Decay Mode	Halflife	Gy/Bq s	Sv / Bq s	RBE
Mn-52	ECB+	5.591d	2.82E-15	3.04E-15	1.078
Mn-52m	ECB+IT	21.1m	4.45E-15	4.62E-15	1.038
Mn-53	EC	3.7E+6y	1.23E-17	2.97E-17	2.408
Mn-54	ECB+B-	312.12d	6.71E-16	7.49E-16	1.116
Mn-56	B-	2.5789h	3.16E-15	3.25E-15	1.03
Mn-57	B-	85.4s	2.62E-15	2.67E-15	1.019
Mn-58m	B-	65.2s	5.82E-15	5.95E-15	1.023
Fe-52	ECB+	8.275h	1.04E-15	1.17E-15	1.122
Fe-53	ECB+	8.51m	3.49E-15	3.63E-15	1.041
Fe-53m	IT	2.526m	2.32E-15	2.48E-15	1.071
Fe-55	EC	2.737y	1.35E-17	3.18E-17	2.362
Fe-59	B-	44.495d	1.17E-15	1.25E-15	1.066
Fe-60	B-	1.5E+6y	1.50E-16	1.68E-16	1.124
Fe-61	B-	5.98m	3.57E-15	3.65E-15	1.023
Fe-62	B-	68s	2.31E-15	2.38E-15	1.03
Co-54m	ECB+	1.48m	7.76E-15	8.04E-15	1.036
Co-55	ECB+	17.53h	2.56E-15	2.74E-15	1.069
Co-56	ECB+	77.23d	2.90E-15	3.08E-15	1.061
Co-57	EC	271.74d	1.50E-16	2.32E-16	1.548
Co-58	ECB+	70.86d	8.53E-16	9.50E-16	1.114
Co-58m	IT	9.04h	5.74E-17	9.04E-17	1.574
Co-60	B-	5.2713y	2.11E-15	2.23E-15	1.061

Radionuclide	Decay Mode	Halflife	Gy/Bq s	Sv / Bq s	RBE
Co-60m	ITB-	10.467m	1.39E-16	1.77E-16	1.276
Co-61	B-	1.650h	1.16E-15	1.21E-15	1.042
Co-62	B-	1.50m	4.94E-15	5.00E-15	1.013
Co-62m	B-	13.91m	4.52E-15	4.64E-15	1.026
Ni-56	ECB+	6.075d	1.37E-15	1.56E-15	1.137
Ni-57	ECB+	35.60h	1.82E-15	1.94E-15	1.071
Ni-59	ECB+	1.01E+5y	1.59E-17	3.60E-17	2.26
Ni-63	B-	100.1y	4.02E-17	5.37E-17	1.337
Ni-65	B-	2.51719h	1.86E-15	1.90E-15	1.021
Ni-66	B-	54.6h	1.69E-16	1.88E-16	1.111
Cu-57	ECB+	0.1963s	9.21E-15	9.33E-15	1.013
Cu-59	ECB+	81.5s	4.58E-15	4.73E-15	1.032
Cu-60	ECB+	23.7m	4.95E-15	5.18E-15	1.045
Cu-61	ECB+	3.333h	1.38E-15	1.49E-15	1.08
Cu-62	ECB+	9.673m	3.77E-15	3.89E-15	1.031
Cu-64	ECB+B-	12.700h	4.39E-16	4.79E-16	1.092
Cu-66	B-	5.120m	2.54E-15	2.55E-15	1.006
Cu-67	B-	61.83h	4.39E-16	4.94E-16	1.125
Cu-69	B-	2.85m	2.45E-15	2.50E-15	1.018
Zn-60	ECB+	2.38m	3.84E-15	4.02E-15	1.047
Zn-61	ECB+	89.1s	5.47E-15	5.61E-15	1.026
Zn-62	ECB+	9.186h	4.42E-16	5.21E-16	1.179

Radionuclide	Decay Mode	Halflife	Gy/Bq s	Sv / Bq s	RBE
Zn-63	ECB+	38.47m	3.00E-15	3.13E-15	1.042
Zn-65	ECB+	244.06d	4.66E-16	5.18E-16	1.11
Zn-69	B-	56.4m	7.42E-16	7.62E-16	1.028
Zn-69m	ITB-	13.76h	3.88E-16	4.45E-16	1.147
Zn-71	B-	2.45m	2.67E-15	2.71E-15	1.014
Zn-71m	B-	3.96h	2.50E-15	2.69E-15	1.074
Zn-72	B-	46.5h	3.65E-16	4.59E-16	1.258
Ga-64	ECB+	2.627m	6.36E-15	6.55E-15	1.03
Ga-65	ECB+	15.2m	2.82E-15	2.99E-15	1.06
Ga-66	ECB+	9.49h	3.94E-15	4.06E-15	1.031
Ga-67	EC	3.2612d	2.18E-16	2.89E-16	1.321
Ga-68	ECB+	67.71m	2.47E-15	2.58E-15	1.047
Ga-70	B-EC	21.14m	1.49E-15	1.51E-15	1.011
Ga-72	B-	14.10h	3.13E-15	3.27E-15	1.045
Ga-73	B-	4.86h	1.44E-15	1.57E-15	1.091
Ga-74	B-	8.12m	4.53E-15	4.67E-15	1.031
Ge-66	ECB+	2.26h	7.82E-16	9.06E-16	1.16
Ge-67	ECB+	18.9m	3.82E-15	3.99E-15	1.044
Ge-68	EC	270.95d	2.09E-17	4.18E-17	1.999
Ge-69	ECB+	39.05h	1.02E-15	1.11E-15	1.087
Ge-71	EC	11.43d	2.12E-17	4.23E-17	1.996
Ge-75	B-	82.78m	9.98E-16	1.03E-15	1.027

Radionuclide	Decay Mode	Halflife	Gy/Bq s	Sv / Bq s	RBE
Ge-77	B-	11.30h	2.34E-15	2.48E-15	1.059
Ge-78	B-	88m	7.45E-16	8.16E-16	1.095
As-68	ECB+	151.6s	7.42E-15	7.67E-15	1.033
As-69	ECB+	15.23m	3.72E-15	3.85E-15	1.035
As-70	ECB+	52.6m	5.27E-15	5.56E-15	1.054
As-71	ECB+	65.28h	7.34E-16	8.40E-16	1.143
As-72	ECB+	26.0h	3.81E-15	3.98E-15	1.044
As-73	EC	80.30d	1.70E-16	2.52E-16	1.485
As-74	ECB+B-	17.77d	1.23E-15	1.32E-15	1.079
As-76	B-	1.0778d	2.79E-15	2.83E-15	1.016
As-77	B-	38.83h	5.28E-16	5.49E-16	1.04
As-78	B-	90.7m	3.86E-15	3.95E-15	1.023
As-79	B-	9.01m	2.05E-15	2.07E-15	1.007
Se-70	ECB+	41.1m	1.15E-15	1.31E-15	1.138
Se-71	ECB+	4.74m	4.46E-15	4.63E-15	1.037
Se-72	EC	8.40d	1.00E-16	1.50E-16	1.497
Se-73	ECB+	7.15h	1.78E-15	1.96E-15	1.098
Se-73m	ITECB+	39.8m	5.93E-16	6.47E-16	1.09
Se-75	EC	119.779d	3.52E-16	4.58E-16	1.303
Se-77m	IT	17.36s	2.44E-16	2.88E-16	1.178
Se-79	B-	2.95E+5y	1.22E-16	1.40E-16	1.145
Se-79m	ITB-	3.92m	2.07E-16	2.46E-16	1.188

Radionuclide	Decay Mode	Halflife	Gy/Bq s	Sv / Bq s	RBE
Se-81	B-	18.45m	1.42E-15	1.43E-15	1.012
Se-81m	ITB-	57.28m	2.23E-16	2.63E-16	1.18
Se-83	B-	22.3m	3.03E-15	3.23E-15	1.067
Se-83m	B-	70.1s	3.64E-15	3.70E-15	1.017
Se-84	B-	3.1m	1.61E-15	1.68E-15	1.047
Br-72	ECB+	78.6s	8.72E-15	8.94E-15	1.026
Br-73	ECB+	3.4m	4.25E-15	4.42E-15	1.04
Br-74	ECB+	25.4m	5.59E-15	5.81E-15	1.04
Br-74m	ECB+	46m	5.96E-15	6.21E-15	1.043
Br-75	ECB+	96.7m	2.18E-15	2.35E-15	1.077
Br-76	ECB+	16.2h	3.54E-15	3.72E-15	1.051
Br-76m	ITECB+	1.31s	2.16E-16	2.83E-16	1.31
Br-77	ECB+	57.036h	2.87E-16	3.51E-16	1.22
Br-77m	IT	4.28m	2.25E-16	2.65E-16	1.176
Br-78	ECB+B-	6.46m	3.20E-15	3.32E-15	1.038
Br-80	B-ECB+	17.68m	1.73E-15	1.75E-15	1.012
Br-80m	IT	4.4205h	1.84E-16	2.49E-16	1.355
Br-82	B-	35.30h	2.40E-15	2.61E-15	1.087
Br-82m	ITB-	6.13m	1.77E-16	2.11E-16	1.197
Br-83	B-	2.40h	7.57E-16	7.79E-16	1.028
Br-84	B-	31.80m	4.05E-15	4.12E-15	1.017
Br-84m	B-	6.0m	4.18E-15	4.36E-15	1.043

Radionuclide	Decay Mode	Halflife	Gy/Bq s	Sv / Bq s	RBE
Br-85	B-	2.90m	2.45E-15	2.46E-15	1.005
Kr-74	ECB+	11.50m	2.24E-15	2.42E-15	1.078
Kr-75	ECB+	4.29m	4.59E-15	4.76E-15	1.037
Kr-76	EC	14.8h	3.92E-16	4.89E-16	1.249
Kr-77	ECB+	74.4m	2.40E-15	2.56E-15	1.068
Kr-79	ECB+	35.04h	2.68E-16	3.20E-16	1.197
Kr-81	EC	2.29E+5y	2.71E-17	4.80E-17	1.77
Kr-81m	ITEC	13.10s	2.44E-16	2.89E-16	1.182
Kr-83m	IT	1.83h	9.58E-17	1.41E-16	1.477
Kr-85	B-	10.756y	5.80E-16	6.00E-16	1.035
Kr-85m	B-IT	4.480h	7.14E-16	7.72E-16	1.081
Kr-87	B-	76.3m	3.63E-15	3.68E-15	1.014
Kr-88	B-	2.84h	2.20E-15	2.29E-15	1.04
Kr-89	B-	3.15m	4.53E-15	4.63E-15	1.022
Rb-77	ECB+	3.77m	5.13E-15	5.31E-15	1.035
Rb-78	ECB+	17.66m	5.77E-15	5.98E-15	1.036
Rb-78m	ECB+IT	5.74m	5.90E-15	6.14E-15	1.041
Rb-79	ECB+	22.9m	3.03E-15	3.23E-15	1.065
Rb-80	ECB+	33.4s	5.68E-15	5.81E-15	1.023
Rb-81	ECB+	4.576h	6.98E-16	7.75E-16	1.11
Rb-81m	ITECB+	30.5m	2.21E-16	2.62E-16	1.184
Rb-82	ECB+	1.273m	4.15E-15	4.27E-15	1.03

Radionuclide	Decay Mode	Halflife	Gy/Bq s	Sv / Bq s	RBE
Rb-82m	ECB+	6.472h	2.51E-15	2.74E-15	1.094
Rb-83	EC	86.2d	4.27E-16	5.05E-16	1.184
Rb-84	ECB+B-	32.77d	1.10E-15	1.19E-15	1.084
Rb-84m	IT	20.26m	4.97E-16	5.77E-16	1.16
Rb-86	B-EC	18.642d	1.62E-15	1.64E-15	1.012
Rb-86m	IT	1.017m	4.64E-16	5.22E-16	1.125
Rb-87	B-	4.923E10y	2.66E-16	2.87E-16	1.078
Rb-88	B-	17.78m	5.23E-15	5.25E-15	1.005
Rb-89	B-	15.15m	3.83E-15	3.93E-15	1.027
Rb-90	B-	158s	5.98E-15	6.03E-15	1.009
Rb-90m	B-IT	258s	5.47E-15	5.59E-15	1.022
Sr-79	ECB+	2.25m	5.25E-15	5.41E-15	1.032
Sr-80	ECB+	106.3m	4.59E-16	5.29E-16	1.154
Sr-81	ECB+	22.3m	3.36E-15	3.54E-15	1.054
Sr-82	EC	25.36d	3.00E-17	5.09E-17	1.699
Sr-83	ECB+	32.41h	1.03E-15	1.15E-15	1.114
Sr-85	EC	64.84d	4.36E-16	5.12E-16	1.175
Sr-85m	ITECB+	67.63m	2.05E-16	2.71E-16	1.323
Sr-87m	ITEC	2.815h	4.14E-16	4.66E-16	1.126
Sr-89	B-	50.53d	1.35E-15	1.37E-15	1.012
Sr-90	B-	28.79y	4.52E-16	4.71E-16	1.043
Sr-91	B-	9.63h	2.06E-15	2.13E-15	1.031

Radionuclide	Decay Mode	Halflife	Gy/Bq s	Sv / Bq s	RBE
Sr-92	B-	2.66h	1.46E-15	1.53E-15	1.051
Sr-93	B-	7.423m	3.58E-15	3.75E-15	1.047
Sr-94	B-	75.3s	2.99E-15	3.05E-15	1.022
Y-81	ECB+	70.4s	5.49E-15	5.68E-15	1.034
Y-83	ECB+	7.08m	4.11E-15	4.28E-15	1.04
Y-83m	ECB+IT	2.85m	2.56E-15	2.69E-15	1.05
Y-84m	ECB+	39.5m	5.93E-15	6.23E-15	1.05
Y-85	ECB+	2.68h	2.00E-15	2.13E-15	1.066
Y-85m	ECB+	4.86h	2.35E-15	2.47E-15	1.051
Y-86	ECB+	14.74h	3.22E-15	3.45E-15	1.073
Y-86m	ITECB+	48m	2.31E-16	2.99E-16	1.294
Y-87	ECB+	79.8h	3.89E-16	4.60E-16	1.183
Y-87m	ITECB+	13.37h	4.32E-16	4.84E-16	1.119
Y-88	ECB+	106.65d	1.98E-15	2.10E-15	1.063
Y-89m	IT	15.663s	7.22E-16	7.80E-16	1.081
Y-90	B-	64.10h	2.15E-15	2.16E-15	1.005
Y-90m	ITB-	3.19h	6.20E-16	7.20E-16	1.162
Y-91	B-	58.51d	1.39E-15	1.41E-15	1.011
Y-91m	IT	49.71m	4.91E-16	5.49E-16	1.118
Y-92	B-	3.54h	3.54E-15	3.56E-15	1.006
Y-93	B-	10.18h	2.77E-15	2.79E-15	1.005
Y-94	B-	18.7m	4.77E-15	4.82E-15	1.01

Radionuclide	Decay Mode	Halflife	Gy/Bq s	Sv / Bq s	RBE
Y-95	B-	10.3m	4.05E-15	4.09E-15	1.01
Zr-85	ECB+	7.86m	4.23E-15	4.39E-15	1.038
Zr-86	ECB+	16.5h	3.35E-16	4.39E-16	1.31
Zr-87	ECB+	1.68h	2.64E-15	2.75E-15	1.041
Zr-88	EC	83.4d	3.65E-16	4.41E-16	1.209
Zr-89	ECB+	78.41h	1.16E-15	1.26E-15	1.092
Zr-89m	ITECB+	4.161m	5.79E-16	6.39E-16	1.103
Zr-93	B-	1.53E+6y	4.48E-17	5.88E-17	1.312
Zr-95	B-	64.032d	8.56E-16	9.34E-16	1.091
Zr-97	B-	16.744h	2.36E-15	2.44E-15	1.035
Nb-87	ECB+	3.75m	5.08E-15	5.28E-15	1.039
Nb-88	ECB+	14.5m	6.68E-15	7.05E-15	1.056
Nb-88m	ECB+	7.78m	6.55E-15	6.87E-15	1.048
Nb-89	ECB+	2.03h	3.54E-15	3.65E-15	1.031
Nb-89m	ECB+	66m	2.87E-15	3.02E-15	1.054
Nb-90	ECB+	14.60h	3.94E-15	4.17E-15	1.058
Nb-91	ECB+	680y	3.67E-17	5.83E-17	1.587
Nb-91m	ITECB+	60.86d	2.60E-16	3.02E-16	1.16
Nb-92	EC	3.47E+7y	1.22E-15	1.36E-15	1.112
Nb-92m	ECB+	10.15d	7.83E-16	8.63E-16	1.102
Nb-93m	IT	16.13y	7.22E-17	9.83E-17	1.361
Nb-94	B-	2.03E+4y	1.62E-15	1.76E-15	1.085

Radionuclide	Decay Mode	Halflife	Gy/Bq s	Sv / Bq s	RBE
Nb-94m	ITB-	6.263m	1.01E-16	1.35E-16	1.33
Nb-95	B-	34.991d	7.10E-16	7.85E-16	1.105
Nb-95m	ITB-	3.61d	4.80E-16	5.24E-16	1.092
Nb-96	B-	23.35h	2.52E-15	2.72E-15	1.081
Nb-97	B-	72.1m	1.61E-15	1.69E-15	1.049
Nb-98m	B-	51.3m	3.92E-15	4.12E-15	1.049
Nb-99	B-	15.0s	3.64E-15	3.72E-15	1.023
Nb-99m	B-IT	2.6m	3.79E-15	3.83E-15	1.011
Mo-89	ECB+	2.11m	5.50E-15	5.62E-15	1.023
Mo-90	ECB+	5.56h	1.16E-15	1.34E-15	1.147
Mo-91	ECB+	15.49m	4.14E-15	4.25E-15	1.027
Mo-91m	ECB+IT	64.6s	2.36E-15	2.47E-15	1.046
Mo-93	EC	4.0E+3y	3.56E-17	5.71E-17	1.606
Mo-93m	ITEC	6.85h	2.00E-15	2.16E-15	1.078
Mo-99	B-	65.94h	1.03E-15	1.06E-15	1.036
Mo-101	B-	14.61m	2.38E-15	2.53E-15	1.061
Mo-102	B-	11.3m	8.24E-16	8.49E-16	1.03
Tc-91	ECB+	3.14m	5.74E-15	5.90E-15	1.027
Tc-91m	ECB+	3.3m	5.49E-15	5.64E-15	1.027
Tc-92	ECB+	4.25m	7.08E-15	7.40E-15	1.045
Tc-93	ECB+	2.75h	1.28E-15	1.37E-15	1.069
Tc-93m	ITECB+	43.5m	8.99E-16	9.61E-16	1.069

Radionuclide	Decay Mode	Halflife	Gy/Bq s	Sv / Bq s	RBE
Tc-94	ECB+	293m	2.22E-15	2.45E-15	1.1
Tc-94m	ECB+	52.0m	3.25E-15	3.41E-15	1.049
Tc-95	EC	20.0h	6.62E-16	7.44E-16	1.123
Tc-95m	ECB+IT	61d	5.97E-16	6.96E-16	1.165
Tc-96	EC	4.28d	2.01E-15	2.21E-15	1.101
Tc-96m	ITECB+	51.5m	1.08E-16	1.41E-16	1.309
Tc-97	EC	2.6E+6y	3.65E-17	5.85E-17	1.601
Tc-97m	IT	90.1d	2.20E-16	2.59E-16	1.181
Tc-98	B-	4.2E+6y	1.46E-15	1.60E-15	1.096
Tc-99	B-	2.111E+5y	2.34E-16	2.54E-16	1.085
Tc-99m	ITB-	6.015h	1.40E-16	1.90E-16	1.36
Tc-101	B-	14.2m	1.36E-15	1.43E-15	1.054
Tc-102	B-	5.28s	4.55E-15	4.56E-15	1.002
Tc-102m	B-IT	4.35m	3.66E-15	3.81E-15	1.042
Tc-104	B-	18.3m	5.32E-15	5.45E-15	1.026
Tc-105	B-	7.6m	3.55E-15	3.66E-15	1.03
Ru-92	ECB+	3.65m	3.48E-15	3.80E-15	1.091
Ru-94	ECB+	51.8m	4.48E-16	5.28E-16	1.179
Ru-95	ECB+	1.643h	1.17E-15	1.29E-15	1.109
Ru-97	EC	2.9d	2.38E-16	3.10E-16	1.303
Ru-103	B-	39.26d	5.53E-16	6.27E-16	1.133
Ru-105	B-	4.44h	1.62E-15	1.72E-15	1.064

Radionuclide	Decay Mode	Halflife	Gy/Bq s	Sv / Bq s	RBE
Ru-106	B-	373.59d	2.32E-17	3.52E-17	1.522
Ru-107	B-	3.75m	2.74E-15	2.78E-15	1.014
Ru-108	B-	4.55m	1.16E-15	1.20E-15	1.036
Rh-94	ECB+	70.6s	9.54E-15	9.78E-15	1.025
Rh-95	ECB+	5.02m	4.01E-15	4.18E-15	1.044
Rh-95m	ITECB+	1.96m	1.08E-15	1.15E-15	1.065
Rh-96	ECB+	9.90m	4.78E-15	5.09E-15	1.066
Rh-96m	ITECB+	1.51m	2.29E-15	2.40E-15	1.048
Rh-97	ECB+	30.7m	2.34E-15	2.49E-15	1.066
Rh-97m	ECB+IT	46.2m	2.05E-15	2.18E-15	1.067
Rh-98	ECB+	8.7m	4.52E-15	4.70E-15	1.039
Rh-99	ECB+	16.1d	6.13E-16	7.28E-16	1.187
Rh-99m	ECB+	4.7h	6.14E-16	7.08E-16	1.154
Rh-100	ECB+	20.8h	2.12E-15	2.28E-15	1.074
Rh-100m	ITECB+	4.6m	2.58E-16	3.30E-16	1.28
Rh-101	EC	3.3y	3.09E-16	4.05E-16	1.311
Rh-101m	ECIT	4.34d	2.92E-16	3.62E-16	1.241
Rh-102	ECB+B-	207d	8.12E-16	8.87E-16	1.092
Rh-102m	ECB+IT	3.742y	1.75E-15	1.96E-15	1.118
Rh-103m	IT	56.114m	9.04E-17	1.19E-16	1.313
Rh-104	B-EC	42.3s	2.28E-15	2.29E-15	1.005
Rh-104m	ITB-	4.34m	2.53E-16	3.21E-16	1.268

Radionuclide	Decay Mode	Halflife	Gy/Bq s	Sv / Bq s	RBE
Rh-105	B-	35.36h	4.15E-16	4.48E-16	1.077
Rh-106	B-	29.80s	3.42E-15	3.45E-15	1.007
Rh-106m	B-	131m	3.02E-15	3.26E-15	1.077
Rh-107	B-	21.7m	1.27E-15	1.34E-15	1.055
Rh-108	B-	16.8s	4.46E-15	4.50E-15	1.009
Rh-109	B-	80s	2.39E-15	2.46E-15	1.028
Pd-96	ECB+	122s	1.67E-15	1.83E-15	1.097
Pd-97	ECB+	3.10m	3.53E-15	3.72E-15	1.053
Pd-98	ECB+	17.7m	4.57E-16	5.49E-16	1.202
Pd-99	ECB+	21.4m	2.04E-15	2.19E-15	1.073
Pd-100	EC	3.63d	2.40E-16	3.34E-16	1.391
Pd-101	ECB+	8.47h	3.85E-16	4.73E-16	1.228
Pd-103	EC	16.991d	4.20E-17	6.66E-17	1.588
Pd-107	B-	6.5E+6y	2.21E-17	3.41E-17	1.542
Pd-109	B-	13.7012h	1.03E-15	1.09E-15	1.058
Pd-109m	IT	4.69m	2.74E-16	3.20E-16	1.167
Pd-111	B-	23.4m	1.98E-15	1.99E-15	1.008
Pd-112	B-	21.03h	2.18E-16	2.60E-16	1.194
Pd-114	B-	2.42m	1.25E-15	1.27E-15	1.019
Ag-99	ECB+	124s	4.79E-15	5.00E-15	1.042
Ag-100m	ECB+	2.24m	6.58E-15	6.79E-15	1.033
Ag-101	ECB+	11.1m	3.18E-15	3.35E-15	1.054

Radionuclide	Decay Mode	Halflife	Gy/Bq s	Sv / Bq s	RBE
Ag-102	ECB+	12.9m	4.54E-15	4.79E-15	1.055
Ag-102m	ECB+IT	7.7m	2.33E-15	2.45E-15	1.05
Ag-103	ECB+	65.7m	1.13E-15	1.25E-15	1.105
Ag-104	ECB+	69.2m	2.33E-15	2.55E-15	1.094
Ag-104m	ECB+IT	33.5m	3.07E-15	3.22E-15	1.051
Ag-105	EC	41.29d	4.75E-16	5.76E-16	1.212
Ag-105m	ITECB+	7.23m	5.96E-17	8.66E-17	1.454
Ag-106	ECB+B-	23.96m	1.72E-15	1.81E-15	1.055
Ag-106m	EC	8.28d	2.24E-15	2.48E-15	1.107
Ag-108	B-ECB+	2.37m	1.42E-15	1.43E-15	1.012
Ag-108m	ECIT	418y	1.35E-15	1.54E-15	1.138
Ag-109m	IT	39.6s	1.95E-16	2.34E-16	1.199
Ag-110	B-EC	24.6s	2.75E-15	2.76E-15	1.004
Ag-110m	B-IT	249.76d	2.32E-15	2.53E-15	1.088
Ag-111	B-	7.45d	8.38E-16	8.62E-16	1.03
Ag-111m	ITB-	64.8s	1.42E-16	1.77E-16	1.247
Ag-112	B-	3.130h	3.65E-15	3.70E-15	1.013
Ag-113	B-	5.37h	1.81E-15	1.84E-15	1.012
Ag-113m	ITB-	68.7s	6.98E-16	7.56E-16	1.083
Ag-114	B-	4.6s	5.06E-15	5.08E-15	1.004
Ag-115	B-	20.0m	2.88E-15	2.92E-15	1.015
Ag-116	B-	2.68m	5.57E-15	5.67E-15	1.019

Radionuclide	Decay Mode	Halflife	Gy/Bq s	Sv / Bq s	RBE
Ag-117	B-	73.6s	3.87E-15	3.94E-15	1.019
Cd-101	ECB+	1.36m	4.35E-15	4.55E-15	1.046
Cd-102	ECB+	5.5m	8.55E-16	9.68E-16	1.132
Cd-103	ECB+	7.3m	2.38E-15	2.51E-15	1.058
Cd-104	EC	57.7m	2.97E-16	3.72E-16	1.25
Cd-105	ECB+	55.5m	1.48E-15	1.58E-15	1.067
Cd-107	ECB+	6.50h	2.55E-16	3.21E-16	1.26
Cd-109	EC	461.4d	2.37E-16	3.02E-16	1.271
Cd-111m	IT	48.50m	4.81E-16	5.72E-16	1.189
Cd-113	B-	7.7E+15y	2.14E-16	2.33E-16	1.091
Cd-113m	B-IT	14.1y	4.26E-16	4.46E-16	1.046
Cd-115	B-	53.46h	8.90E-16	9.34E-16	1.049
Cd-115m	B-	44.6d	1.42E-15	1.44E-15	1.012
Cd-117	B-	2.49h	1.83E-15	1.92E-15	1.05
Cd-117m	B-	3.36h	2.01E-15	2.12E-15	1.053
Cd-118	B-	50.3m	3.72E-16	3.92E-16	1.052
Cd-119	B-	2.69m	3.08E-15	3.18E-15	1.032
Cd-119m	B-	2.20m	3.27E-15	3.39E-15	1.036
In-103	ECB+	60s	5.63E-15	5.85E-15	1.038
In-105	ECB+	5.07m	3.89E-15	4.07E-15	1.048
In-106	ECB+	6.2m	5.31E-15	5.62E-15	1.057
In-106m	ECB+	5.2m	5.77E-15	5.97E-15	1.034

Radionuclide	Decay Mode	Halflife	Gy/Bq s	Sv / Bq s	RBE
In-107	ECB+	32.4m	1.91E-15	2.05E-15	1.071
In-108	ECB+	58.0m	3.41E-15	3.71E-15	1.088
In-108m	ECB+	39.6m	3.59E-15	3.75E-15	1.045
In-109	ECB+	4.2h	5.97E-16	6.96E-16	1.167
In-109m	IT	1.34m	5.86E-16	6.45E-16	1.102
In-110	ECB+	4.9h	2.48E-15	2.74E-15	1.103
In-110m	ECB+	69.1m	2.69E-15	2.84E-15	1.057
In-111	EC	2.8047d	4.23E-16	5.43E-16	1.283
In-111m	IT	7.7m	5.38E-16	5.95E-16	1.107
In-112	ECB+B-	14.97m	7.87E-16	8.37E-16	1.063
In-112m	IT	20.56m	3.23E-16	3.70E-16	1.148
In-113m	IT	1.6579h	5.29E-16	5.81E-16	1.098
In-114	B-ECB+	71.9s	1.79E-15	1.80E-15	1.007
In-114m	ITEC	49.51d	4.08E-16	4.56E-16	1.119
In-115	B-	4.41E+14y	3.52E-16	3.72E-16	1.055
In-115m	ITB-	4.486h	5.42E-16	5.88E-16	1.086
In-116m	B-	54.41m	2.56E-15	2.70E-15	1.054
In-117	B-	43.2m	1.18E-15	1.30E-15	1.104
In-117m	B-IT	116.2m	1.08E-15	1.12E-15	1.035
In-118	B-	5.0s	4.40E-15	4.41E-15	1.002
In-118m	B-	4.364m	3.67E-15	3.84E-15	1.046
In-119	B-	2.4m	2.03E-15	2.14E-15	1.05

Radionuclide	Decay Mode	Halflife	Gy/Bq s	Sv / Bq s	RBE
In-119m	B-IT	18.0m	2.41E-15	2.43E-15	1.009
In-121	B-	23.1s	3.00E-15	3.07E-15	1.024
In-121m	B-IT	3.88m	3.59E-15	3.62E-15	1.01
Sn-106	ECB+	1.92m	1.27E-15	1.43E-15	1.125
Sn-108	ECB+	10.30m	6.29E-16	7.59E-16	1.206
Sn-109	ECB+	18.0m	1.77E-15	1.90E-15	1.073
Sn-110	EC	4.11h	2.85E-16	3.63E-16	1.273
Sn-111	ECB+	35.3m	8.36E-16	9.02E-16	1.078
Sn-113	EC	115.09d	5.16E-17	8.00E-17	1.552
Sn-113m	ITEC	21.4m	1.59E-16	2.00E-16	1.257
Sn-117m	IT	13.76d	5.15E-16	6.07E-16	1.179
Sn-119m	IT	293.1d	2.07E-16	2.74E-16	1.323
Sn-121	B-	27.03h	2.67E-16	2.86E-16	1.074
Sn-121m	ITB-	43.9y	9.05E-17	1.21E-16	1.338
Sn-123	B-	129.2d	1.21E-15	1.23E-15	1.015
Sn-123m	B-	40.06m	1.22E-15	1.28E-15	1.052
Sn-125	B-	9.64d	2.11E-15	2.14E-15	1.015
Sn-125m	B-	9.52m	2.14E-15	2.20E-15	1.031
Sn-126	B-	2.30E+5y	3.76E-16	4.67E-16	1.245
Sn-127	B-	2.10h	2.64E-15	2.77E-15	1.051
Sn-127m	B-	4.13m	3.02E-15	3.08E-15	1.021
Sn-128	B-	59.07m	1.09E-15	1.27E-15	1.158

Radionuclide	Decay Mode	Halflife	Gy/Bq s	Sv / Bq s	RBE
Sn-129	B-	2.23m	3.69E-15	3.77E-15	1.022
Sn-130	B-	3.72m	1.83E-15	1.99E-15	1.089
Sn-130m	B-	1.7m	3.93E-15	4.03E-15	1.025
Sb-111	ECB+	75s	4.34E-15	4.53E-15	1.042
Sb-113	ECB+	6.67m	2.69E-15	2.84E-15	1.057
Sb-114	ECB+	3.49m	4.87E-15	5.05E-15	1.038
Sb-115	ECB+	32.1m	1.27E-15	1.39E-15	1.095
Sb-116	ECB+	15.8m	2.91E-15	3.06E-15	1.051
Sb-116m	ECB+	60.3m	2.74E-15	3.00E-15	1.096
Sb-117	ECB+	2.80h	2.37E-16	3.11E-16	1.31
Sb-118	ECB+	3.6m	2.67E-15	2.76E-15	1.037
Sb-118m	ECB+	5.00h	2.12E-15	2.35E-15	1.107
Sb-119	EC	38.19h	1.01E-16	1.56E-16	1.545
Sb-120	ECB+	15.89m	1.09E-15	1.16E-15	1.065
Sb-120m	EC	5.76d	2.02E-15	2.24E-15	1.108
Sb-122	B-ECB+	2.7238d	1.66E-15	1.72E-15	1.037
Sb-122m	IT	4.191m	2.99E-16	4.03E-16	1.347
Sb-124	B-	60.20d	2.27E-15	2.40E-15	1.054
Sb-124m	ITB-	93s	6.22E-16	6.90E-16	1.11
Sb-124n	IT	20.2m	6.00E-17	8.89E-17	1.482
Sb-125	B-	2.75856y	5.98E-16	6.93E-16	1.159
Sb-126	B-	12.35d	3.02E-15	3.29E-15	1.091

Radionuclide	Decay Mode	Halflife	Gy/Bq s	Sv / Bq s	RBE
Sb-126m	B-IT	19.15m	2.70E-15	2.87E-15	1.063
Sb-127	B-	3.85d	1.28E-15	1.38E-15	1.071
Sb-128	B-	9.01h	3.61E-15	3.90E-15	1.08
Sb-128m	B-IT	10.4m	3.73E-15	3.91E-15	1.049
Sb-129	B-	4.40h	2.03E-15	2.15E-15	1.055
Sb-130	B-	39.5m	4.31E-15	4.60E-15	1.069
Sb-130m	B-	6.3m	4.49E-15	4.70E-15	1.047
Sb-131	B-	23.03m	2.91E-15	3.04E-15	1.045
Sb-133	B-	2.5m	3.56E-15	3.70E-15	1.037
Te-113	ECB+	1.7m	5.63E-15	5.79E-15	1.03
Te-114	ECB+	15.2m	1.35E-15	1.50E-15	1.112
Te-115	ECB+	5.8m	3.61E-15	3.79E-15	1.049
Te-115m	ECB+	6.7m	3.59E-15	3.77E-15	1.051
Te-116	ECB+	2.49h	2.61E-16	3.38E-16	1.292
Te-117	ECB+	62m	1.68E-15	1.80E-15	1.072
Te-118	EC	6.00d	4.81E-17	7.65E-17	1.591
Te-119	ECB+	16.05h	6.59E-16	7.50E-16	1.139
Te-119m	ECB+	4.70d	1.20E-15	1.34E-15	1.11
Te-121	EC	19.16d	5.07E-16	5.94E-16	1.172
Te-121m	ITEC	154d	3.73E-16	4.62E-16	1.238
Te-123	EC	6.00E+14y	7.15E-18	1.98E-17	2.763
Te-123m	IT	119.25d	3.58E-16	4.43E-16	1.238

Radionuclide	Decay Mode	Halflife	Gy/Bq s	Sv / Bq s	RBE
Te-125m	IT	57.40d	3.11E-16	3.95E-16	1.271
Te-127	B-	9.35h	5.22E-16	5.43E-16	1.039
Te-127m	ITB-	109d	2.09E-16	2.51E-16	1.202
Te-129	B-	69.6m	1.31E-15	1.36E-15	1.04
Te-129m	ITB-	33.6d	6.62E-16	6.98E-16	1.055
Te-131	B-	25.0m	1.98E-15	2.05E-15	1.039
Te-131m	B-IT	30h	1.57E-15	1.71E-15	1.092
Te-132	B-	3.204d	4.62E-16	5.72E-16	1.238
Te-133	B-	12.5m	2.50E-15	2.61E-15	1.043
Te-133m	B-IT	55.4m	2.33E-15	2.49E-15	1.069
Te-134	B-	41.8m	1.23E-15	1.37E-15	1.117
I-118	ECB+	13.7m	6.13E-15	6.31E-15	1.031
I-118m	ECB+	8.5m	5.52E-15	5.86E-15	1.06
I-119	ECB+	19.1m	1.92E-15	2.06E-15	1.072
I-120	ECB+	81.6m	4.65E-15	4.83E-15	1.038
I-120m	ECB+	53m	4.83E-15	5.12E-15	1.06
I-121	ECB+	2.12h	4.90E-16	5.83E-16	1.191
I-122	ECB+	3.63m	3.33E-15	3.44E-15	1.034
I-123	EC	13.27h	2.24E-16	2.99E-16	1.332
I-124	ECB+	4.1760d	1.32E-15	1.43E-15	1.082
I-125	EC	59.400d	1.15E-16	1.84E-16	1.598
I-126	ECB+B-	12.93d	7.29E-16	7.99E-16	1.097

Radionuclide	Decay Mode	Halflife	Gy/Bq s	Sv / Bq s	RBE
I-128	B-ECB+	24.99m	1.78E-15	1.80E-15	1.012
I-129	B-	1.57E+7y	1.89E-16	2.48E-16	1.314
I-130	B-	12.36h	2.35E-15	2.57E-15	1.093
I-130m	ITB-	8.84m	5.02E-16	5.43E-16	1.082
I-131	B-	8.02070d	7.50E-16	8.27E-16	1.103
I-132	B-	2.295h	2.92E-15	3.11E-15	1.066
I-132m	ITB-	1.387h	6.54E-16	7.49E-16	1.146
I-133	B-	20.8h	1.45E-15	1.53E-15	1.056
I-134	B-	52.5m	3.35E-15	3.54E-15	1.058
I-134m	ITB-	3.60m	4.61E-16	5.55E-16	1.205
I-135	B-	6.57h	1.98E-15	2.07E-15	1.047
Xe-120	ECB+	40m	4.60E-16	5.72E-16	1.242
Xe-121	ECB+	40.1m	2.45E-15	2.58E-15	1.056
Xe-122	EC	20.1h	9.71E-17	1.37E-16	1.413
Xe-123	ECB+	2.08h	9.48E-16	1.06E-15	1.113
Xe-125	ECB+	16.9h	3.23E-16	4.18E-16	1.293
Xe-127	EC	36.4d	3.20E-16	4.14E-16	1.295
Xe-127m	IT	69.2s	4.46E-16	5.34E-16	1.199
Xe-129m	IT	8.88d	4.99E-16	5.93E-16	1.187
Xe-131m	IT	11.84d	3.69E-16	4.20E-16	1.138
Xe-133	B-	5.243d	3.70E-16	4.33E-16	1.172
Xe-133m	IT	2.19d	4.90E-16	5.42E-16	1.105

Radionuclide	Decay Mode	Halflife	Gy/Bq s	Sv / Bq s	RBE
Xe-135	B-	9.14h	9.38E-16	1.01E-15	1.075
Xe-135m	ITB-	15.29m	5.79E-16	6.36E-16	1.098
Xe-137	B-	3.818m	4.06E-15	4.08E-15	1.006
Xe-138	B-	14.08m	2.33E-15	2.43E-15	1.045
Cs-121	ECB+	155s	4.96E-15	5.10E-15	1.029
Cs-121m	ECB+IT	122s	4.06E-15	4.23E-15	1.04
Cs-123	ECB+	5.88m	3.08E-15	3.22E-15	1.048
Cs-124	ECB+	30.8s	5.52E-15	5.65E-15	1.023
Cs-125	ECB+	45m	1.43E-15	1.53E-15	1.073
Cs-126	ECB+	1.64m	3.97E-15	4.11E-15	1.034
Cs-127	ECB+	6.25h	4.34E-16	5.23E-16	1.205
Cs-128	ECB+	3.640m	2.74E-15	2.85E-15	1.041
Cs-129	ECB+	32.06h	2.91E-16	3.75E-16	1.286
Cs-130	ECB+B-	29.21m	1.31E-15	1.38E-15	1.058
Cs-130m	ITEC	3.46m	2.99E-16	3.99E-16	1.332
Cs-131	EC	9.689d	5.13E-17	8.20E-17	1.599
Cs-132	ECB+B-	6.479d	6.24E-16	7.17E-16	1.15
Cs-134	B-EC	2.0648y	1.62E-15	1.77E-15	1.092
Cs-134m	IT	2.903h	2.90E-16	3.62E-16	1.251
Cs-135	B-	2.3E+6y	2.06E-16	2.26E-16	1.095
Cs-135m	IT	53m	1.35E-15	1.46E-15	1.088
Cs-136	B-	13.16d	1.99E-15	2.18E-15	1.094

Radionuclide	Decay Mode	Halflife	Gy/Bq s	Sv / Bq s	RBE
Cs-137	B-	30.1671y	4.34E-16	4.54E-16	1.045
Cs-138	B-	33.41m	4.60E-15	4.71E-15	1.024
Cs-138m	ITB-	2.91m	1.06E-15	1.13E-15	1.065
Cs-139	B-	9.27m	4.04E-15	4.06E-15	1.004
Cs-140	B-	63.7s	5.71E-15	5.79E-15	1.014
Ba-124	ECB+	11.0m	8.74E-16	9.74E-16	1.115
Ba-126	ECB+	100m	5.15E-16	6.03E-16	1.172
Ba-127	ECB+	12.7m	1.97E-15	2.08E-15	1.055
Ba-128	EC	2.43d	9.12E-17	1.31E-16	1.435
Ba-129	ECB+	2.23h	5.71E-16	6.42E-16	1.124
Ba-129m	ECB+	2.16h	1.34E-15	1.54E-15	1.145
Ba-131	EC	11.50d	5.11E-16	6.23E-16	1.219
Ba-131m	IT	14.6m	3.28E-16	4.09E-16	1.246
Ba-133	EC	10.52y	4.81E-16	6.12E-16	1.273
Ba-133m	ITEC	38.9h	5.90E-16	6.71E-16	1.136
Ba-135m	IT	28.7h	5.41E-16	5.91E-16	1.093
Ba-137m	IT	2.552m	6.31E-16	6.91E-16	1.096
Ba-139	B-	83.06m	2.12E-15	2.14E-15	1.012
Ba-140	B-	12.752d	8.92E-16	9.85E-16	1.104
Ba-141	B-	18.27m	2.94E-15	3.05E-15	1.038
Ba-142	B-	10.6m	1.77E-15	1.89E-15	1.065
La-128	ECB+	5.18m	5.30E-15	5.57E-15	1.051

Radionuclide	Decay Mode	Halflife	Gy/Bq s	Sv / Bq s	RBE
La-129	ECB+	11.6m	2.16E-15	2.30E-15	1.064
La-130	ECB+	8.7m	4.31E-15	4.52E-15	1.05
La-131	ECB+	59m	1.00E-15	1.13E-15	1.124
La-132	ECB+	4.8h	2.83E-15	3.00E-15	1.06
La-132m	ITECB+	24.3m	8.06E-16	9.33E-16	1.157
La-133	ECB+	3.912h	2.63E-16	3.38E-16	1.286
La-134	ECB+	6.45m	2.35E-15	2.44E-15	1.039
La-135	ECB+	19.5h	6.26E-17	9.59E-17	1.532
La-136	ECB+	9.87m	1.02E-15	1.09E-15	1.066
La-137	EC	6.0E+4y	5.27E-17	8.44E-17	1.601
La-138	ECB-	1.02E+11y	1.02E-15	1.10E-15	1.079
La-140	B-	1.6781d	2.94E-15	3.07E-15	1.046
La-141	B-	3.92h	2.30E-15	2.31E-15	1.005
La-142	B-	91.1m	3.64E-15	3.73E-15	1.026
La-143	B-	14.2m	3.19E-15	3.21E-15	1.006
Ce-130	ECB+	22.9m	5.88E-16	7.02E-16	1.193
Ce-131	ECB+	10.2m	2.70E-15	2.91E-15	1.076
Ce-132	EC	3.51h	2.78E-16	3.69E-16	1.326
Ce-133	ECB+	97m	1.35E-15	1.49E-15	1.105
Ce-133m	ECB+	4.9h	1.53E-15	1.71E-15	1.12
Ce-134	EC	3.16d	5.68E-17	9.02E-17	1.587
Ce-135	ECB+	17.7h	7.44E-16	8.75E-16	1.176

Radionuclide	Decay Mode	Halflife	Gy/Bq s	Sv / Bq s	RBE
Ce-137	ECB+	9.0h	8.84E-17	1.52E-16	1.714
Ce-137m	ITEC	34.4h	5.34E-16	5.88E-16	1.1
Ce-139	EC	137.641d	2.28E-16	3.05E-16	1.335
Ce-141	B-	32.508d	4.60E-16	5.11E-16	1.112
Ce-143	B-	33.039h	1.25E-15	1.34E-15	1.078
Ce-144	B-	284.91d	2.29E-16	2.59E-16	1.132
Ce-145	B-	3.01m	2.24E-15	2.38E-15	1.065
Pr-134	ECB+	11m	4.98E-15	5.30E-15	1.065
Pr-134m	ECB+	17m	5.30E-15	5.50E-15	1.038
Pr-135	ECB+	24m	2.05E-15	2.19E-15	1.069
Pr-136	ECB+	13.1m	3.40E-15	3.59E-15	1.056
Pr-137	ECB+	1.28h	7.56E-16	8.20E-16	1.085
Pr-138	ECB+	1.45m	3.34E-15	3.44E-15	1.03
Pr-138m	ECB+	2.12h	2.47E-15	2.70E-15	1.094
Pr-139	ECB+	4.41h	2.30E-16	2.73E-16	1.189
Pr-140	ECB+	3.39m	1.72E-15	1.80E-15	1.046
Pr-142	B-EC	19.12h	1.91E-15	1.93E-15	1.007
Pr-142m	IT	14.6m	8.60E-18	2.41E-17	2.8
Pr-143	B-	13.57d	7.27E-16	7.47E-16	1.028
Pr-144	B-	17.28m	2.81E-15	2.82E-15	1.003
Pr-144m	ITB-	7.2m	1.27E-16	1.70E-16	1.333
Pr-145	B-	5.984h	1.58E-15	1.59E-15	1.01

Radionuclide	Decay Mode	Halflife	Gy/Bq s	Sv / Bq s	RBE
Pr-146	B-	24.15m	3.82E-15	3.88E-15	1.018
Pr-147	B-	13.4m	2.46E-15	2.58E-15	1.051
Pr-148	B-	2.29m	4.58E-15	4.66E-15	1.017
Pr-148m	B-	2.01m	4.62E-15	4.73E-15	1.025
Nd-134	ECB+	8.5m	8.48E-16	9.68E-16	1.141
Nd-135	ECB+	12.4m	3.46E-15	3.69E-15	1.064
Nd-136	ECB+	50.65m	4.36E-16	5.49E-16	1.259
Nd-137	ECB+	38.5m	1.69E-15	1.84E-15	1.091
Nd-138	EC	5.04h	7.12E-17	1.09E-16	1.535
Nd-139	ECB+	29.7m	8.48E-16	9.20E-16	1.085
Nd-139m	ECB+IT	5.50h	1.44E-15	1.62E-15	1.123
Nd-140	EC	3.37d	5.59E-17	9.08E-17	1.624
Nd-141	ECB+	2.49h	1.15E-16	1.54E-16	1.338
Nd-141m	ITECB+	62.0s	6.97E-16	7.55E-16	1.084
Nd-147	B-	10.98d	7.46E-16	8.19E-16	1.097
Nd-149	B-	1.728h	1.47E-15	1.57E-15	1.072
Nd-151	B-	12.44m	2.09E-15	2.21E-15	1.053
Nd-152	B-	11.4m	8.98E-16	9.66E-16	1.075
Pm-136	ECB+	107s	7.12E-15	7.40E-15	1.039
Pm-137m	ECB+	2.4m	4.00E-15	4.26E-15	1.065
Pm-139	ECB+	4.15m	3.16E-15	3.27E-15	1.036
Pm-140	ECB+	9.2s	5.56E-15	5.67E-15	1.021

Radionuclide	Decay Mode	Halflife	Gy/Bq s	Sv / Bq s	RBE
Pm-140m	ECB+	5.95m	4.69E-15	4.96E-15	1.058
Pm-141	ECB+	20.90m	1.98E-15	2.07E-15	1.044
Pm-142	ECB+	40.5s	3.72E-15	3.82E-15	1.027
Pm-143	EC	265d	2.87E-16	3.46E-16	1.204
Pm-144	EC	363d	1.31E-15	1.49E-15	1.138
Pm-146	ECB-	5.53y	8.29E-16	9.32E-16	1.124
Pm-147	B-	2.6234y	1.43E-16	1.61E-16	1.126
Pm-148	B-	5.368d	2.12E-15	2.16E-15	1.022
Pm-148m	B-IT	41.29d	1.98E-15	2.20E-15	1.108
Pm-149	B-	53.08h	8.52E-16	8.75E-16	1.027
Pm-150	B-	2.68h	2.98E-15	3.10E-15	1.038
Pm-151	B-	28.40h	9.72E-16	1.07E-15	1.103
Pm-152	B-	4.12m	3.29E-15	3.33E-15	1.012
Pm-152m	B-	7.52m	3.26E-15	3.43E-15	1.054
Pm-153	B-	5.25m	1.66E-15	1.72E-15	1.038
Pm-154	B-	1.73m	3.31E-15	3.42E-15	1.035
Pm-154m	B-	2.68m	3.55E-15	3.73E-15	1.049
Sm-139	ECB+	2.57m	3.66E-15	3.84E-15	1.047
Sm-140	ECB+	14.82m	8.53E-16	9.43E-16	1.107
Sm-141	ECB+	10.2m	2.75E-15	2.90E-15	1.054
Sm-141m	ECB+IT	22.6m	2.45E-15	2.66E-15	1.085
Sm-142	ECB+	72.49m	2.07E-16	2.51E-16	1.216

Radionuclide	Decay Mode	Halflife	Gy/Bq s	Sv / Bq s	RBE
Sm-143	ECB+	8.75m	1.58E-15	1.66E-15	1.049
Sm-143m	ITECB+	66s	7.12E-16	7.71E-16	1.083
Sm-145	EC	340d	1.53E-16	2.35E-16	1.537
Sm-151	B-	90y	4.61E-17	6.04E-17	1.31
Sm-153	B-	46.50h	6.86E-16	7.64E-16	1.113
Sm-155	B-	22.3m	1.39E-15	1.45E-15	1.042
Sm-156	B-	9.4h	5.79E-16	6.65E-16	1.148
Sm-157	B-	8.03m	2.35E-15	2.43E-15	1.036
Eu-142	ECB+	2.34s	7.33E-15	7.45E-15	1.017
Eu-142m	ECB+	1.223m	6.79E-15	7.12E-15	1.048
Eu-143	ECB+	2.59m	4.04E-15	4.15E-15	1.028
Eu-144	ECB+	10.2s	5.65E-15	5.77E-15	1.02
Eu-145	ECB+	5.93d	1.04E-15	1.15E-15	1.105
Eu-146	ECB+	4.61d	1.97E-15	2.18E-15	1.102
Eu-149	EC	93.1d	1.26E-16	1.94E-16	1.544
Eu-150	ECB+	36.9y	1.32E-15	1.52E-15	1.156
Eu-150m	B-ECB+	12.8h	7.61E-16	7.88E-16	1.036
Eu-152	ECB+B-	13.537y	1.22E-15	1.35E-15	1.111
Eu-152m	B-ECB+	9.3116h	1.40E-15	1.45E-15	1.033
Eu-152n	IT	96m	2.22E-16	3.21E-16	1.446
Eu-154	B-EC	8.593y	1.60E-15	1.73E-15	1.082
Eu-154m	IT	46.0m	2.44E-16	3.79E-16	1.552

Radionuclide	Decay Mode	Halflife	Gy/Bq s	Sv / Bq s	RBE
Eu-155	B-	4.7611y	2.04E-16	2.62E-16	1.286
Eu-156	B-	15.19d	1.97E-15	2.05E-15	1.045
Eu-157	B-	15.18h	1.17E-15	1.28E-15	1.102
Eu-158	B-	45.9m	3.05E-15	3.16E-15	1.038
Eu-159	B-	18.1m	2.32E-15	2.42E-15	1.045
Gd-142	ECB+	70.2s	2.53E-15	2.65E-15	1.047
Gd-143m	ECB+	110.0s	4.63E-15	4.88E-15	1.053
Gd-144	ECB+	4.47m	2.05E-15	2.14E-15	1.046
Gd-145	ECB+	23.0m	2.53E-15	2.65E-15	1.05
Gd-145m	ITECB+	85s	9.93E-16	1.10E-15	1.103
Gd-146	EC	48.27d	5.31E-16	7.00E-16	1.319
Gd-147	ECB+	38.1h	1.26E-15	1.44E-15	1.145
Gd-149	ECB+	9.28d	6.00E-16	7.30E-16	1.216
Gd-153	EC	240.4d	2.09E-16	2.99E-16	1.429
Gd-159	B-	18.479h	7.61E-16	8.01E-16	1.053
Gd-162	B-	8.4m	1.12E-15	1.21E-15	1.085
Tb-146	ECB+	23s	6.06E-15	6.26E-15	1.033
Tb-147	ECB+	1.64h	2.33E-15	2.51E-15	1.077
Tb-147m	ECB+	1.87m	2.16E-15	2.28E-15	1.056
Tb-148	ECB+	60m	3.73E-15	3.91E-15	1.048
Tb-148m	ECB+	2.20m	3.22E-15	3.52E-15	1.096
Tb-150m	ECB+	5.8m	2.33E-15	2.62E-15	1.127

Radionuclide	Decay Mode	Halflife	Gy/Bq s	Sv / Bq s	RBE
Tb-151m	ITECB+	25s	2.57E-16	3.67E-16	1.431
Tb-152	ECB+	17.5h	1.71E-15	1.85E-15	1.084
Tb-152m	ITECB+	4.2m	9.77E-16	1.17E-15	1.195
Tb-153	ECB+	2.34d	3.95E-16	5.14E-16	1.302
Tb-154	ECB+	21.5h	1.79E-15	1.94E-15	1.081
Tb-155	EC	5.32d	2.64E-16	3.73E-16	1.413
Tb-156	EC	5.35d	1.70E-15	1.92E-15	1.13
Tb-156m	IT	24.4h	7.97E-17	1.24E-16	1.56
Tb-156n	IT	5.3h	2.08E-16	2.52E-16	1.212
Tb-157	EC	71y	2.11E-17	4.57E-17	2.167
Tb-158	ECB-	180y	9.03E-16	1.03E-15	1.143
Tb-160	B-	72.3d	1.47E-15	1.60E-15	1.088
Tb-161	B-	6.906d	5.11E-16	6.02E-16	1.178
Tb-162	B-	7.60m	2.11E-15	2.26E-15	1.074
Tb-163	B-	19.5m	1.47E-15	1.60E-15	1.092
Tb-164	B-	3.0m	3.79E-15	4.03E-15	1.065
Tb-165	B-	2.11m	2.70E-15	2.77E-15	1.027
Dy-148	ECB+	3.3m	6.53E-16	7.56E-16	1.158
Dy-149	ECB+	4.20m	1.50E-15	1.66E-15	1.108
Dy-155	ECB+	9.9h	5.98E-16	7.15E-16	1.196
Dy-157	EC	8.14h	3.24E-16	4.19E-16	1.295
Dy-159	EC	144.4d	8.39E-17	1.38E-16	1.638

Radionuclide	Decay Mode	Halflife	Gy/Bq s	Sv / Bq s	RBE
Dy-165	B-	2.334h	1.06E-15	1.08E-15	1.028
Dy-165m	ITB-	1.257m	2.61E-16	3.06E-16	1.174
Dy-166	B-	81.6h	4.30E-16	5.11E-16	1.189
Dy-167	B-	6.20m	2.11E-15	2.22E-15	1.051
Dy-168	B-	8.7m	1.32E-15	1.44E-15	1.086
Ho-150	ECB+	76.8s	6.09E-15	6.27E-15	1.03
Ho-155	ECB+	48m	9.97E-16	1.13E-15	1.135
Ho-156	ECB+	56m	3.15E-15	3.38E-15	1.072
Ho-157	ECB+	12.6m	7.02E-16	8.67E-16	1.235
Ho-159	ECB+	33.05m	4.67E-16	6.27E-16	1.342
Ho-160	ECB+	25.6m	1.52E-15	1.72E-15	1.134
Ho-161	EC	2.48h	1.47E-16	2.29E-16	1.554
Ho-162	ECB+	15.0m	2.82E-16	3.56E-16	1.262
Ho-162m	ITECB+	67.0m	6.23E-16	7.73E-16	1.241
Ho-163	EC	4570y	1.35E-18	2.84E-18	2.101
Ho-164	ECB-	29m	3.73E-16	4.19E-16	1.125
Ho-164m	IT	38.0m	2.71E-16	3.98E-16	1.47
Ho-166	B-	26.80h	1.63E-15	1.67E-15	1.024
Ho-166m	B-	1.20E+3y	1.64E-15	1.88E-15	1.146
Ho-167	B-	3.1h	8.34E-16	9.35E-16	1.121
Ho-168	B-	2.99m	2.57E-15	2.68E-15	1.042
Ho-168m	IT	132s	1.29E-16	1.72E-16	1.335

Radionuclide	Decay Mode	Halflife	Gy/Bq s	Sv / Bq s	RBE
Ho-170	B-	2.76m	3.27E-15	3.49E-15	1.066
Er-156	EC	19.5m	2.96E-16	4.35E-16	1.466
Er-159	ECB+	36m	9.31E-16	1.06E-15	1.138
Er-161	ECB+	3.21h	9.09E-16	1.04E-15	1.148
Er-163	ECB+	75.0m	6.41E-17	1.06E-16	1.656
Er-165	EC	10.36h	6.15E-17	1.03E-16	1.672
Er-167m	IT	2.269s	3.37E-16	3.88E-16	1.153
Er-169	B-	9.40d	2.39E-16	2.68E-16	1.121
Er-171	B-	7.516h	1.28E-15	1.42E-15	1.112
Er-172	B-	49.3h	7.46E-16	8.67E-16	1.162
Er-173	B-	1.434m	2.33E-15	2.52E-15	1.08
Tm-161	ECB+	30.2m	1.54E-15	1.78E-15	1.155
Tm-162	ECB+	21.70m	2.72E-15	2.88E-15	1.059
Tm-163	ECB+	1.810h	1.19E-15	1.37E-15	1.152
Tm-164	ECB+	2.0m	1.99E-15	2.10E-15	1.052
Tm-165	ECB+	30.06h	6.13E-16	7.57E-16	1.235
Tm-166	ECB+	7.70h	1.69E-15	1.88E-15	1.111
Tm-167	EC	9.25d	4.43E-16	5.49E-16	1.24
Tm-168	ECB+B-	93.1d	1.20E-15	1.41E-15	1.173
Tm-170	B-EC	128.6d	7.61E-16	7.90E-16	1.038
Tm-171	B-	1.92y	5.95E-17	7.51E-17	1.264
Tm-172	B-	63.6h	1.58E-15	1.65E-15	1.04

Radionuclide	Decay Mode	Halflife	Gy/Bq s	Sv / Bq s	RBE
Tm-173	B-	8.24h	1.03E-15	1.11E-15	1.081
Tm-174	B-	5.4m	2.59E-15	2.86E-15	1.107
Tm-175	B-	15.2m	2.06E-15	2.19E-15	1.063
Tm-176	B-	1.85m	3.76E-15	3.96E-15	1.053
Yb-162	ECB+	18.87m	3.03E-16	4.10E-16	1.354
Yb-163	ECB+	11.05m	1.21E-15	1.33E-15	1.107
Yb-164	EC	75.8m	7.81E-17	1.24E-16	1.588
Yb-165	ECB+	9.9m	6.44E-16	8.31E-16	1.29
Yb-166	EC	56.7h	1.89E-16	2.86E-16	1.513
Yb-167	ECB+	17.5m	4.68E-16	6.82E-16	1.457
Yb-169	EC	32.026d	6.42E-16	8.84E-16	1.376
Yb-175	B-	4.185d	3.34E-16	3.62E-16	1.085
Yb-177	B-	1.911h	1.16E-15	1.21E-15	1.042
Yb-178	B-	74m	4.75E-16	5.02E-16	1.057
Yb-179	B-	8.0m	2.42E-15	2.55E-15	1.054
Lu-165	ECB+	10.74m	1.74E-15	1.92E-15	1.106
Lu-167	ECB+	51.5m	1.53E-15	1.71E-15	1.123
Lu-169	ECB+	34.06h	1.13E-15	1.29E-15	1.142
Lu-169m	IT	160s	6.70E-17	1.04E-16	1.558
Lu-170	ECB+	2.012d	1.95E-15	2.11E-15	1.08
Lu-171	ECB+	8.24d	7.60E-16	9.55E-16	1.258
Lu-171m	IT	79s	1.64E-16	2.07E-16	1.262

Radionuclide	Decay Mode	Halflife	Gy/Bq s	Sv / Bq s	RBE
Lu-172	ECB+	6.70d	1.80E-15	2.03E-15	1.131
Lu-172m	IT	3.7m	9.67E-17	1.36E-16	1.411
Lu-173	EC	1.37y	2.93E-16	4.20E-16	1.431
Lu-174	ECB+	3.31y	2.11E-16	2.84E-16	1.351
Lu-174m	ITEC	142d	3.43E-16	4.82E-16	1.407
Lu-176	B-	3.85E+10y	1.09E-15	1.25E-15	1.153
Lu-176m	B-EC	3.635h	1.12E-15	1.17E-15	1.042
Lu-177	B-	6.647d	3.70E-16	4.06E-16	1.095
Lu-177m	B-IT	160.4d	1.44E-15	1.77E-15	1.225
Lu-178	B-	28.4m	1.84E-15	1.87E-15	1.019
Lu-178m	B-	23.1m	1.98E-15	2.26E-15	1.139
Lu-179	B-	4.59h	1.15E-15	1.17E-15	1.022
Lu-180	B-	5.7m	2.62E-15	2.78E-15	1.059
Lu-181	B-	3.5m	2.43E-15	2.59E-15	1.063
Hf-167	ECB+	2.05m	1.65E-15	1.76E-15	1.067
Hf-169	ECB+	3.24m	8.32E-16	9.51E-16	1.143
Hf-170	EC	16.01h	5.32E-16	6.88E-16	1.294
Hf-172	EC	1.87y	3.05E-16	4.52E-16	1.484
Hf-173	ECB+	23.6h	4.54E-16	6.07E-16	1.337
Hf-175	EC	70d	4.01E-16	5.07E-16	1.264
Hf-177m	IT	51.4m	3.03E-15	3.64E-15	1.201
Hf-178m	IT	31y	2.30E-15	2.75E-15	1.196

Radionuclide	Decay Mode	Halflife	Gy/Bq s	Sv / Bq s	RBE
Hf-179m	IT	25.05d	1.20E-15	1.47E-15	1.231
Hf-180m	ITB-	5.5h	1.14E-15	1.37E-15	1.204
Hf-181	B-	42.39d	9.08E-16	1.04E-15	1.147
Hf-182	B-	9E+6y	3.39E-16	4.13E-16	1.219
Hf-182m	B-IT	61.5m	1.31E-15	1.52E-15	1.166
Hf-183	B-	1.067h	1.65E-15	1.77E-15	1.067
Hf-184	B-	4.12h	1.31E-15	1.52E-15	1.159
Ta-170	ECB+	6.76m	4.56E-15	4.73E-15	1.036
Ta-172	ECB+	36.8m	2.59E-15	2.80E-15	1.08
Ta-173	ECB+	3.14h	8.59E-16	1.02E-15	1.181
Ta-174	ECB+	1.14h	1.84E-15	2.01E-15	1.092
Ta-175	ECB+	10.5h	1.01E-15	1.18E-15	1.164
Ta-176	ECB+	8.09h	1.83E-15	2.00E-15	1.093
Ta-177	EC	56.56h	1.23E-16	1.80E-16	1.467
Ta-178	ECB+	9.31m	1.99E-16	2.65E-16	1.331
Ta-178m	EC	2.36h	1.32E-15	1.63E-15	1.235
Ta-179	EC	1.82y	4.63E-17	8.34E-17	1.801
Ta-180	ECB-	8.152h	1.81E-16	2.36E-16	1.303
Ta-182	B-	114.43d	1.48E-15	1.64E-15	1.108
Ta-182m	IT	15.84m	8.46E-16	1.05E-15	1.235
Ta-183	B-	5.1d	1.07E-15	1.27E-15	1.182
Ta-184	B-	8.7h	2.50E-15	2.77E-15	1.105

Radionuclide	Decay Mode	Halflife	Gy/Bq s	Sv / Bq s	RBE
Ta-185	B-	49.4m	1.85E-15	1.96E-15	1.061
Ta-186	B-	10.5m	3.61E-15	3.82E-15	1.059
W-177	ECB+	132m	9.73E-16	1.20E-15	1.235
W-178	EC	21.6d	3.63E-17	6.98E-17	1.926
W-179	EC	37.05m	1.38E-16	2.21E-16	1.593
W-179m	ITEC	6.40m	4.37E-16	5.01E-16	1.145
W-181	EC	121.2d	7.29E-17	1.30E-16	1.785
W-185	B-	75.1d	2.93E-16	3.13E-16	1.067
W-185m	IT	1.597m	4.33E-16	5.32E-16	1.229
W-187	B-	23.72h	1.06E-15	1.14E-15	1.082
W-188	B-	69.78d	2.32E-16	2.52E-16	1.087
W-190	B-	30.0m	1.24E-15	1.38E-15	1.112
Re-178	ECB+	13.2m	2.68E-15	2.86E-15	1.068
Re-179	ECB+	19.5m	1.00E-15	1.17E-15	1.169
Re-180	ECB+	2.44m	1.35E-15	1.52E-15	1.122
Re-181	ECB+	19.9h	9.69E-16	1.14E-15	1.18
Re-182	EC	64.0h	1.89E-15	2.21E-15	1.173
Re-182m	ECB+	12.7h	1.16E-15	1.33E-15	1.142
Re-183	EC	70.0d	4.01E-16	5.49E-16	1.368
Re-184	ECB+	38.0d	8.46E-16	9.78E-16	1.156
Re-184m	ITEC	169d	6.45E-16	7.94E-16	1.232
Re-186	B-EC	3.7183d	7.94E-16	8.27E-16	1.042

Radionuclide	Decay Mode	Halflife	Gy/Bq s	Sv / Bq s	RBE
Re-186m	IT	2.00E+5y	3.21E-16	4.42E-16	1.374
Re-187	B-	4.12E+10y	1.43E-18	6.26E-18	4.395
Re-188	B-	17.0040h	1.85E-15	1.88E-15	1.016
Re-188m	IT	18.59m	2.98E-16	4.15E-16	1.395
Re-189	B-	24.3h	7.98E-16	8.40E-16	1.052
Re-190	B-	3.1m	2.65E-15	2.84E-15	1.069
Re-190m	B-IT	3.2h	1.78E-15	1.94E-15	1.095
Os-180	ECB+	21.5m	1.88E-16	2.76E-16	1.467
Os-181	ECB+	105m	1.29E-15	1.48E-15	1.149
Os-182	EC	22.10h	4.92E-16	6.26E-16	1.272
Os-183	ECB+	13.0h	7.05E-16	8.81E-16	1.25
Os-183m	ECB+IT	9.9h	8.81E-16	9.86E-16	1.119
Os-185	EC	93.6d	6.07E-16	7.11E-16	1.171
Os-189m	IT	5.8h	7.12E-17	1.09E-16	1.531
Os-190m	IT	9.9m	1.55E-15	1.81E-15	1.168
Os-191	B-	15.4d	3.97E-16	5.14E-16	1.295
Os-191m	IT	13.10h	1.64E-16	2.09E-16	1.275
Os-193	B-	30.11h	9.33E-16	9.83E-16	1.053
Os-194	B-	6.0y	1.12E-16	1.60E-16	1.428
Os-196	B-	34.9m	9.45E-16	9.89E-16	1.047
Ir-180	ECB+	1.5m	4.15E-15	4.38E-15	1.054
Ir-182	ECB+	15m	3.54E-15	3.75E-15	1.059

Radionuclide	Decay Mode	Halflife	Gy/Bq s	Sv / Bq s	RBE
Ir-183	ECB+	58m	1.26E-15	1.43E-15	1.135
Ir-184	ECB+	3.09h	2.26E-15	2.51E-15	1.109
Ir-185	ECB+	14.4h	9.40E-16	1.12E-15	1.189
Ir-186	ECB+	16.64h	1.62E-15	1.84E-15	1.135
Ir-186m	ECB+IT	1.92h	1.21E-15	1.35E-15	1.111
Ir-187	ECB+	10.5h	4.11E-16	5.29E-16	1.286
Ir-188	ECB+	41.5h	1.63E-15	1.78E-15	1.091
Ir-189	EC	13.2d	1.84E-16	2.64E-16	1.439
Ir-190	EC	11.78d	1.37E-15	1.60E-15	1.171
Ir-190m	IT	1.120h	6.08E-17	9.81E-17	1.614
Ir-190n	ECIT	3.087h	1.25E-16	1.81E-16	1.446
Ir-191m	IT	4.94s	2.97E-16	3.96E-16	1.331
Ir-192	B-EC	73.827d	1.16E-15	1.30E-15	1.126
Ir-192m	ITB-	1.45m	1.31E-16	1.72E-16	1.315
Ir-192n	IT	241y	3.87E-16	4.66E-16	1.203
Ir-193m	IT	10.53d	1.85E-16	2.28E-16	1.234
Ir-194	B-	19.28h	1.94E-15	1.97E-15	1.012
Ir-194m	B-	171d	2.21E-15	2.52E-15	1.142
Ir-195	B-	2.5h	9.36E-16	1.03E-15	1.102
Ir-195m	B-IT	3.8h	9.11E-16	1.03E-15	1.135
Ir-196	B-	52s	2.89E-15	2.92E-15	1.011
Ir-196m	B-	1.40h	2.87E-15	3.23E-15	1.123

Radionuclide	Decay Mode	Halflife	Gy/Bq s	Sv / Bq s	RBE
Pt-187	ECB+	2.35h	8.68E-16	1.04E-15	1.195
Pt-189	ECB+	10.87h	6.37E-16	7.92E-16	1.243
Pt-191	EC	2.802d	4.31E-16	5.64E-16	1.309
Pt-193	EC	50y	2.24E-17	5.07E-17	2.26
Pt-193m	IT	4.33d	3.34E-16	4.19E-16	1.254
Pt-195m	IT	4.02d	5.06E-16	6.55E-16	1.295
Pt-197	B-	19.8915h	6.14E-16	6.78E-16	1.104
Pt-197m	ITB-	95.41m	8.29E-16	9.27E-16	1.118
Pt-199	B-	30.80m	1.42E-15	1.47E-15	1.035
Pt-200	B-	12.5h	5.91E-16	6.74E-16	1.141
Pt-202	B-	44h	1.51E-15	1.53E-15	1.01
Au-186	ECB+	10.7m	3.66E-15	3.86E-15	1.053
Au-190	ECB+	42.8m	2.18E-15	2.35E-15	1.078
Au-191	ECB+	3.18h	6.91E-16	8.53E-16	1.235
Au-192	ECB+	4.94h	1.62E-15	1.77E-15	1.093
Au-193	EC	17.65h	2.81E-16	3.87E-16	1.378
Au-193m	ITEC	3.9s	3.73E-16	4.68E-16	1.253
Au-194	ECB+	38.02h	8.87E-16	1.01E-15	1.136
Au-195	EC	186.098d	2.04E-16	3.08E-16	1.512
Au-195m	IT	30.5s	4.38E-16	5.36E-16	1.224
Au-196	ECB-	6.183d	4.75E-16	5.88E-16	1.238
Au-196m	IT	9.6h	1.09E-15	1.31E-15	1.203

Radionuclide	Decay Mode	Halflife	Gy/Bq s	Sv / Bq s	RBE
Au-198	B-	2.69517d	1.08E-15	1.16E-15	1.073
Au-198m	IT	2.27d	1.07E-15	1.32E-15	1.225
Au-199	B-	3.139d	4.15E-16	4.83E-16	1.164
Au-200	B-	48.4m	1.89E-15	1.93E-15	1.017
Au-200m	B-IT	18.7h	2.15E-15	2.44E-15	1.135
Au-201	B-	26m	1.01E-15	1.05E-15	1.038
Au-202	B-	28.8s	2.61E-15	2.64E-15	1.009
Hg-190	ECB+	20.0m	3.01E-16	4.28E-16	1.421
Hg-191m	ECB+	50.8m	1.49E-15	1.73E-15	1.158
Hg-192	EC	4.85h	3.83E-16	5.21E-16	1.361
Hg-193	ECB+	3.80h	8.25E-16	9.65E-16	1.169
Hg-193m	ECB+IT	11.8h	9.10E-16	1.04E-15	1.141
Hg-194	EC	440y	2.43E-17	5.30E-17	2.179
Hg-195	ECB+	10.53h	3.24E-16	4.23E-16	1.305
Hg-195m	ITECB+	41.6h	5.21E-16	6.67E-16	1.281
Hg-197	EC	64.94h	2.36E-16	3.27E-16	1.385
Hg-197m	ITEC	23.8h	5.89E-16	6.94E-16	1.178
Hg-199m	IT	42.66m	9.62E-16	1.07E-15	1.109
Hg-203	B-	46.612d	4.19E-16	4.91E-16	1.172
Hg-205	B-	5.2m	1.25E-15	1.27E-15	1.015
Hg-206	B-	8.15m	1.07E-15	1.12E-15	1.043
Hg-207	B-	2.9m	3.86E-15	4.03E-15	1.043

Radionuclide	Decay Mode	Halflife	Gy/Bq s	Sv / Bq s	RBE
Tl-190	ECB+	2.6m	4.56E-15	4.72E-15	1.035
Tl-190m	ECB+	3.7m	3.81E-15	4.08E-15	1.072
Tl-194	ECB+	33.0m	2.12E-15	2.25E-15	1.063
Tl-194m	ECB+	32.8m	2.72E-15	3.05E-15	1.12
Tl-195	ECB+	1.16h	1.09E-15	1.25E-15	1.14
Tl-196	ECB+	1.84h	1.82E-15	1.98E-15	1.089
Tl-197	ECB+	2.84h	4.96E-16	5.95E-16	1.2
Tl-198	ECB+	5.3h	1.59E-15	1.76E-15	1.102
Tl-198m	ECB+IT	1.87h	1.45E-15	1.68E-15	1.153
Tl-199	ECB+	7.42h	3.52E-16	4.47E-16	1.268
Tl-200	ECB+	26.1h	1.12E-15	1.27E-15	1.134
Tl-201	EC	72.912h	1.92E-16	2.78E-16	1.447
Tl-202	EC	12.23d	4.39E-16	5.41E-16	1.233
Tl-204	B-EC	3.78y	5.49E-16	5.69E-16	1.038
Tl-206	B-	4.200m	1.25E-15	1.26E-15	1.014
Tl-206m	IT	3.74m	2.38E-15	2.68E-15	1.123
Tl-207	B-	4.77m	1.14E-15	1.16E-15	1.016
Tl-208	B-	3.053m	3.69E-15	3.83E-15	1.039
Tl-209	B-	2.161m	3.18E-15	3.35E-15	1.053
Tl-210	B-	1.30m	5.00E-15	5.20E-15	1.041
Pb-195m	ECB+	15m	2.06E-15	2.32E-15	1.127
Pb-196	ECB+	37m	6.32E-16	7.64E-16	1.208

Radionuclide	Decay Mode	Halflife	Gy/Bq s	Sv / Bq s	RBE
Pb-197	ECB+	8m	1.35E-15	1.50E-15	1.107
Pb-197m	ECB+IT	43m	1.51E-15	1.72E-15	1.139
Pb-198	EC	2.4h	5.43E-16	6.69E-16	1.232
Pb-199	ECB+	90m	9.34E-16	1.05E-15	1.128
Pb-200	EC	21.5h	4.12E-16	5.28E-16	1.282
Pb-201	ECB+	9.33h	7.45E-16	8.78E-16	1.178
Pb-201m	IT	61s	9.06E-16	9.69E-16	1.071
Pb-202m	ITEC	3.53h	1.88E-15	2.08E-15	1.103
Pb-203	EC	51.873h	3.84E-16	4.88E-16	1.27
Pb-204m	IT	67.2m	1.86E-15	2.03E-15	1.091
Pb-205	EC	1.53E+7y	2.02E-17	4.02E-17	1.996
Pb-209	B-	3.253h	4.56E-16	4.75E-16	1.043
Pb-211	B-	36.1m	1.10E-15	1.13E-15	1.024
Pb-212	B-	10.64h	5.27E-16	6.02E-16	1.141
Pb-214	B-	26.8m	8.86E-16	9.70E-16	1.094
Bi-197	ECB+	9.3m	1.99E-15	2.16E-15	1.086
Bi-200	ECB+	36.4m	2.51E-15	2.80E-15	1.119
Bi-201	ECB+	108m	1.45E-15	1.60E-15	1.099
Bi-202	ECB+	1.72h	2.51E-15	2.78E-15	1.108
Bi-203	ECB+	11.76h	1.97E-15	2.15E-15	1.089
Bi-204	ECB+	11.22h	2.45E-15	2.71E-15	1.108
Bi-205	ECB+	15.31d	1.35E-15	1.48E-15	1.101

Radionuclide	Decay Mode	Halflife	Gy/Bq s	Sv / Bq s	RBE
Bi-206	ECB+	6.243d	2.87E-15	3.18E-15	1.108
Bi-207	ECB+	32.9y	1.48E-15	1.64E-15	1.105
Bi-208	EC	3.68E+5y	1.74E-15	1.83E-15	1.048
Bi-212n	B-	7.0m	1.23E-15	1.25E-15	1.014
Bi-215	B-	7.6m	1.75E-15	1.80E-15	1.034
Bi-216	B-	2.17m	3.66E-15	3.76E-15	1.026
Rn-223	B-	24.3m	1.73E-15	1.85E-15	1.069
Fr-222	B-	14.2m	1.80E-15	1.89E-15	1.049
Fr-224	B-	3.33m	2.44E-15	2.53E-15	1.034
Fr-227	B-	2.47m	2.21E-15	2.32E-15	1.053
Ra-225	B-	14.9d	2.63E-16	3.04E-16	1.158
Ra-227	B-	42.2m	1.18E-15	1.28E-15	1.089
Ra-228	B-	5.75y	3.72E-17	6.70E-17	1.802
Ra-230	B-	93m	5.76E-16	6.34E-16	1.101
Ac-228	B-	6.15h	1.72E-15	1.84E-15	1.072
Ac-230	B-	122s	2.53E-15	2.59E-15	1.023
Ac-231	B-	7.5m	1.81E-15	1.94E-15	1.074
Ac-232	B-	119s	3.08E-15	3.16E-15	1.027
Ac-233	B-	145s	2.33E-15	2.41E-15	1.036
Th-231	B-	25.52h	4.17E-16	5.32E-16	1.277
Th-233	B-	22.3m	9.89E-16	1.04E-15	1.055
Th-234	B-	24.10d	1.55E-16	1.88E-16	1.214

Radionuclide	Decay Mode	Halflife	Gy/Bq s	Sv / Bq s	RBE
Th-235	B-	7.1m	1.59E-15	1.61E-15	1.013
Th-236	B-	37.5m	8.76E-16	9.11E-16	1.04
Pa-232	B-EC	1.31d	1.15E-15	1.30E-15	1.128
Pa-233	B-	26.967d	6.87E-16	8.13E-16	1.182
Pa-234	B-	6.70h	2.10E-15	2.36E-15	1.122
Pa-234m	B-IT	1.17m	1.90E-15	1.91E-15	1.007
Pa-235	B-	24.5m	1.13E-15	1.17E-15	1.039
Pa-236	B-	9.1m	2.55E-15	2.66E-15	1.041
Pa-237	B-	8.7m	1.82E-15	1.90E-15	1.046
U-237	B-	6.75d	5.96E-16	7.45E-16	1.251
U-239	B-	23.45m	9.96E-16	1.05E-15	1.052
U-240	B-	14.1h	3.10E-16	3.68E-16	1.188
U-242	B-	16.8m	9.25E-16	9.56E-16	1.033
Np-232	ECB+	14.7m	1.21E-15	1.41E-15	1.164
Np-234	ECB+	4.4d	9.68E-16	1.08E-15	1.116
Np-236m	ECB-	22.5h	2.50E-16	2.94E-16	1.175
Np-238	B-	2.117d	1.05E-15	1.14E-15	1.086
Np-239	B-	2.3565d	7.68E-16	9.23E-16	1.201
Np-240	B-	61.9m	2.03E-15	2.25E-15	1.111
Np-240m	B-IT	7.22m	1.83E-15	1.90E-15	1.041
Np-241	B-	13.9m	1.04E-15	1.09E-15	1.048
Np-242	B-	2.2m	2.28E-15	2.31E-15	1.013

Radionuclide	Decay Mode	Halflife	Gy/Bq s	Sv / Bq s	RBE
Np-242m	B-	5.5m	2.49E-15	2.69E-15	1.082
Pu-243	B-	4.956h	4.24E-16	4.67E-16	1.102
Pu-245	B-	10.5h	1.06E-15	1.15E-15	1.083
Pu-246	B-	10.84d	3.98E-16	5.10E-16	1.282
Am-242	B-EC	16.02h	4.39E-16	4.90E-16	1.115
Am-244	B-	10.1h	1.43E-15	1.64E-15	1.142
Am-244m	B-	26m	1.21E-15	1.25E-15	1.028
Am-245	B-	2.05h	6.91E-16	7.32E-16	1.058
Am-246	B-	39m	2.31E-15	2.58E-15	1.118
Am-246m	B-	25.0m	1.93E-15	2.04E-15	1.057
Am-247	B-	23.0m	1.43E-15	1.51E-15	1.061
Cm-239	ECB+	2.9h	2.87E-16	4.02E-16	1.4
Cm-249	B-	64.15m	6.72E-16	7.24E-16	1.078
Cm-251	B-	16.8m	1.14E-15	1.18E-15	1.035
Bk-246	EC	1.80d	8.22E-16	9.79E-16	1.191
Bk-248m	B-EC	23.7h	4.92E-16	5.41E-16	1.099
Bk-250	B-	3.212h	1.38E-15	1.48E-15	1.07
Bk-251	B-	55.6m	9.38E-16	1.05E-15	1.122
Cf-255	B-	85m	5.02E-16	5.22E-16	1.039
Es-250	EC	8.6h	1.79E-15	2.24E-15	1.25
Es-250m	ECB+	2.22h	5.23E-16	6.28E-16	1.2
Es-256	B-	25.4m	1.35E-15	1.38E-15	1.024

APPENDIX B:

TABULATED RBE VALUES

RBE values of electrons and photons predicted by the DSB yield method.

Electron		Photon	
Energy (keV)	RBE	Energy (keV)	RBE
3.10E-02	0.00	3.70E-02	0.00
8.90E-02	0.41	4.60E-02	0.11
1.77E-01	2.07	7.10E-02	0.29
3.16E-01	4.28	1.00E-01	0.63
5.62E-01	5.51	1.38E-01	1.35
1.00E+00	4.73	2.15E-01	2.69
1.78E+00	3.39	3.72E-01	4.57
3.16E+00	2.48	4.64E-01	5.03
5.62E+00	1.91	5.17E-01	5.30

1.00E+01	1.54	1.00E+00	4.72
3.16E+01	1.22	5.18E+00	2.00
5.62E+01	1.15	1.39E+01	1.46
1.00E+02	1.09	1.00E+02	1.42
1.78E+02	1.06	7.20E+02	1.11
3.16E+02	1.02	1.00E+03	1.08
5.62E+02	1.02	5.18E+03	1.02
1.00E+03	1.00	1.00E+04	1.01

APPENDIX C

INTER-IONIZATION DISTANCE PROFILER CODE

```
####
####
####
#### Author: Michael Bellamy
#### Project: Electron RBE
#### Summary: Investigates the frequency that ionizations pairs occur
in specific distance intervals
####       this simulation interrogates electrons of multiple energies
and produces several histograms
####
####
####
####
####
#include <conio.h>                                                    //for
kbhit
#include <iostream>                                                   //for
cout and cin
```

```
#include <iomanip>                                                    //for
setw output formatting
#include <fstream>                                                    //for
file IO
#include "track.h"
      //NOREC
#include <math.h>                                                  //for
square root and square
#include <ctime>                                                   //for
performance timing

using namespace std;

//declare distance function
double PointDist(Point a, Point b)
{
//custom distance function which returns the square of the distance
between two points
double dist;
dist = (a.x-b.x)*(a.x-b.x) + (a.y-b.y)*(a.y-b.y) + (a.z-b.z)*(a.z-b.z);
return dist;
}

struct Point
//define a custom 3D-point datatype for storing events in the electron
track
{
bool marked;
//marked - stores whether this ionization was already considered
```

```
int ps;
//ps store event type
int type;
//x,y,z store cartesian coordinates of the point
double x;
double y;
double z;
//x,y,z store cartesian coordinates of the point
double Energy;
//energy - store event energy
double NeighbourhoodEnergy;
//NeighbourhoodEnergy stores energy of events in the neighbourhood of
this event
int NumberNeighbours;
//stores number of neighbours

};



struct Histogram
//define a Histogram datatype
{
float min;
float max;
int N;
vector<float> Data;
};

double PointDist(Point a, Point b);
```

```
int main(int argc, char* argv[])
{
//initialize file IO
ofstream myfile;
myfile.open ("data.txt",ios::app);

//initialize timer functions
time_t start, end;
time(&start);

//initialize point vector
int E=20;
Point current;
vector<Point> PointData;
PointData.reserve(200000);

///initialize other variables
double dist;
int ITER;
int num_ionizations=0;
int num_pairs=0;
float area_under_histogram=0;
int bin;

Track t;
int size=0;

//initialize histogram variables
```

```
Histogram histogram;
histogram.N   = 100 ;
histogram.min = 0   ;
histogram.max = 0.1 ;


//get command line parameters
if(argc > 1)
{
cout  <<  "Iterations"<<  setw(9)  <<"  energy"<<  setw(9)  <<"hist  max"<<
setw(15) <<"Num of bins" << endl;
ITER = atoi(argv[1]);
E = atoi(argv[2]);
histogram.max = atof(argv[3]);
histogram.N = atoi(argv[4]);
cout << setw(9) << ITER << setw(9) << E << setw(9) << histogram.max <<
setw(15) << histogram.N << endl;
}

//resize hisgram parameters
histogram.Data.resize(histogram.N);
//Initilize Histogram to zero
for (int i=0; i<histogram.N; i++)
{
histogram.Data[i]=0;
}

for(int iter=0;iter<ITER;iter++)
{
```

```
//Populate pointData vector
t.generateTrack(E,0,0,0,1,0,0);
PointData.clear();
num_ionizations=0;
while(!t.isOver() )
{
t.getLine(
&current.ps,&current.type,&current.x,&current.y,&current.z,&current.Ene
rgy);
if(current.type > 6 && current.type < 12)
{
current.NeighbourhoodEnergy=0;
current.NumberNeighbours=0;
PointData.push_back(current);
num_ionizations++;
}
}

//compute distances and store in histogram
if (PointData.size()>0)
{
for(unsigned int i=0;i<PointData.size()-1;i++)
{
for(unsigned int j=i+1;j<PointData.size();j++)
{
//AP sum formula for the total number of pairs
num_pairs=(PointData.size()-1)/2.0        *        (2*(PointData.size()-
1)+(PointData.size()-2)*(-1));
```

```
if(   abs(PointData[i].x   -   PointData[j].x)   <   histogram.max   &&
abs(PointData[i].y    -    PointData[j].y)    <    histogram.max    &&
      abs(PointData[i].z - PointData[j].z) < histogram.max )
{
dist = sqrt(PointDist(PointData[i],PointData[j]));
if(dist < histogram.max && dist > histogram.min)
{
bin    =    floor((dist    -    histogram.min)/    (    (histogram.max-
histogram.min)/histogram.N));
histogram.Data[bin]+=       1.0/num_pairs       /       ((histogram.max-
histogram.min)/histogram.N)*(num_ionizations-1);
}
}
}
}
}

cout << setw(20) << "Number of pairs= " << (PointData.size()-1)/2.0 *
(2*(PointData.size()-1)+(PointData.size()-2)*(-1)) << endl;
cout << "number of ionizations:" << setw(5) << PointData.size() <<
endl;
cout <<endl << setw(20) << "Distance(nm)" << setw(20) << "frequency per
Ionization" << endl;

//determine area under curve to test for normalization
for(int i=0;i<histogram.N;i++)
{
```

```
area_under_histogram   +=   (histogram.max-histogram.min)/histogram.N   *
histogram.Data[i];
}
cout << " area under hist = " << area_under_histogram/ITER  << endl;
cout << "bin width = " <<  (histogram.max-histogram.min)/histogram.N <<
endl;

myfile <<  "Energy " << E << " eV" << endl;
for(int i=0;i<histogram.N;i++)
{
cout    << setw(20) << (histogram.max-histogram.min)/histogram.N * i <<
setw(20) << histogram.Data[i]/ITER << endl;
//myfile  <<  (histogram.max-histogram.min)/histogram.N  *  i  <<  setw(20)
<< histogram.Data[i]/ITER << endl;
myfile << histogram.Data[i]/ITER << endl;
}
myfile << "end" << endl;

time(&end);
cout << float(difftime(end, start))<<" seconds."<<endl;
myfile.close();

exit(0);                              //end
}
```

APPENDIX D

DNA MODEL CODE

```
####
####
####
#### Author: Michael Bellamy
#### Project: Electron RBE
#### Chromatin.py
#### Constructs a Solenoidal chromatin model of DNA from geometric
#### parameters.
####
####
####
####
```

```
import matplotlib as mpl
from mpl_toolkits.mplot3d import Axes3D
import numpy as np
import matplotlib.pyplot as plt
```

```
NUM_BASE_PAIRS=8200


CHROMATIN_RADIUS=10
CHROMATIN_HEIGHT_PER_REVOLUTION=12
CHROMATIN_REVOLUTIONS=16
NUCLEOSOME_RADIUS=5
NUCLEOSOME_HEIGHT_PER_REVOLUTION=14
HELIX_RADIUS=2
HELIX_HEIGHT_PER_REVOLUTION=3.4




HELIX_HEIGHT_PER_RADIAN=HELIX_HEIGHT_PER_REVOLUTION/3.1415/2
NUCLEOSOME_HEIGHT_PER_RADIAN=NUCLEOSOME_HEIGHT_PER_REVOL
UTION/3.1415/2
CHROMATIN_HEIGHT_PER_RADIAN=CHROMATIN_HEIGHT_PER_REVOLUTI
ON/3.1415/2



f = open('DNA_Coords.txt', 'w')
mpl.rcParams['legend.fontsize'] = 10
fig = plt.figure()
```

```
ax = fig.gca(projection='3d')



Z=np.zeros((NUM_BASE_PAIRS))

Y=np.zeros((NUM_BASE_PAIRS))

X=np.zeros((NUM_BASE_PAIRS))


##include chromatin vectorization foundation

for i in range(NUM_BASE_PAIRS):

   theta = (float(i)/NUM_BASE_PAIRS)*2*np.pi*CHROMATIN_REVOLUTIONS

   X[i]=X[i]+ CHROMATIN_RADIUS*np.cos(theta)

   Y[i]=Y[i]+ CHROMATIN_RADIUS*np.sin(theta)

   Z[i]=Z[i]+ CHROMATIN_HEIGHT_PER_RADIAN*theta


##superimpose nucleosome  vectorization

distance=0

for i in range(NUM_BASE_PAIRS-1):

   distance = distance + ( (Z[i]-Z[i+1])**2 + (Y[i]-Y[i+1])**2 + (X[i]-X[i+1])**2 )**0.5

   theta = distance/float(NUCLEOSOME_HEIGHT_PER_RADIAN)


   z_angle = 3.1415    - np.arccos( (Z[i+1]-Z[i])/( (Z[i]-Z[i+1])**2 +(Y[i]-Y[i+1])**2 +

(X[i]-X[i+1])**2 )**0.5 )

   x_angle =  np.arccos( (X[i+1]-X[i])/( ((Y[i]-Y[i+1])**2 + (X[i]-X[i+1])**2 )**0.5 ))
```

```
    if (Y[i+1]-Y[i])<0: x_angle=x_angle*-1

    z=0
    y=NUCLEOSOME_RADIUS*np.sin(theta)
    x=NUCLEOSOME_RADIUS*np.cos(theta)

    #compute first rotation (around y axis)
    x1= x*np.cos(z_angle)+z*np.sin(z_angle)
    y1= y
    z1=-x*np.sin(z_angle)+z*np.cos(z_angle)

    #compute second rotation (around z axis)
    x2=x1*np.cos(x_angle)-y1*np.sin(x_angle)
    y2=x1*np.sin(x_angle)+y1*np.cos(x_angle)
    z2=z1

    #superimpose vector
    X[i]=X[i]+x2
    Y[i]=Y[i]+y2
    Z[i]=Z[i]+z2

##superimpose HELIX  vectorization
distance=0
```

```
for i in range(NUM_BASE_PAIRS-1):
    distance = distance + ( (Z[i]-Z[i+1])**2 + (Y[i]-Y[i+1])**2 + (X[i]-X[i+1])**2 )**0.5
    theta = distance/float(HELIX_HEIGHT_PER_RADIAN)

    z_angle = np.arccos( (Z[i+1]-Z[i])/( (Z[i]-Z[i+1])**2 +(Y[i]-Y[i+1])**2 + (X[i]-X[i+1])**2 )**0.5 )
    x_angle =  np.arccos( (X[i+1]-X[i])/( ((Y[i]-Y[i+1])**2 + (X[i]-X[i+1])**2 )**0.5 ))
    if (Y[i+1]-Y[i])<0: x_angle=x_angle*-1

    z=0
    y=HELIX_RADIUS*np.sin(theta)
    x=HELIX_RADIUS*np.cos(theta)

    #compute first rotation (around y axis)
    x1= x*np.cos(z_angle)+z*np.sin(z_angle)
    y1= y
    z1=-x*np.sin(z_angle)+z*np.cos(z_angle)

    #compute second rotation (around z axis)
    x2=x1*np.cos(x_angle)-y1*np.sin(x_angle)
    y2=x1*np.sin(x_angle)+y1*np.cos(x_angle)
    z2=z1
```

```
    #superimpose vector
    X[i]=X[i]+x2
    Y[i]=Y[i]+y2
    Z[i]=Z[i]+z2
print "distance ", distance
print "inter-bp distance", distance/NUM_BASE_PAIRS
print "length of array X", len(X)

for i in range(len(X)):
    print >>f, X[i], Y[i], Z[i], i

ax.plot(X[0:-1],  Y[0:-1],  Z[0:-1],  label='DNA 30nm diameter chromatin fiber')

ax.legend()
plt.show()
```

APPENDIX E

PHOTON INITIAL ELECTRON SPECTRUM CODE

```
####
####
####
#### Author: Michael Bellamy
#### Project: Electron RBE
#### InitialElectronEnergy.py
#### determines the energy dependent electron yield from photons which
#### completely deposit their energy in liquid water.
#### This particular example produces the electron spectrum of a 100eV
#### photon
####
####
####
####
####


import csv,pylab
import matplotlib.pyplot as pplot
```

```
import numpy as np
import random
import math

from scipy import interpolate
from math import pi , cos
from pylab import hist

class KN:
    def __init__(self):
        self.infile = csv.reader(open("KNdata.csv","rb"))
        self.cdf=[]
        for self.line in self.infile:
            self.cdf.append([])
            for self.item in self.line:
                self.cdf[-1].append(float(self.item))
        self.cdf_fit = []
        self.inv_cdf_fit = []
        self.angles = range(0,361,36)
        for self.line in self.cdf:

self.cdf_fit.append(interpolate.interp1d(np.array(self.angles),np.array
(self.line)))

self.inv_cdf_fit.append(interpolate.interp1d(np.array(self.line),np.arr
ay(self.angles)))
        self.x = []
        for i in range(10000):
```

```
self.x.append(float(self.inv_cdf_fit[1](random.uniform(0,1))))
    def angle(self,energy):
        if energy < 0.05:
            self.bin = 0
        elif  energy > 1:
            self.bin = 20
        else:
            self.bin = int(round(float( energy * 20.)))
        return float(self.inv_cdf_fit[self.bin](random.uniform(0,1)))


class CrossSection:
    def __init__(self, filename):
        self.data = csv.reader(open(filename,"rb"))
        self.energy=[]
        self.compton=[]
        self.photoElectric=[]
        for line in self.data:
            self.energy.append(float(line[0]))
            self.compton.append(float(line[1]))
            self.photoElectric.append(float(line[2]))
        self.comptonFit                                                =
interpolate.interp1d(np.array(self.energy),np.array(self.compton))
        self.photoElectricFit                                          =
interpolate.interp1d(np.array(self.energy),np.array(self.photoElectric)
)
    def values(self, erg):
        return                                 float(self.comptonFit(erg)),
float(self.photoElectricFit(erg))
```

```
    def probability(self,erg):
        a = float(self.comptonFit(erg))
        b = float(self.photoElectricFit(erg))
        return a/(a+b) , b/(a+b)
    def get_type(self,erg):
        if self.probability(erg)[1] < random.uniform(0,1):
            return "c"
        else:
            return "p"


class Photon:
    #Instantiate a photon in water with specified energy
    def __init__(self):
        self.energy = 0
    def set_energy(self,erg):
        self.energy = erg
    def collide(self,xs,kn):
        #determine type of collision
        if xs.get_type(self.energy) == "p":
            # photoelectric - dump all energy
            deposited = self.energy
            self.energy = self.energy - deposited
            return deposited
        else:
            # Compton scatter:
            # sample angle
            theta = kn.angle(self.energy)
            # compute deposited energy
```

```
            deposited = self.energy - self.energy / ( 1 + ( (1 -
cos(theta))*self.energy/0.511))
            # compute new energy
            self.energy = self.energy - deposited
            #return energy of compton electron
            return deposited




class Histogram:
    #Create a histogram object with specified Min, Max, Bins
    def __init__(self,minimum,maximum,bins):
        self.min = minimum
        self.max = maximum
        self.bins = bins
        self.hist = [0] * (bins)
        self.binWidth = (self.max - self.min) / ( bins - 1 )
    def add(self,entry):
        self.binNum = int( math.floor( (entry - self.min) /
self.binWidth ) )
        if self.binNum < 0:
            self.binNum = 0
            print "lower bound truncation"
        if self.binNum >= self.bins:
            self.binNum = self.bins - 1
            print "upper bound truncation"
        print self.binNum
        self.hist[self.binNum] += 1
        print self.hist
```

```
xs = CrossSection("xsdata.csv")
kn = KN()



p = Photon()
deposit_array = []
for i in range(500):
    p.set_energy(.0001)
    while p.energy > 0 :
        deposit_array.append(p.collide(xs,kn))
a = pplot.hist(deposit_array,100, log=True)


outfile = open("100ev.csv","w")
for i in range(len(a[0])):
      print a[1][i],a[0][i]
      outfile.write(str(a[1][i]) + ", " + str(a[0][i]) + "\n")
outfile.close()
```

REFERENCES

Ay MR, S Sarker, M Shahriari, H Zaidi (2005). Assessment of different computational models for generation of x-ray spectra in diagnostic radiology and mammography, *Med Phys* **32(**6): 1660-1675, DOI: 10.1118/1.1906126.

Beyreuther E, W Dorr, A Lehnert (2009). Relative biological effectiveness of 25 and 10 kV x-rays for the induction of chromosomal aberrations in two human mammary epithelial cell lines, *Radiat Environ Biophys* **48:**333–340.

Boudaïffa B, P Cloutier, D Hunting, M Huels, L Sanche (2000). Resonant formation of DNA strand breaks by low-energy (3 to 20 eV) electrons, *Science* **287**(5458):1658-1660.

Burch P (1957a). Calculation of energy dissipation characteristics in water for various radiations,aspects of relative biological efficiency, *Radiat Res* **6**(3): 289-301.

Burch P (1957b). Some aspects of relative biological efficiency, *Br J Radiol* **30:**524-529.

Charlton DE, JL Humm (1988). A method of calculating initial DNA strand breakage following the decay of incorporated ^{125}I, *Int J Radiat Biol* **53:**353-365.

Charlton D, H Nikjoo, JL Humm (1989). Calculation of initial yields of single and double strand breaks in cell nuclei from electrons, protons and alpha particles, *Int J Radiat Biol* **56:**1-19.

Cho S, O Vassilev, J Horton (2007). Comparison between an event-by-event Monte Carlo code NOREC, and ETRAN for electron scaled point kernels between 20 keV and 1 MeV, *Radiat Environ Biophys* **47:**77-83.

Dingfelder M, RH Ritchie, JE Turner, W Friedland, HG Paretzke and RN Hamm (2008). Comparisons of calculations with PARTRAC and NOREC: transport of electrons in liquid water *Radiat. Res.* **169:**584–94

Dietze G and WG Alberts (2004). Why it is advisable to keep wR = 1 and Q = 1 for photons and electrons, *Radiat Prot Dosim* **109**:297-302.

Eckerman KF, RW Leggett, M Cristy, CB Nelson, JC Ryman, AL Sjoreen, RC Ward (2006). *User's Guide to the DCAL System*, ORNL/TM-2001/190, Oak Ridge National Laboratory, Oak Ridge, TN.

EPA (1999). *Cancer Risk Coefficients for Environmental Exposure to Radionuclides, Federal Guidance Report No. 13*, EPA 402-R-99-001 (Oak Ridge National Laboratory, Oak Ridge, TN; U.S. Environmental Protection Agency, Washington, DC).

EPA (2011). *EPA Radiogenic Cancer Risk Models and Projections for the U.S. Population*, EPA 402-R-11-001, U.S. U.S. Environmental Protection Agency, Washington, DC.

Egbert S, G Kerr, H Cullings (2007). DS02 fluence spectra for neutrons and gamma rays at Hiroshima and Nagasaki with fluence-to-kerma coefficients and transmission factors for sample measurements, *Radiat Environ Biophys* **46:** 311–325.

Failla G., Henshaw S., (1931). The Relative Biological Effectiveness of X-rays and Gamma Rays, *Radiology*, **17**:1 1-43; doi:10.1148/17.1.1

Folkard M, KM Prise, B Vojnovic, S Davies, MJ Roper and B D Michael (1993). Measurement of DNA damage by electrons with energies between 25 and 4000 eV, *Int J Radiat Biol* **64**(6): 651-658.

Friedland W, H Paretzke, F Ballarini, A Ottolenghi, G Kreth, C Cremer (2008). First steps towards systems radiation biology studies concerned with DNA and chromosome structure within living cells, *Radiat Environ Biophys* **47:** 49-61.

Goodhead D, J Thacker, R Cox (1981). Is selective absorption of ultrasoft x-rays biologically important in mammalian cells?, *Phys Med Biol* **26,** 1115.

Goodhead D. (2006). Energy Deposition Stochastic and Track Structure: What About The Target?, Radiat Prot Dosim **122(**1/4): 3-15.

Hill MA (2004). The variation in biological effectiveness of x-rays and gamma rays with energy, *Radiat Prot Dosim* **112**(4): 471–48.

Health Protection Agency (UK) (2007). *Review of Risks from Tritium. Report of the Independent Advisory Group on Ionising Radiation.* Documents of the Health Protection Agency. Radiation, Chemical and Environmental Hazards. www.hpa.org.uk/webc/HPAwebFile/HPAweb_C/1197382221858

Hunter N, C Muirhead (2009). Review of relative biological effectiveness dependence on linear energy transfer for low-LET radiations, *J. Radiol Prot* **29:**5–21.

ICRP (International Commission on R adiological Protection). (1991). 1990 Recommendations of the International Commission on Radiological Protection. ICRP Publication 60. Ann ICRP 21(1-3).

ICRP (International Commission on Radiological Protection). (1991). The Biological Basis for Dose Limitation in t he Skin. ICRP Publication 59. Ann ICRP 22(2).

ICRP (International Commission on R adiological Protection). (1993). Age-dependent Doses to Members of the Public from Intake of Radionuclides: Part 2. Ingestion Dose Coefficients. ICRP Publication 67. Ann ICRP 23(3/4).

ICRP (International Commission on R adiological Protection). (2000). Pregnancy and Medical Radiation. ICRP Publication 84. Ann ICRP 30(1).

ICRP (International Commission on Radi ological Protection). (2003). Relative Biological Effectiveness (RBE), Quality Factor (Q), and Radiation Weighting Factor (wR).
ICRP Publication 92. Ann ICRP 33(4).

ICRP (International Commission on Radi ological Protection) (2008). Nuclear Decay Data for Dosimetric Calculations. ICRP Publication 107. *Ann ICRP* 38 (3).

Kocher DC, AI Apostoaci, FO Hoffman (2005). Radiation effectiveness factors for use in calculating probability of causation of radiogenic cancer, Health Phys 89(1): 3-32.

Land C, E Gilbert, J Smith, FO Hoffman, I Apostoaei, B Thomas, DC Kocher (2003). Report of the NCI-CDC working group to revise the 1985 NIH radioepidemiological tables. National Cancer Institute, Bethesda MD.

Lehnert A, Lessman E, Pawelke J., Dorr W. (2006) RBE of 25 kV X-rays for the survival and induction of micronuclei in the human mammary epithelial cell line MCF-12A, *Radiat. Environ. Biophys.* **45:**256-260, DOI 10.1007/s00411-006-0062-3

Little MP, BE Lambert (2008). Systematic review of experimental studies on the relative biological effectiveness of tritium, *Radiat Environ Biophys* **47:**71–93.

Mestres M., Caballin M., Barrios L., Ribas M (2008) RBE of X Rays of Different energies, *Radiation Research,* **170,** 93-100

Michael BD, P O'Neill (2000). A Sting in the Tail of Electron Tracks, *Science* **287** (5458): 1603-1604, DOI: 10.1126/science.287.5458.1603.

Milligan J, JA Aguilera, JF Ward (1993). Variation of single-strand break yield with scavenger concentration for plasmid DNA irradiated in aqueous solution, *Radiat Res* **133**(2)**:**151-157.

Moissenko V, R Hamm, W Prestwich (2001). Calculation of radiation-induced DNA damage from photons and tritium beta-particles, *Radiat Environ Biophys* **40**:23–31.

National Research Council (1990). *Health Effects of Exposure to Low Levels of Ionizing Radiation: BEIR V*. Washington, DC: The National Academies Press.

National Research Council (2006). *Health Risks from Exposure to Low Levels of Ionizing Radiation: BEIR VII Phase 2*. Washington, DC: The National Academies Press.

NIOAH (2002). NIOSH-Interactive RadioEpidemiological Prorgram (IREP) technical documentation; Final report. National Institute for Occupational Safety and Health. Available at: www.cdc.gov/niosh/ocas/pdfs/irep/irepfnl.pdg.

Nikjoo H, D Goodhead (1991). Track structure analysis illustrating the prominent role of low-energy electrons in radiobiological effects of low-let radiations, *Phys Med Biol* **36:** 229-238.

Nikjoo H, P O'Neil, WE Wilson, DT Goodhead (2001). Computational Approach for Determining the Spectrum of DNA Damage Induced by Ionizing Radiation, *Radiat Res* **156**(5)**:** 577-583.

Nikjoo H, P O'Neill, DT Goodhead, M Terrissoll (1997). Computational modeling of low-energy electron-induced DNA damage by early physical and chemical events, *Int J Radiat Biol* **71:**467-483.

Nikjoo H, CE Bolton, R Watanabe, M Terrisol, P O'Neill, DT Goodhead (2002). Modelling of DNA damage induced by energetic electrons (100 eV to 100 keV), *Radiat Prot Dosim* **99**(1/4): 77-80.

Nikjoo H, L Lindborg (2010). Topical review: RBE of low energy electrons and photons, *Phys. Med. Biol.* **55,** R65–R10.

Paretzke HG (1988). Simulation von Elektronenspuren im Energiebereich 0.01-10 keV in Wasserdampf, Gesellschaft fur Strhlen-und Umweltforschung Munchen.

Pelowitz, DB (2008). *MCNPX User's Manual*, Version 2.6.0. LA-CP-07-1473. Los Alamos National Laboratory, Los Alamos, NM.

Poludniowski G, G Landry, F DeBlois, PM Evans, F Verhaegen (2009). SpekCalc: a program to calculate photon spectra from tungsten anode x-ray tubes, *Phys Med Biol* **54**:N433-N438.

Roots R, S Okada (1975). Estimation of life times and diffusion distances of radicals involved in x-ray-induced DNA strand breaks or killing of mammalian cells, *Radiat Res* **64**(2)**:** 306-320.

Sasaki MS, K Kobayashi, K Hieda, T Yamada, Y Ejima, H Maezawatt, Y Furusawa, T Ito, S Okada (1989). Induction of chromosome aberrations in human lymphocytes by monochromatic x-rays of quantum energy between 4.8 and 14.6 keV, Int J Radiat Biol 56(6):975-988.

Semenenko V, JE Turner and T Borak (2003). NOREC, a Monte Carlo code for simulating electron tracks in liquid water, *Radiat Environ Biophys*, **42,** 213-217.

Schmid E, D Regulla, H Kramer, D Harder (2002). The effect of 29 kV X rays on the dose response of chromosome aberrations in human lymphocytes, *Radiat Res* **158**(6): 771-777.

Schwarz G, M Berg, C Botstein (1966). Changes in the relative biological effectiveness (RBE) of a 35 MeV electron beam as a function of tissue depth. *Am J Roentgenol Radium Ther Nucl Med* **97:**1049-52.

Staynov D. (2008). The controversial 30nm chromatin fibre. *BioEssays,* **30:**1003-1009

Straume T (1995). High-energy gamma rays in Hiroshima and Nagasaki: Implications for risk and wR, *Health Phys* **69**(6): 954-956.

Terrissol M, A Beaudre (1990). Simulation of space and time evolution of radiolytic species induced by electrons in water, *Rad Prot Dosim* **31**(1/4):175-117.

Turner JE, RN Hamm, ML Souleyrette, DE Martz, TA Rhea, DW Schmidt (1988). Calculations for beta dosimetry using Monte Carlo code (OREC) for electron transport in water. *Health Phys* **55**(5): 741–750.

Woodcock C, S Grigoryev, R Horowitz, N Witaker (1993). A chromatin folding model that incorporates linker variability generates fibers resembling the native structures, *Proc Natl Acad Sci USA,* **90:**9021-9025.

Wright H. Magee J., Hamm R., Chatterjee A., Turner J. (1983). Calculations of physical and chemical reactions produced in irradiated water containing DNA, *ORNL Report*, CONF-850506—8.

Zirkle R., Cornelius T. (1953) Effects of ploidy and linear energy transfer on radio-biological survival curves, *Arch Biochem Biophys*, **47,** 2, 282-306.

VITA

Michael B. Bellamy

Michael Bellamy was born in Trinidad and Tobago where he attended St. Joseph Boy's Roman Catholic school and Hillview College. In 2000 he came to the United States of America, enrolled in Morehouse College and successfully completed a double Bachelors of Science degree in Mathematics and Physics. While enrolled in Morehouse college Michael took the opportunity to conduct research in semiconductor physics at IBM, astrophysics at the University of Pittsburgh and atomic spectroscopy at the Lawrence Livermore National Lab. Michael received his Masters of Science degree from Clark Atlanta University and took the opportunity to conduct theoretical research on quantum nano-structures and difference equation systems. In 2007 Michael enrolled in the Georgia Institute of Technology under the joint mentorship of Dr. Nolan Hertel and Dr. Keith Eckerman in the Nuclear Engineering department where this current research is being conducted. When he is not working on his research, Michael pursues his interest in programming, music and photography.